

University of Windsor

Scholarship at UWindor

Electronic Theses and Dissertations

Theses, Dissertations, and Major Papers

2011

Gas-liquid phenomena with dynamic contact angle in cathode of proton exchange membrane fuel cells

Xichen Wang
University of Windsor

Follow this and additional works at: <https://scholar.uwindsor.ca/etd>

Recommended Citation

Wang, Xichen, "Gas-liquid phenomena with dynamic contact angle in cathode of proton exchange membrane fuel cells" (2011). *Electronic Theses and Dissertations*. 5395.
<https://scholar.uwindsor.ca/etd/5395>

This online database contains the full-text of PhD dissertations and Masters' theses of University of Windsor students from 1954 forward. These documents are made available for personal study and research purposes only, in accordance with the Canadian Copyright Act and the Creative Commons license—CC BY-NC-ND (Attribution, Non-Commercial, No Derivative Works). Under this license, works must always be attributed to the copyright holder (original author), cannot be used for any commercial purposes, and may not be altered. Any other use would require the permission of the copyright holder. Students may inquire about withdrawing their dissertation and/or thesis from this database. For additional inquiries, please contact the repository administrator via email (scholarship@uwindsor.ca) or by telephone at 519-253-3000ext. 3208.

**GAS-LIQUID PHENOMENA WITH DYNAMIC CONTACT ANGLE IN
CATHODE OF PROTON EXCHANGE MEMBRANE FUEL CELLS**

by

XICHEN WANG

A Thesis

Submitted to the Faculty of Graduate Studies
through Mechanical, Automotive and Materials Engineering
in Partial Fulfillment of the Requirements for
the Degree of Master of Applied Science at the
University of Windsor

Windsor, Ontario, Canada

2011

©2011 Xichen Wang

Gas-liquid phenomena with dynamic contact angle in cathode of proton exchange
membrane fuel cells

by

Xichen Wang

APPROVED BY:

Dr. Tirupati Bolisetti

Department of Civil & Environmental Engineering

Dr. Ronald M Barron

Department of Mechanical, Automotive & Materials Engineering

Dr. Biao Zhou, Advisor

Department of Mechanical, Automotive & Materials Engineering

Dr. Amir Fartaj, Chair of Defense

Department of Mechanical, Automotive & Materials Engineering

September 13, 2011

DECLARATION OF PREVIOUS PUBLICATION

This thesis includes [1] original papers that have been previously published for publication in peer reviewed journals, as follows:

| Thesis Chapter | Publication title/full citation | Publication status* |
|--------------------------------|--|---------------------|
| <i>Chapter 5 (Partial)</i> | <i>X. Wang, B. Zhou, Liquid water flooding process in proton exchange membrane fuel cell cathode with straight parallel channels and porous layer, Journal of Power Sources, 196 (2011) 1776-1794.</i> | <i>published</i> |

I certify that I have obtained a written permission from the copyright owner(s) to include the above published material(s) in my thesis. I certify that the above material describes work completed during my registration as graduate student at the University of Windsor.

I declare that, to the best of my knowledge, my thesis does not infringe upon anyone's copyright nor violate any proprietary rights and that any ideas, techniques, quotations, or any other material from the work of other people included in my thesis, published or otherwise, are fully acknowledged in accordance with the standard referencing practices. Furthermore, to the extent that I have included copyrighted material that surpasses the bounds of fair dealing within the meaning of the Canada Copyright Act, I certify that I have obtained a written permission from the copyright owner(s) to include such material(s) in my thesis.

I declare that this is a true copy of my thesis, including any final revisions, as approved by my thesis committee and the Graduate Studies office, and that this thesis has not been submitted for a higher degree to any other University or Institution.

ABSTRACT

Fundamental understanding of liquid water behaviours in the cathode of proton exchange membrane fuel cells (PEMFC) contributes to the investigation of the liquid water management in PEMFCs. In this work, a three-dimensional two-phase flow model using volume of fluid method (VOF) with dynamic contact angle (DCA) is developed through user defined function (UDF) codes and validated by comparing the simulation results with experimental results available from the literature. An improvement is proposed and implemented for the Hoffman function to calculate local DCAs. By employing this methodology, gas-liquid phenomena inside the cathode of PEMFCs with porous layer and different gas flow field designs are studied and compared with the numerical models without consideration of DCA, namely with static contact angles (SCA).

DEDICATION

To my beloved parents.

ACKNOWLEDGEMENTS

I would like to express my feeling of gratitude to my advisor, Dr. Biao Zhou. I thank him for providing me the opportunity to join in his laboratory and pursue my M. A. Sc. degree in University of Windsor. His guidance, suggestions, and encouragement helped me greatly in my research during these two years.

I would like to give sincere thanks to Dr. Tirupati Bolisetti and Dr. Ronald M Barron for serving in my thesis committee and contributing their time and efforts. Thank Dr. Amir Fartaj for chairing my oral defence.

I am grateful to Simo Kang, as my research partner and roommate. Also thanks to who helped and showed their kindness to me in the MAME department and in the University of Windsor.

Finally, special thanks are given to my mother Chengfang Jing and father Jianqun Wang. Thank you so much for supporting me and loving me heart and soul. It is my luck and honour to be your daughter.

TABLE OF CONTENTS

| | |
|---|-----------|
| DECLARATION OF PREVIOUS PUBLICATION | iii |
| ABSTRACT | iv |
| DEDICATION | v |
| ACKNOWLEDGEMENTS | vi |
| LIST OF FIGURES | ix |
| LIST OF TABLES | xi |
| NOMENCLATURE..... | xii |
| 1. INTRODUCTION | 1 |
| 1.1. Principle of a Fuel Cell | 1 |
| 1.2. Features of Proton Exchange Membrane Fuel Cell..... | 2 |
| 1.3. Water Management Problem in Proton Exchange Membrane Fuel Cells..... | 3 |
| 1.4. Dynamic Contact Angle Effects on Liquid Water Transport..... | 3 |
| 1.5. Objectives | 5 |
| 1.6. Outline of Thesis..... | 6 |
| 2. LITERATURE REVIEW | 7 |
| 3. NUMERICAL METHODOLOGY | 10 |
| 3.1. Brief Model Description | 10 |
| 3.2. Governing Equations and Volume of Fluid (VOF) Method | 10 |
| 3.3. Implementation of Dynamic Contact Angle | 12 |
| 3.4. Improvement of Hoffman Function | 12 |
| 4. NUMERICAL MODEL VALIDATIONS | 14 |
| 4.1. Volume of Fluid (VOF) Method Validation..... | 14 |
| 4.2. Dynamic Contact Angle Methodology Validations | 14 |
| 4.2.1. Slug Flow in Rectangular Micro-channel..... | 15 |
| 4.2.1.1. Brief Description | 15 |
| 4.2.1.2. Validation | 16 |
| 4.2.1.3. Dynamic Contact Angle Effects | 21 |
| 4.2.1.4. Mass Flowrate, Surface Tension, and Viscosity Effects..... | 22 |
| 4.2.2. Impact of Droplet on Smooth Glass..... | 24 |
| 4.2.2.1. Brief Description | 24 |
| 4.2.2.2. Comparisons | 25 |
| 4.2.2.3. Dimple Phenomenon..... | 27 |
| 4.3. Summary..... | 27 |
| 5. GAS-LIQUID PHENOMENA IN PROTON EXCHANGE MEMBRANE FUEL CELLS WITH PARALLEL DESIGN..... | 28 |
| 5.1. Numerical Model Setup..... | 28 |
| 5.1.1. Geometry Domain | 28 |
| 5.1.2. Boundary Conditions | 29 |
| 5.1.3. Grid Independency | 30 |
| 5.2. Liquid Water Transport in Parallel Model without Dynamic Contact Angle..... | 30 |
| 5.2.1. General Process | 30 |

| | | |
|----------|--|-----------|
| 5.2.2. | Emerging Process..... | 32 |
| 5.2.2.1. | Liquid Water Emerging from Peripheral Areas of Lands and Frames | 32 |
| 5.2.2.2. | Dean Vortex Evolution..... | 35 |
| 5.2.3. | Draining Process in Outlet Channel | 36 |
| 5.3. | Liquid Water Transport in Parallel Model with Dynamic Contact Angle | 37 |
| 5.3.1. | General Process | 37 |
| 5.3.2. | Emerging Process..... | 40 |
| 5.3.2.1. | Liquid Water Emerging Mainly from Middle of the Interface under Channels | 40 |
| 5.3.2.2. | Dean Vortex Evolution..... | 42 |
| 5.3.3. | Draining Process in Outlet Channel | 46 |
| 5.3.4. | Liquid Water Amount and Pressure over Time..... | 49 |
| 5.4. | Comparison and Summary | 50 |
| 6. | GAS-LIQUID PHENOMENA IN PROTON EXCHANGE MEMBRANE FUEL CELLS WITH STIRRED TANK REACTOR (STR) DESIGN..... | 52 |
| 6.1. | Numerical Model Setup..... | 52 |
| 6.1.1. | Computational Domain | 52 |
| 6.1.2. | Boundary Conditions..... | 53 |
| 6.1.3. | Grid Independency | 54 |
| 6.2. | Liquid Water Transport in STR Model without Dynamic Contact Angle | 54 |
| 6.2.1. | General Process | 54 |
| 6.2.2. | Emerging Process..... | 57 |
| 6.2.2.1. | Liquid Water Emerging Tranquilly in Porous Layer..... | 57 |
| 6.2.2.2. | Liquid Water Distribution in Plenum | 59 |
| 6.3. | Liquid Water Transport in STR Model with Dynamic Contact Angle..... | 62 |
| 6.3.1. | General Process | 62 |
| 6.3.2. | Emerging Process..... | 65 |
| 6.3.2.1. | Liquid Water Surging in Porous Layer | 65 |
| 6.3.2.2. | Liquid Water Distribution in Plenum | 69 |
| 6.4. | Comparison of Liquid Water Amount and Gauge Pressure..... | 74 |
| 6.5. | Summary..... | 76 |
| 7. | CONCLUSIONS..... | 77 |
| | REFERENCES | 79 |
| | VITA AUCTORIS..... | 83 |

LIST OF FIGURES

| | |
|--|----|
| Figure 1-1 Principle of a fuel cell | 1 |
| Figure 1-2 An exploded view of PEMFC components | 3 |
| Figure 1-3 Definition of dynamic contact angle | 4 |
| Figure 3-1 The calculated values of original and revised Hoffman function | 13 |
| Figure 4-1 Comparison of liquid water behaviours between numerical simulation and the experiment at $t = 0.400s$ [33] | 14 |
| Figure 4-2 Numerical and experimental slug flow model conducted by Fang et al. [46] | 16 |
| Figure 4-3 Results comparison between Case2 (second row) and experiment (first row) | 17 |
| Figure 4-4 Results comparison between Case4 and experiment | 18 |
| Figure 4-5 (a-m) Slug flow movements with velocity field in Case2 | 20 |
| Figure 4-6 (a-b) Liquid distribution with DCA on the bottom wall in Case2 | 22 |
| Figure 4-7 Experimental setup for droplet impact model [41] | 24 |
| Figure 4-8(a-c) Results comparison of droplet impact model | 25 |
| Figure 4-9 Results comparison between SCA and DCA model of glycerine impact | 26 |
| Figure 4-10 Enlarged experimental results from Sikalo and Ganic [40] | 26 |
| Figure 4-11(a-b) Depression phenomenon (liquid volume fraction with corresponding DCA on the glass at $0.002424 s$) | 27 |
| Figure 5-1 Computational domain of Parallel model | 29 |
| Figure 5-2(a-j) General liquid water transport in Parallel-SCA model | 32 |
| Figure 5-3(a-c) Liquid water distribution near interface in Parallel-SCA model | 34 |
| Figure 5-4 Extract a plane from Parallel computational domain at $Y=0.0012m$ | 34 |
| Figure 5-5(a-c) Emerging process on plane at $Y = 0.012 m$ in the Parallel-SCA model | 35 |
| Figure 5-6(a-h) Draining process in the Parallel-SCA model | 37 |
| Figure 5-7(a-j) General liquid water transport in the Parallel-DCA model | 39 |
| Figure 5-8(a-c) Liquid water distribution near interface in the Parallel-DCA model | 41 |
| Figure 5-9 Contact angle on porous layer walls in the Parallel-DCA model at $0.254 s$ | 42 |
| Figure 5-10 Contact angle on channel sidewalls in the Parallel-DCA model at $0.337s$ | 42 |
| Figure 5-11(a-c) Emerging process on plane at $Y = 0.012 m$ in the Parallel-DCA model | 43 |
| Figure 5-12(a-b) Comparison of Dean Vortex evolution in No.7 parallel channel | 46 |
| Figure 5-13(a-j) Draining water deformation in Parallel-DCA model | 49 |
| Figure 5-14 Liquid water amount in the Parallel-DCA model over time | 50 |
| Figure 5-15 Gauge pressure in the Parallel-DCA model over time | 50 |
| Figure 5-16(a-b) Liquid water and velocity distribution on three planes ($Y = 0.006 m, 0.012 m,$ and $0.018 m$) at $0.1 s, 0.5s$ | 51 |
| Figure 6-1 Computational domain of STR model | 52 |
| Figure 6-2(a-j) General liquid water transport in the STR-SCA model | 57 |
| Figure 6-3(a-f) Liquid water transport in porous layer in the STR-SCA model | 59 |
| Figure 6-4(a-f) Liquid water distribution on plenum plane near interface ($Z = 0.00031 m$) in the STR-SCA model | 60 |
| Figure 6-5(a-b) Pressure distribution with velocity on plenum plane near interface ($Z = 0.00031 m$) in the STR-SCA model (unit: Pa) | 61 |

| | |
|---|----|
| Figure 6-6(a-j) General liquid water transport in the STR-DCA model..... | 65 |
| Figure 6-7(a-f) Liquid water transport in porous layer in the STR-SCA model | 67 |
| Figure 6-8(a-d) Liquid water and velocity field near walls (partial) of porous layer at the beginning of emerging process | 68 |
| Figure 6-9(a-d) Dynamic contact angle effects on velocity change at the beginning of emerging process in the STR-DCA model..... | 69 |
| Figure 6-10(a-f) Liquid water distribution on plenum plane near interface (Z = 0.00031 m) in STR-SCA model..... | 70 |
| Figure 6-11(a-f) Liquid water distribution and contact angles on PL walls in the STR-DCA model | 73 |
| Figure 6-12(a-d) Liquid water distribution and contact angles on sidewalls in the STR-DCA model | 74 |
| Figure 6-13 Liquid water amount in the STR-SCA model over time..... | 75 |
| Figure 6-14 Liquid water amount in the STR-DCA model over time | 75 |
| Figure 6-15 Gauge pressure in the STR-SCA model over time | 76 |
| Figure 6-16 Gauge pressure in the STR-DCA model over time..... | 76 |

LIST OF TABLES

| | |
|---|----|
| Table 1-1 Relationship between contact angle and wettability | 4 |
| Table 4-1 Description of conducted cases in numerical slug flow model | 17 |
| Table 4-2 DCA effects on the slug flow model..... | 21 |
| Table 4-3 Air mass flowrate effects on the slug flow model | 22 |
| Table 4-4 Surface tension effects on the slug flow model | 23 |
| Table 5-1 Boundary conditions of the parallel model | 29 |
| Table 6-1 Boundary conditions of the STR model | 53 |

NOMENCLATURE

| | |
|------------------------|--|
| ρ | Density ($\text{kg}\cdot\text{m}^3$) |
| ε | Porosity |
| \mathbf{u} | Velocity vector ($\text{m}\cdot\text{s}^{-1}$) |
| S | Source term |
| s | Phase volume fraction |
| χ | Surface tension coefficient |
| K | Surface curvature (m^{-1}) |
| α | Permeability (m^2) |
| θ_D | Dynamic contact angle ($^\circ$) |
| θ_e | Contact angle in equilibrium ($^\circ$) |
| Ca | Capillary number |
| f_{Hoff} | Hoffmann function |
| f_{Hoff}^{-1} | Inversed Hoffmann function |
| f_{Hoff}^* | Improved Hoffmann function |
| x | Shift factor |
| μ | Dynamic viscosity ($\text{Pa}\cdot\text{s}$) |
| σ | Surface tension ($\text{N}\cdot\text{m}^{-1}$) |
| Vel | Contact line velocity ($\text{m}\cdot\text{s}^{-1}$) |

Subscripts

| | |
|-----|----------------------------|
| g | Gas phase |
| l | Liquid phase |
| c | Continuity (mass) equation |
| m | Momentum equation |

1. INTRODUCTION

1.1. Principle of a Fuel Cell

A fuel cell is an energy conversion device that directly converts chemical energy into electrical energy. It is regarded as a major alternative to traditional energy sources such as internal combustion engines.

A fuel cell consists of the anode, electrolyte, and cathode. The electrochemical reaction in a fuel cell can be divided into two half reactions, namely oxidation reaction in the anode and reduction reaction in the cathode. As illustrated in Figure 1-1, the principle of a fuel cell generating electricity can be summarized into several main steps. Firstly, reactants are supplied into the fuel cell—fuel in the anode and air in the cathode. Then, electrochemical reaction happens. Fuel molecules split into ions and electrons in the anode catalyst layer; when they arrive in the cathode, they react with supplied reactant in the cathode catalyst layer. During this electrochemical reaction, electrons move along an external circuit connecting between anode and cathode while ions go through the electrolyte, thus electricity is being generated. Finally, products are removed from the fuel cell. As long as hydrogen is supplied as fuel, the fuel cell can continuously generate electricity.

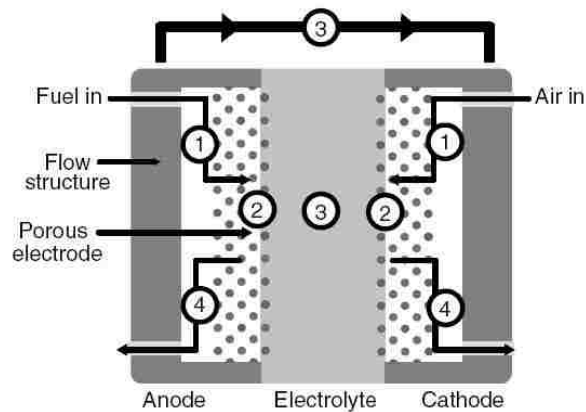


Figure 1-1 Principle of a fuel cell

(1) Reactant transport; (2) electrochemical reaction; (3) ionic and electronic conduction; (4) product removal [1]

Compared with combustion engines and batteries, fuels cells have many advantages such as high efficiency, high reliability, low noise, and low air pollution emission. However, some problems

including cost, power density, fuel storage, and other concerns cannot be neglected and need to be technically overcome before the commercialization of fuel cells.

1.2. Features of Proton Exchange Membrane Fuel Cell

Generally, fuel cells can be classified into five major types according to their different electrolyte: phosphoric acid fuel cell (PAFC), solid-oxide fuel cell (SOFC), alkaline fuel cell (AFC), molten carbonate fuel cell (MCFC), and proton exchange membrane fuel cell (PEMFC) [1]. Due to the advantages of low operating temperature, high power density, and good start-stop cycling durability, PEMFC is considered one of the potential candidates for commercialization.

PEMFCs use a thin polymer membrane as its electrolyte. Hydrogen is supplied to the anode as fuel, and catalytically split into protons and electrons. The protons carrying ionic charge go through the membrane to the cathode side, while the electrons move along the external circuit that connects two electrodes, generating electricity with direction defined as opposite to the electrons movements. When the protons and electrons arrive in the cathode, they react with oxygen molecules in the supplied air, generating water and heat. The electrochemical reactions in a PEMFC are shown as below.

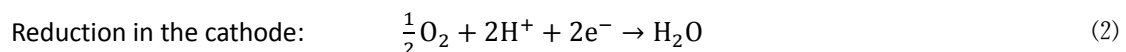
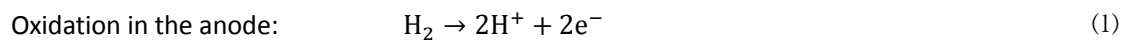


Figure 1-2 shows the exploded view of PEMFC components. The interconnector is used to connect single cells in a fuel cell stack. In the middle of a cell is the membrane which looks like plastic wrap. The anode and cathode in a cell share the same structure, including catalyst and gas diffusion layer (GDL), which are both porous layers, fixed by the gasket between the membrane and bipolar plate. In the bipolar plate, there are many channels with different designs to distribute the gas flow and remove redundant liquid water.

For the last two decades, although many different types of flow field channel designs have been developed by industrial and academic researchers, most of them can be classified into three categories: parallel, serpentine, and interdigitated. These different designs were proposed to

resolve the major concerns, such as pressure drop, uniformity of reactant gas distribution, and water management.

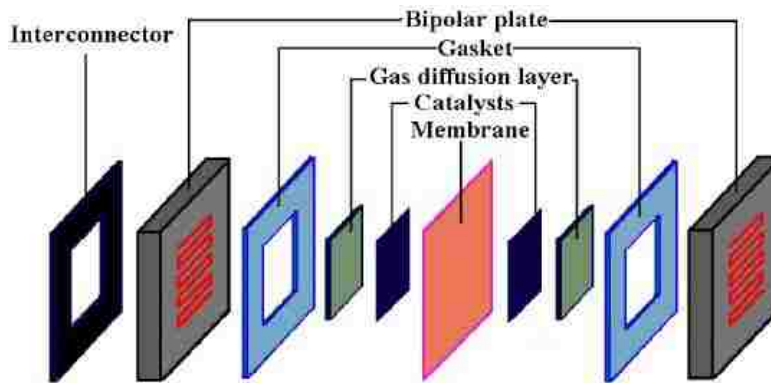


Figure 1-2 An exploded view of PEMFC components
(Source from: <http://www.energi.kemi.dtu.dk/Projekter/fuelcells.aspx>)

1.3. Water Management Problem in Proton Exchange Membrane Fuel Cells

As the main product in the cathode, water plays an important role in PEMFC's performance. Because the operating temperature of a PEMFC is under 100°C (usually 50-100°C), water generated from the electrochemical reaction easily condenses into liquid water and accumulates in the cathode. Too much liquid water may flood the GDL and channels, hinder mass transport of gas from reaction, resulting in an increase of voltage loss. On the other hand, if there is too little water so that the membrane is unable to get hydrated enough to ensure adequate protons go through it; the generated voltage is decreased as well. Therefore, the amount of water and distribution is a key point affecting the performance of PEMFC, either too much or too little will drop the power output. That is why water management, especially liquid water management, is a critical issue in the improvement of PEMFC's performance and the commercialization that attracts interests of academic researchers and engineers. Thus, it is important to get an understanding of gas-liquid dynamics inside PEMFCs with different flow field designs.

1.4. Dynamic Contact Angle Effects on Liquid Water Transport

Contact angle, which is defined as the angle between the liquid/gas interface and the solid surface (Figure 1-3), plays an important role in gas-liquid dynamics.

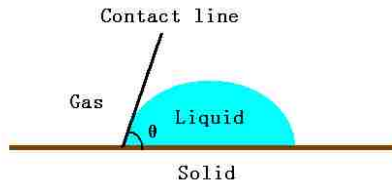


Figure 1-3 Definition of dynamic contact angle

The value of contact angle is determined by the relationship between three phases (gas, liquid, and solid), as shown in Table 1-1. When contact angle equals to 0° , the solid surface is perfect wetted. When contact angle equals to 180° , then the solid surface is dry, namely perfect non-wetted. These are the boundaries of contact angle on a flat surface. When the contact angle is between 0° and 90° , the surface is hydrophilic, which means liquid tends to be adhesive to the surface. When the contact angle is greater than 90° , the surface is hydrophobic, which means liquid tends to be repulsive to the surface.

In the equilibrium, contact angle can be expressed by Young's equation,



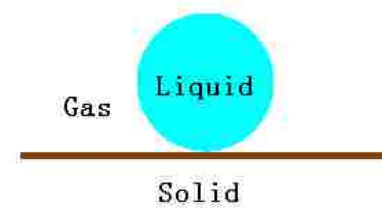
$$\gamma \cos \theta_e = \gamma_{SG} - \gamma_{SL} \quad (3)$$

where γ_{SG} and γ_{SL} are the surface tension of solid/gas interface and solid/liquid interface respectively [2].

In the case of a droplet resting on a flat surface without shape change, the contact angle is referred to as static contact angle (SCA) θ_s . Before the contact line (between three phases) starts to move, the maximum of contact angle is the advancing contact angle θ_a , while the minimum is the receding contact angle θ_r . These three angles are only in the equilibrium situation.

Table 1-1 Relationship between contact angle and wettability

| Contact angle | Wettability | Shape of droplet |
|---------------|-------------|------------------|
| $\theta = 0$ | flood | |

| | | |
|------------------------------------|-------------|--|
| $0 < \theta < 90^\circ$ | hydrophilic |  |
| $90^\circ \leq \theta < 180^\circ$ | hydrophobic |  |
| $\theta = 180^\circ$ | dry |  |

However, from many experiments conducted, the surrounding gas flow is unsteady, resulting in changing of surface tension between gas and liquid, so the contact angle is unlikely to stay in equilibrium. This type of contact angle with a moving contact line is defined as dynamic contact angle (DCA), which is a critical parameter in the boundary of unsteady two-phase flow model, rather than a property of the surface material itself. In investigating the gas-liquid dynamics in PEMFC, especially when the geometry of fuel cell size is quite small, namely in a microscopic view, where surface tension weights much on the gas/liquid distribution and transport, it is not proper to set SCA as a boundary condition, instead, DCA should be considered.

1.5. Objectives

The objective of this thesis is to investigate gas-liquid phenomena inside the cathode of PEMFCs with different flow field design, considering the effects of DCA. The numerical study is conducted by means of volume of fluid (VOF) method to tracking the interface of liquid using FLUENT, which is a powerful computational fluid dynamics (CFD) software. DCA is introduced to the model through user defined function (UDF) code with an improvement of the Hoffman function which is used to account for DCA. The present methodology is validated by comparison with experiments, and implemented to study the emerging, flooding, drainage process, and detailed gas-liquid phenomena inside parallel PEMFC and stirred tank reactor (STR) PEMFC.

1.6. Outline of Thesis

The present thesis is divided into seven chapters. The content for each chapter are summarized as below:

Chapter 1: To introduce the fundamental knowledge of fuel cell and proton exchange membrane fuel cell (PEMFC), illustrate the importance of investigating the gas-liquid phenomena in water management of PEMFC, and depict dynamic contact angle (DCA) effects on liquid water transport.

Chapter 2: To make literature reviews on the models of PEMFC and DCA, and address three problems that need improvement in the end of this chapter.

Chapter 3: To introduce the model used in this work, including VOF method and computation of DCA. An important improvement of the Hoffman function, which is used to account for DCA in this model, is presented as well.

Chapter 4: To validate the numerical model. Two experiments carried out by other researchers, slug flow in a rectangular micro-channel, and glycerine droplet impacting glass, are selected for comparisons. Similar numerical models are conducted with the same geometry and operating conditions as the experiments, by using presented methodology in this work.

Chapter 5: To investigate gas-liquid phenomena in the cathode of PEMFC with parallel flow field design. Two cases are conducted using VOF model; one is to apply DCA on multiple wall boundaries, the other is without DCA, namely using static contact angle (SCA). The results for each case and comparisons between two cases are described.

Chapter 6: To investigate gas-liquid phenomena in the cathode of the PEMFC with stirred tank reactor (STR) design. Similar to Chapter 5, two cases with/without DCA are conducted. Results and comparisons between two cases are described.

Chapter 7: To summaries the conclusions to the present work, and propose future improvements.

2. LITERATURE REVIEW

As a critical research topic for optimizing the performance of PEMFCs, liquid water management is attracting great efforts from many scientists and engineers [3]. During last two decades, a great number of research works have been reported by scholars and academic researchers. Singh et al. [4] developed a two-dimensional model to investigate the transport process in PEMFCs to improve water management. Previously reported analyses by Djilali and Lu [5] also studied the influence of heat and water transport in PEMFCs. A three-dimensional numerical model of straight gas-flow channels was studied by Dutta et al. [6]. Cha et al. [7] discussed the influence of oxygen concentration along gas flow channels on PEMFC performance by examining the steady-state gas-flow phenomena in micro parallel flow channels. Kulikovskiy [8] numerically acquired the gas concentration of a steady-state flow along channels in a similar way. These studies, however, did not investigate the influence of liquid water. Yi et al. [9] indicated that water vapor condensation is a common phenomenon on both sides of a PEMFC. You and Liu [10] pointed out that a multi-phase model must be employed in order to obtain more practical results. Both of these previous studies considered water in vapor form [9, 10]. Wang et al. [11] conducted a two-phase, multi-component mixture model of the cathode of a PEMFC to deal with the problems in a single- and in a two-phase co-existence region, and introduced a technique to measure in situ water distribution [12]. Recently, Dawes et al. [13] investigated the effects of water with a three-dimensional mixture model of a PEMFC, and Luo et al. [14] also developed a topologically equivalent pore network model to study the transport of liquid water in PEMFC. These contributions to investigating the water management in PEMFC are summarized by some review papers. Wang [15] provided a review of fundamental models for PEMFC, and Weber et al. [16] gave a review of modeling transport. Li et al. [17] outlined progress and achievements of water management investigation in PEMFC, particularly concentrating on water flooding issues. The most recent overview was detailed summarized by Jiao et al. [3].

From one-dimensional to multi-dimensional, from single phase to multi-phase, many numerical models were developed based on computational fluid dynamics (CFD) approaches. Two fluid model [18-20] and mixture model [21-23] were considered close to the real two-phase flow in a PEMFC, and were widely used by many researchers to estimate two-phase concentrations in the

cathode of PEMFCs. However, these two models are difficult to simulate detailed liquid water transport. Thus, the volume of fluid (VOF) model was proposed by Quan et al. [24] to simulate the liquid water removal process by tracking the interface between liquid and gaseous phases.

By means of the VOF model, between 2006 and 2008, a series of numerical simulations of two-phase flow in several different types of cathode flow field design were conducted [25-29]. The water removal characteristics [25-27], the effects of electrode wettability on liquid water behaviour [28], and accelerated numerical test of liquid behaviour [29] were investigated, but neither conventional porous layers nor electrochemical reactions were included in these analyses. In 2008, a general model for PEMFC has been proposed [30] and applied in the following years to investigate two-phase flow coupled with electrochemical reactions, water transport through the membrane, and heat and mass transfer for single cells with different flow field designs [30, 31] and a 3-cell stack [32]. However, this technique requires excessive computational time. In order to minimize computational time, a simplified model [33] was developed by neglecting electrochemical reactions and heat transfer effects since computational results were hardly affected for the aim of simulating liquid water transport. And detailed experimental validation [33] was performed by direct optical visualization method to capture the motion and deformation of liquid water. Then liquid water emerging and flooding process inside a PEMFC cathode with straight parallel [34] and interdigitated [35] flow field designs were studied by means of this validated simplified model.

All the studies with VOF model mentioned above [24-34] are implemented with static contact angles on the wall boundaries. The contact angle is determined by the liquid-gas interface on a solid material, changing with the moving contact line. Djilali et al. [36, 37] noted that liquid water behaviour on a gas diffusion layer (GDL) surface is affected by the contact angle when water emerges from a pore, and conducted validation experiments by observation method [38]. Therefore, it is not proper to use static contact angles as a wall boundary condition for the unsteady, two-phase flow model of the cathode of PEMFC.

Sikalo et al. [39] investigated DCA of spreading droplet using VOF model, through both numerical and experimental method. In his work, Sikalo made a review of other models being used to

compute DCA. He also presents a widely used formula describing the relationship between DCA and the contact angle in equilibrium. However, they are not dependent on the actual flow field. Therefore, Sikalo considered the correlation proposed by Kistler [42] which is an application of Hoffman function. Miller [43] used this method which is best fit to existing experiment results, and developed a user defined function (UDF) code for pursuing the movements of a droplet in a single straight channel with implement of DCA on the boundary condition. All models conducted with DCA so far are in simple geometry domains, usually considering only one boundary with DCA. Moreover, the DCA values were not extracted within a specific time and location.

To summarize the literature review, some key points can be addressed as follows:

- (1) Compared with existing numerical models to study the gas-liquid dynamics in the cathode of PEMFC, VOF model has the advantage of tracking interface between liquid and gas so that the liquid water distribution and transport can be described in details. However, most of the simulation of PEMFC cathode using VOF model have not considered DCA as wall boundaries.
- (2) Although many researchers studied the contact angle effects on gas-liquid dynamics and proposed many correlations to account for DCA, most of models are not dependent on actual flow field. The method with application of Hoffman function is considered as the best fitting of experiment results, and good for depicting DCA depending on real flow field.
- (3) Some researchers use Hoffman function in their flow model; however, nearly all these models are simple geometry, usually a straight channel or a plate, and couple DCA only on a single wall boundary. No one has applied this method on the model of PEMFC cathode with complex flow field design to investigate the liquid water transport.

In present work, all issues proposed above are solved. The methodology is going to be presented and validated by comparison with selected experiments. By use of this method, the gas-liquid phenomena with/without DCA in the cathode of PEMFC with complex flow field, i.e., parallel design, and stirred tank reactor (STR) design developed by Benziger et al. [44] and Hogarth and Benziger [45], are studied and present later.

3. NUMERICAL METHODOLOGY

3.1. Brief Model Description

According to the work of Sikalo et al. [39] and Miller [43], and the validated VOF method [23-25], with an improvement of Hoffman function, a numerical model are developed by implementation of DCA on multiple wall boundaries through a UDF code.

The numerical model of PEMFC cathode is 3-dimensional, unsteady, two-phase flow, solved by use of FLUENT software, which is a powerful engineering tool to solve CFD problems. Air is treated as the gaseous phase while liquid water is treated as the liquid phase, and these two-phases are assumed to be immiscible. VOF method is applied to track the liquid-gas flow interface. A UDF code is applied to introduce the source term, apply DCA to multiple wall boundaries, and extract analytic parameter values, such as liquid water amount, interface pressure, and local DCA.

The fluid flow is laminar because of the low flow velocity and the small size of the channels. Heat transfer and phase change are not considered in this study in order to reduce the computation time. The unsteady, laminar flow model is governed by the following continuity (mass) and momentum equations to describe the fluid flow transport process.

3.2. Governing Equations and Volume of Fluid (VOF) Method

The continuity (mass) equation is expressed as

$$\frac{\partial(\varepsilon \rho)}{\partial t} + \nabla \cdot (\varepsilon \rho \mathbf{u}) = S_c \quad (4)$$

where ε is the porosity of the porous media (in the gas flow channels $\varepsilon = 1$). The first term on the left hand side is the transient term representing the change of mass with time, the second term is the convection term standing for the change in mass flux, and the term on the right hand side is the mass source term. In this study, S_c equals to zero because phase changes are not taken into account in this model.

In the VOF model, the volume fractions of gas and liquid water are defined as s_l and s_g respectively, and

$$s_l + s_g = 1 \quad (5)$$

The variables and properties are shared by both phases and are calculated by a volume-averaged method. The average density and viscosity for each computational cell which is between those of gaseous and liquid phases, are defined as

$$\rho = s_l \rho_l + s_g \rho_g \quad (6)$$

and

$$\mu = s_l \mu_l + s_g \mu_g \quad (7)$$

In the VOF model, the interface between gaseous and liquid phases is tracked by solving a continuity equation for the volume fraction of liquid water,

$$\frac{\partial(\epsilon s_l \rho_l)}{\partial t} + \nabla \cdot (\epsilon s_l \rho_l \mathbf{u}) = 0 \quad (8)$$

which is solved over the entire computational domain. Then the volume fraction of gas is computed based on the Equation (5).

A single momentum equation is implemented in the VOF model, and the gaseous phase and the liquid phase share the same resulting velocity field,

$$\frac{\partial}{\partial t} (\epsilon \rho \mathbf{u}) + \nabla \cdot (\epsilon \rho \mathbf{u} \mathbf{u}) = -\epsilon \nabla p + \nabla \cdot [\epsilon \mu \nabla \mathbf{u}] + \epsilon S_m \quad (9)$$

In this momentum equation, the terms on the left hand side represents the change of momentum with time and the advection momentum flux respectively, while the terms on the right hand side are the momentum due to pressure, viscosity and sources.

In the model, the surface tension force, as well as gravity force, is coupled to the momentum equation by the source term S_m , expressed as

$$S_m = \rho g + \chi K \frac{\rho \nabla s_l}{(\rho_l + \rho_g)/2} \quad (10)$$

where χ is the surface tension coefficient and K is the surface curvature.

In the porous layer, one more term $-\frac{\mu}{\alpha} \mathbf{u}$, where α stands for the permeability of the porous layer, is added in the source term because of the viscous effect through the porous layer, or the Darcy force. So the complete source term for the momentum equation in the porous layer is

$$S_m = \rho g + \chi K \frac{\rho \nabla s_l}{(\rho_l + \rho_g)/2} - \frac{\mu}{\alpha} \mathbf{u} \quad (11)$$

3.3. Implementation of Dynamic Contact Angle

Dynamic contact angle is implemented in this model by means of compiling the UDF code to the wall boundary conditions, which is developed based on the empirical expressions contributed by Kistler [42] and the work of Sikalo et al. [39] and Miller [43],

$$\theta_D = f_{\text{Hoff}}[Ca + f_{\text{Hoff}}^{-1}(\theta_e)] \quad (12)$$

The dynamic contact angle θ_D is determined by the Hoffmann function f_{Hoff} , and varies according to the capillary number Ca and a shift factor $f_{\text{Hoff}}^{-1}(\theta_e)$ gained from the inverse of the Hoffman function under equilibrium when the contact angle on the wall boundary is fixed, namely, static contact angle (SCA) [39], i.e.,

$$f_{\text{Hoff}}(x) = \arccos \left\{ 1 - 2 \tanh \left[5.16 \left(\frac{x}{1+1.31x^{0.99}} \right)^{0.706} \right] \right\} \quad (13)$$

The capillary number Ca , which shows a relationship between viscosity μ and surface tension σ , affected by the contact line velocity which is extracted instantaneously from the model during iteration, is defined as

$$Ca = \frac{(Vel)\mu}{\sigma} \quad (14)$$

3.4. Improvement of Hoffman Function

The Hoffman function (Equation (13)) is an empirical formula derived through experiments [46]. It is noticed that, in all of these experiments, the shift factor x , whose range of value is between 0 and 1 since it is a proportion parameter, was obtained for corresponding contact angles between 15° and 120° . This means the applicability of the Hoffman function with a contact angle in the range of $[0^\circ, 15^\circ]$ or $[120^\circ, 180^\circ]$ has not been validated by experiments.

During the current investigation, the Hoffman function (Equation (13)) was found to be imprecise. The value of x was found to be greater than 1, that is beyond the upper limit of proportional parameter value range, with a corresponding contact angle within the range of (171°, 180°).

Therefore, a correction term $-0.013x$ is added to the original Hoffman function to improve the applicability. The revised Hoffman function is expressed as

$$f_{\text{Hoff}}^*(x) = \arccos \left\{ 1 - 0.013x - 2 \tanh \left[5.16 \left(\frac{x}{1+1.31x^{0.99}} \right)^{0.706} \right] \right\} \quad (15)$$

A comparative plot with both the original and revised Hoffman functions is presented in Figure 3-1, from which it can be seen that the revised Hoffman function has a wider range of applicability in the numerical simulation. Consequently, the UDF code implemented the revised Hoffman function to compute DCAs for specific wall conditions with different SCA in equilibrium and compile them to this 3-D, unsteady model.

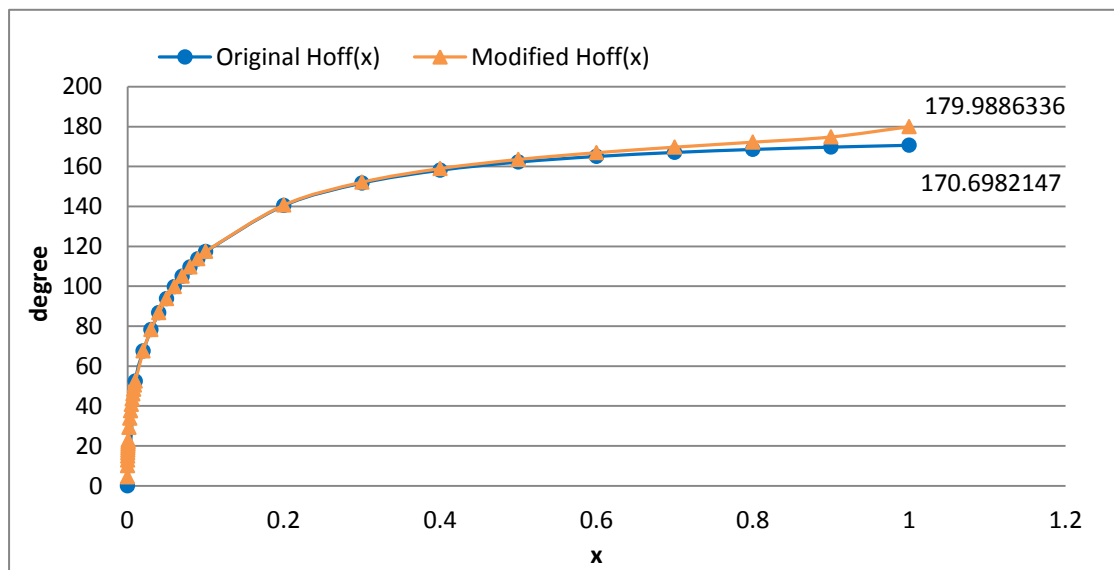


Figure 3-1 The calculated values of original and revised Hoffman function

4. NUMERICAL MODEL VALIDATIONS

4.1. Volume of Fluid (VOF) Method Validation

A simplified VOF model, in which electrochemical reactions and heat transfer effects were neglected to minimize the computational time, is validated by Le et al. [33]. Numerical simulation was used to predict the liquid water behaviours in the cathode of a PEMFC with serpentine channels and a porous layer. A detailed experimental validation of this simplified cathode model was performed by direct optical visualization method to capture the motion and deformation of liquid water with high spatial and temporal resolutions. A sample comparison from this validation is shown in Figure 4-1 (the left panel shows the experimental setup, while the right panel shows the numerical simulation), which demonstrates that the results from this simplified model are in good agreement with the corresponding experiments.

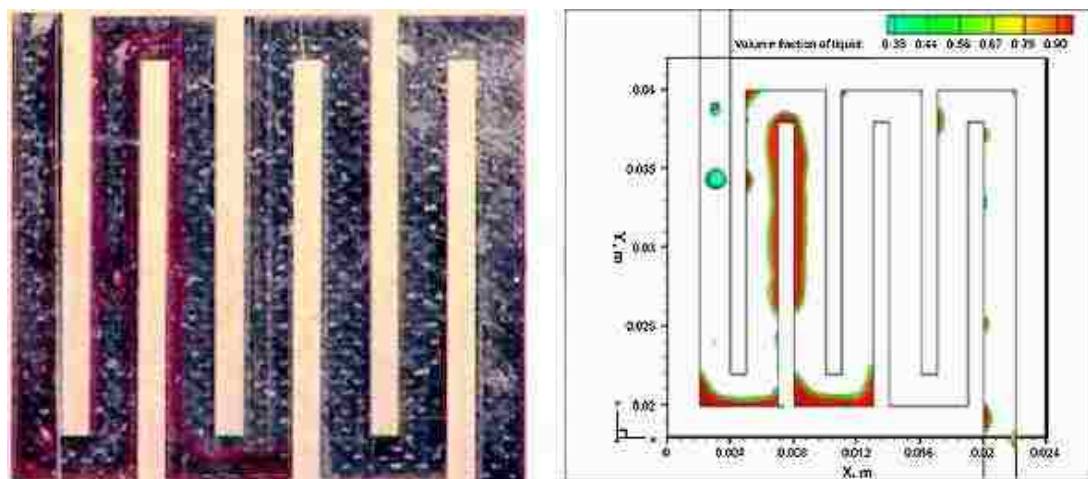


Figure 4-1 Comparison of liquid water behaviours between numerical simulation and the experiment at $t = 0.400s$ [33]

4.2. Dynamic Contact Angle Methodology Validations

Two interesting experiments were selected for the validation of the present model with DCA coupling on wall boundary conditions. One was conducted by Fang et al. [47], who studied slug flow in a micro-channel; the other was carried out by Sikalo and Ganic [40] and Sikalo et al. [41], which was impact of a droplet on glass. In order to validate the methodology proposed in this thesis, a series of comparative cases were conducted with the same geometry and operated

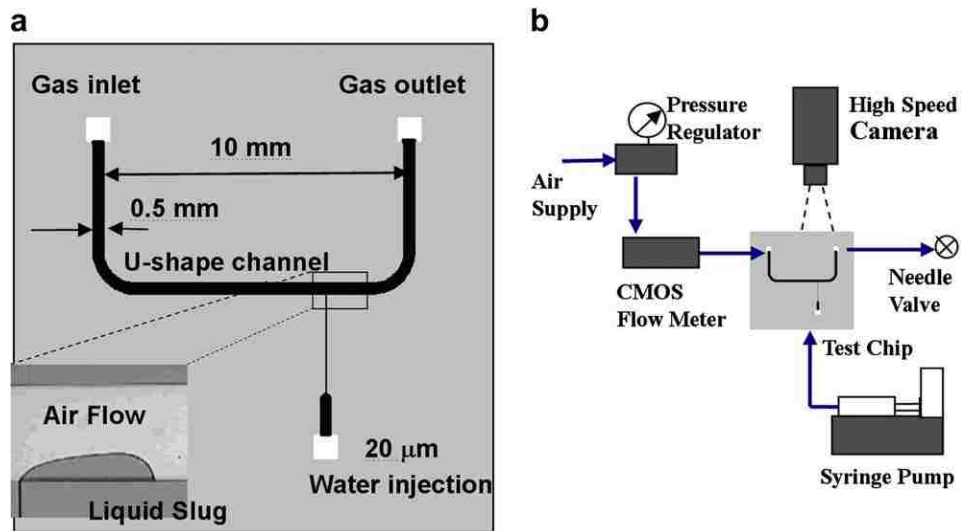
under the same conditions with the experiments. Detailed validated cases are presented, and the comparisons of results between numerical and experimental models are addressed in the following section.

4.2.1. Slug Flow in Rectangular Micro-channel

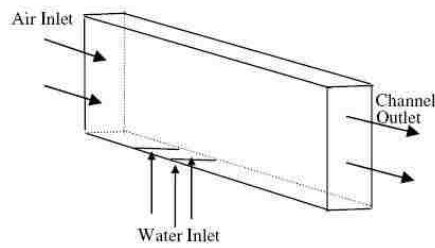
4.2.1.1. Brief Description

Fang et al. [47] conducted experiments of liquid slug flow in micro-channels with several of input parameters. The schematic of the experimental setup is shown in Figure 4-2(1). The test bench is a 10 mm long, 0.5 mm wide U-shape micro-channel made of silicon. A three-dimensional, two-phase flow model of this experiment also using VOF theory was validated by Fang et al. [47]. The computational domain is shown in Figure 4-2(2), which is a straight channel with 5 mm in length and has a cross-section of $500 \mu\text{m} \times 45 \mu\text{m}$. Air is supplied to the inlet boundary of the channel as gaseous phase with a constant velocity of 15.56 ms^{-1} , while liquid water is supplied to the liquid inlet boundary, which is located at one third of the length from the air inlet, as liquid phase with a constant velocity of 0.09 ms^{-1} . The initial contact angle on the bottom wall of the channel is 105° . DCA was implemented on the wall boundary as well, but in the computational manner differing from the methodology presented in this thesis. The experimental and numerical results supplied by Fang et al. [47] are shown in Figure 4-2(c) (gas is coloured in blue, and liquid is coloured in red).

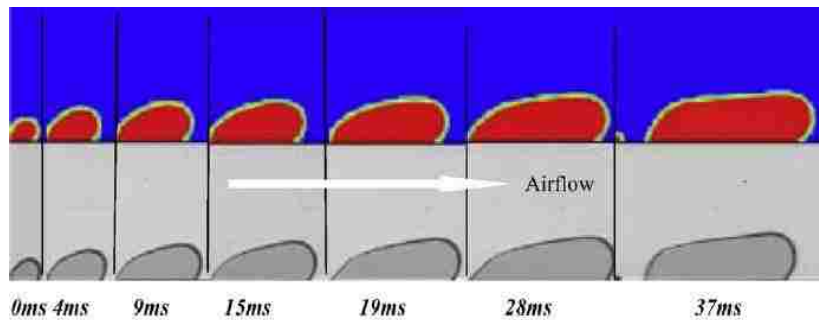
The methodology presented in this thesis has the advantage of plotting local contact angle with time (i.e. DCA field) compared to Fang's model. In order to validate the present methodology, a numerical model with same dimensions and operating parameters but different way of computing and compiling DCA to the wall boundary is conducted. Both air and liquid water are supplied in constant mass flowrate to get the same velocities as those set in Fang's model.



(a) Experimental setup



(b) Numerical model setup



(c) Numerical (first row) and experimental (second row) results

Figure 4-2 Numerical and experimental slug flow model conducted by Fang et al. [46]

4.2.1.2. Validation

Figure 4-3 shows comparison of results between Fang's experiments and the present numerical model with DCA (Case2 in Table 4-1). The liquid water slug shapes between the two models are

similar, but the time directions in the two models are hard to fit well. In order to investigate the potential factors that influence the comparison, a series of slug flow testing cases with changes of parameters were conducted with descriptions as in Table 4-1. These cases will be compared and discussed by groups in the following section.

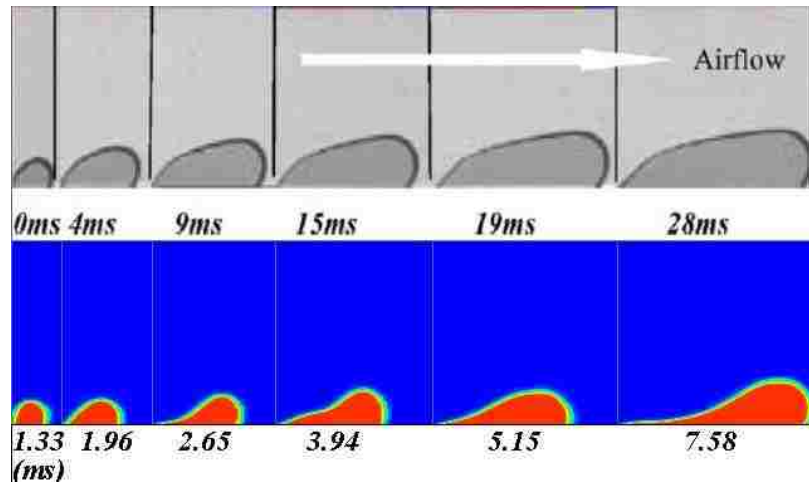


Figure 4-3 Results comparison between Case2 (second row) and experiment (first row)

Table 4-1 Description of conducted cases in numerical slug flow model

| Description No. | Contact angle | Gas flowrate | Surface tension | Viscosity |
|--------------------|---------------|--------------|-----------------|-----------|
| Case1 | SCA | Original | Original | Original |
| Case2 | DCA | Original | Original | Original |
| Case3 | DCA | 2/3 | Original | Original |
| Case4 | DCA | 1/3 | Original | Original |
| Case5 | DCA | Original | 110% | Original |
| Case6 | DCA | Original | 200% | Original |
| Case7 | DCA | Original | Original | 109% |
| Case8 | DCA | Original | Original | 200% |

In the simulation processes, it was found that the numerical results in Case4, in which the gas flowrate was lowered to 1/3 of the origin, fit well with the experimental results on both slug movements and time instances, as shown in Figure 4-4. In some way, the experiment may have some unavoidable errors, and the experimental results are only partially provided, not

presented entirely so that some phenomena might be neglected. Therefore, the gas flowrate may be the factor affecting the validation results.

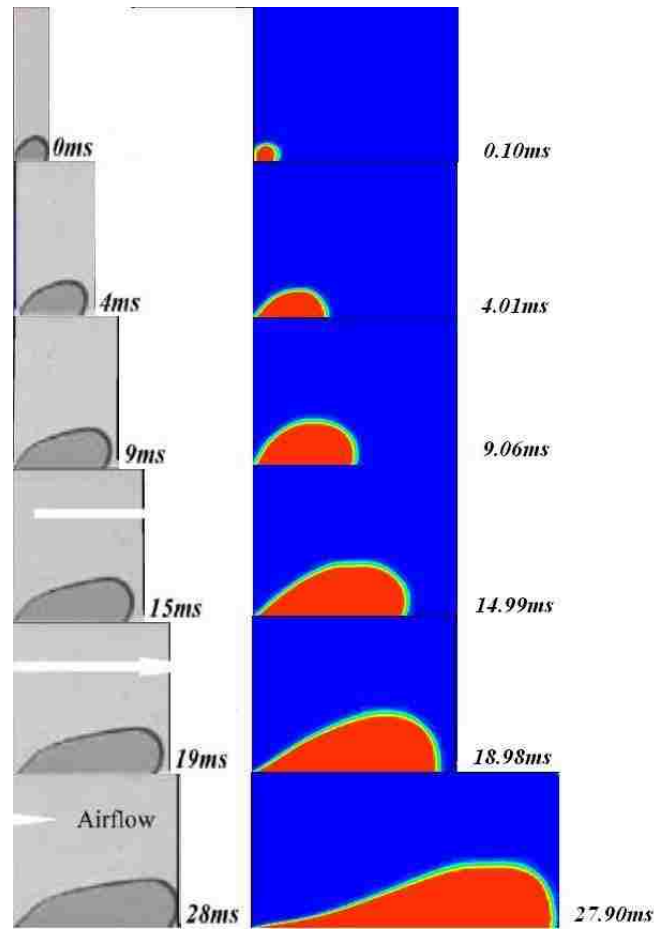
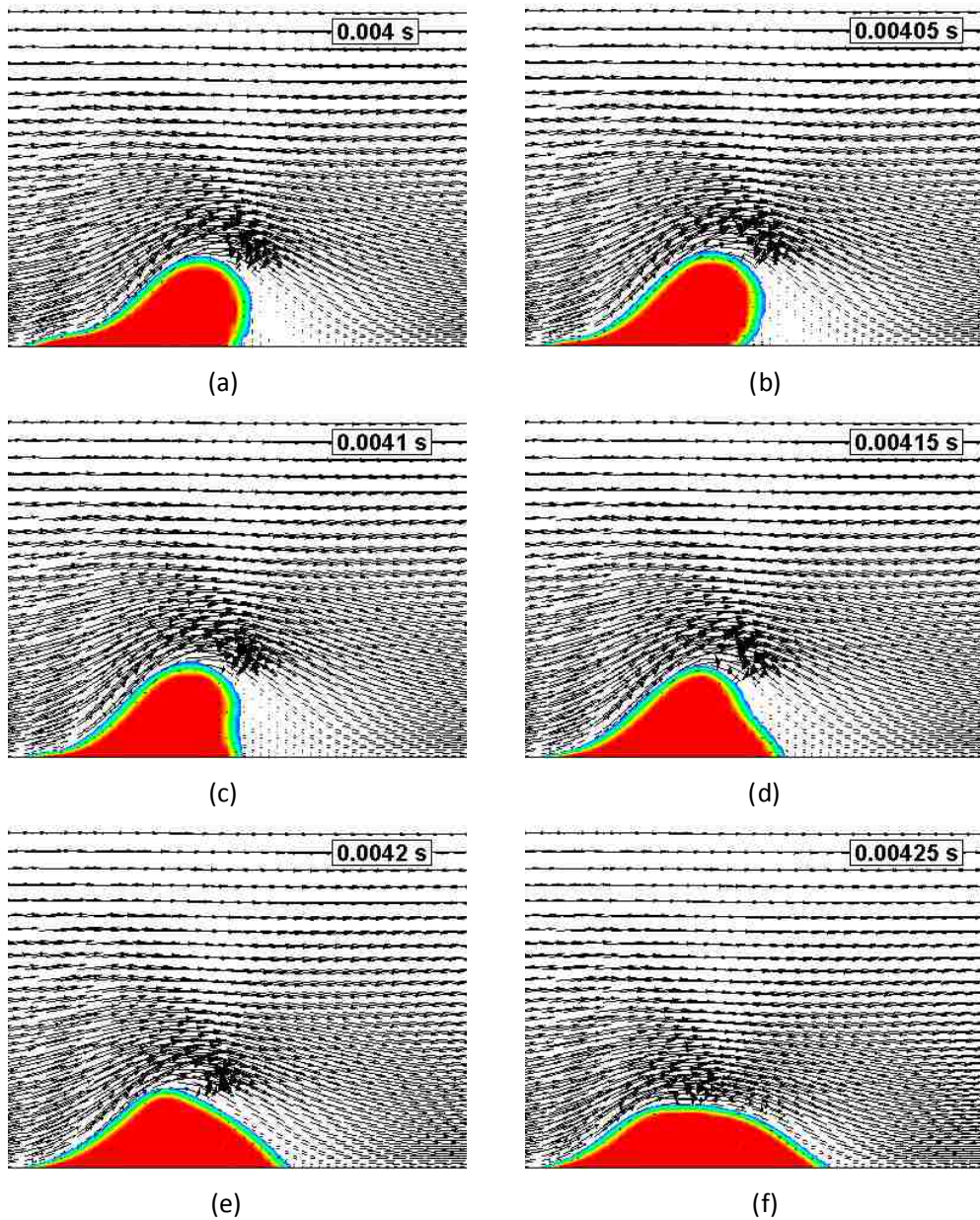


Figure 4-4 Results comparison between Case4 and experiment

Since the provided experimental results are fragmentary, the whole movement cannot be tracked from Fang's paper. Whereas, an interesting worm crawling phenomenon of liquid water can be observed periodically in the numerical model with DCA implementation (Case2) (as shown in Figure 4-5). This phenomenon divides into accumulation, flattening, re-accumulation; three sub-processes caused by a cooperation of pressure, surface tension, and shear stress. In the accumulation sub-process (Figure 4-5(a, b)), surface water in the slug is driven by the air flow, and the head of slug is held by the surface tension. The air flow converges and increases the velocities in the windward side of the water slug resulting in a high pressure area; while the velocities at the leeward of the slug decreases forming a low pressure area. This pressure drop in the air flow and the shear stress on the water slug result in flattening of the slug (Figure 4-5(c-g)).

The pressure between the two sides decreases. With surface of the water slug increasing, the surface tension increases as well. So the slug recedes a little bit as shown in Figure 4-5(h-l), and then re-accumulates. The worm crawling phenomenon reveals the interaction between the two phases, i.e., gas and liquid water. The different slug shape at difference time instances corresponds to the relationship between pressure, surface tension, and shear stress at specific time instance.



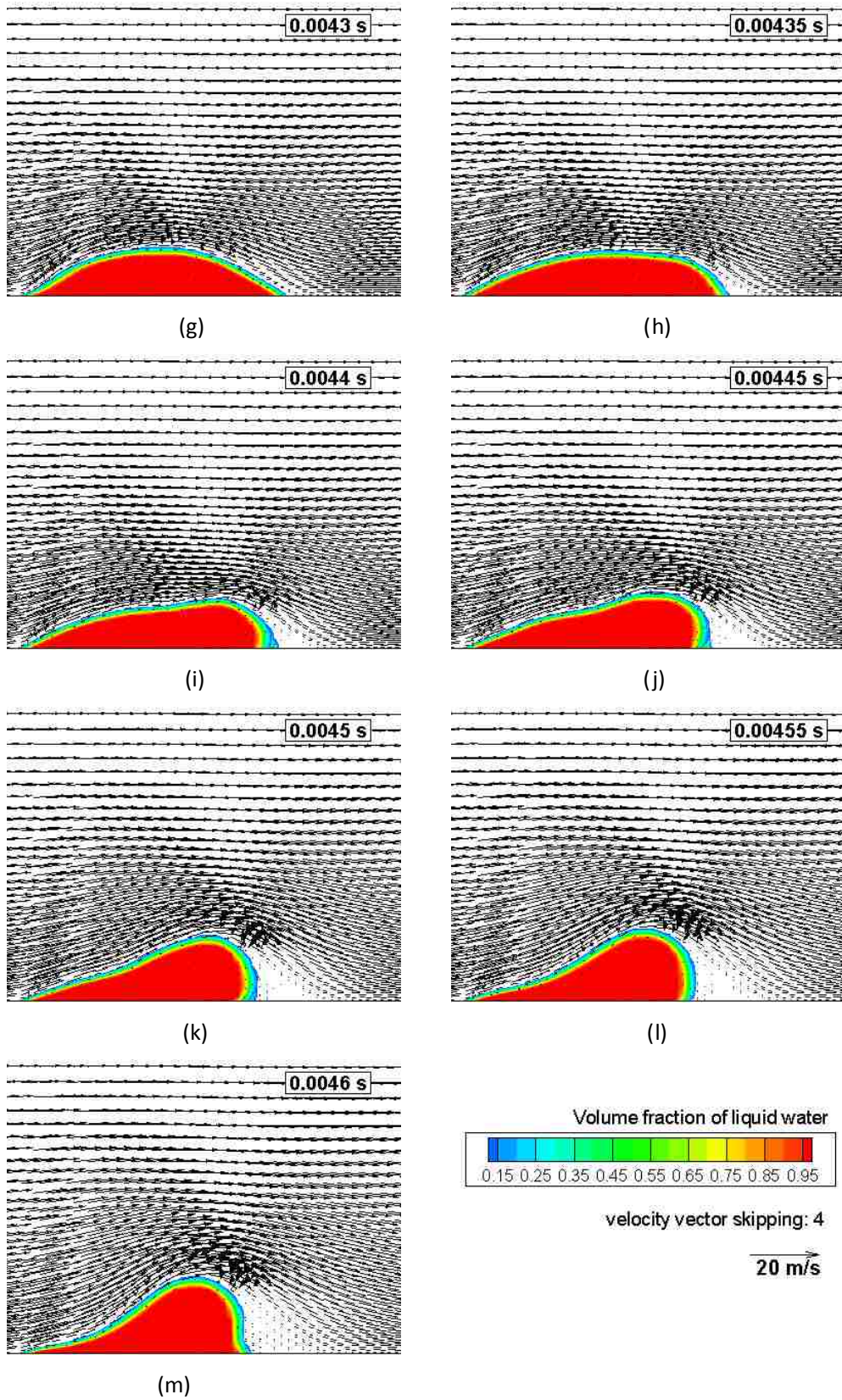









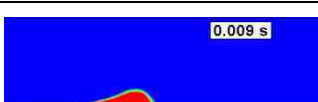


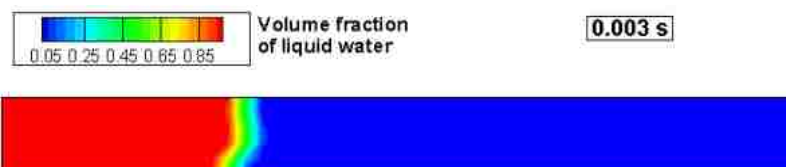
Figure 4-5 (a-m) Slug flow movements with velocity field in Case2

4.2.1.3. Dynamic Contact Angle Effects

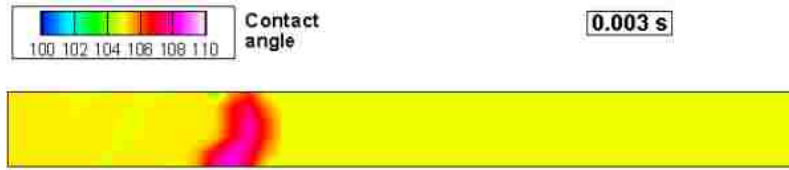
The numerical model with contact angle fixed, namely SCA (Case1), is conducted with other settings identical to the DCA case (Case2). The comparison of results between Case1 and Case2 are presented in Table 4-2. It can be noticed that the contact line between gas and water in Case1 is held at a steady angle, which violates the physics of slug motion. Since the velocities near the contact line change in magnitude and/or direction over time, the contact angle on the bottom wall should alter correspondingly, which affects the water transport in contrary because of changes in wall adhesion. Figure 4-6 shows the water distribution on the wall with corresponding DCAs at 0.03 s. The area where volume fraction of water shifts intensely has a large DCA difference because of the greater change of velocity.

Table 4-2 DCA effects on the slug flow model

| Time | Case1 SCA model | Case2 DCA model |
|------|---|--|
| 1 ms |  |  |
| 3 ms |  |  |
| 5 ms |  |  |
| 7 ms |  |  |
| 9 ms |  |  |



(a)















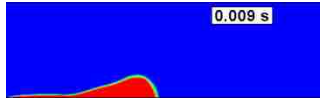


(b)

Figure 4-6 (a-b) Liquid distribution with DCA on the bottom wall in Case2

4.2.1.4. Mass Flowrate, Surface Tension, and Viscosity Effects

The effects of gas mass flowrate are studied by conducting the numerical model with 1/3 percentage decrease gradually. Case 3 is the numerical model with 2/3 of original air mass flowrate, and Case 4 is the one with 1/3 of original air mass flowrate. These two cases are compared with the original air flowrate (Case2), shown in Table 4-3. All three cases are conducted with DCA implementation. From the results in Table 4-3, lower air mass flowrate leads to a longer time when water slug is stuck at the liquid inlet.













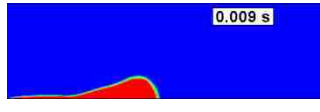
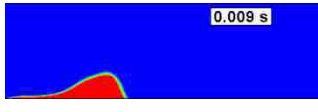

Table 4-3 Air mass flowrate effects on the slug flow model

| Time | Case2 Original DCA model | Case3 2/3 air mass flowrate | Case4 1/3 air mass flowrate |
|------|---|--|---|
| 1 ms |  |  |  |
| 3 ms |  |  |  |
| 5 ms |  |  |  |
| 7 ms |  |  |  |
| 9 ms |  |  |  |

Similarly, two cases with increase of surface tension are conducted and compared with the original DCA model (Case2). Case5 has the 10% increase on surface tension, while Case6 has an









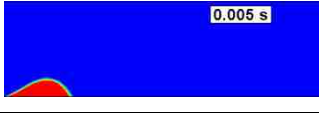
increase of 100%. From the comparison in Table 4-4, it can be noticed that with higher surface tension the slug prefers to be held near the liquid inlet field.

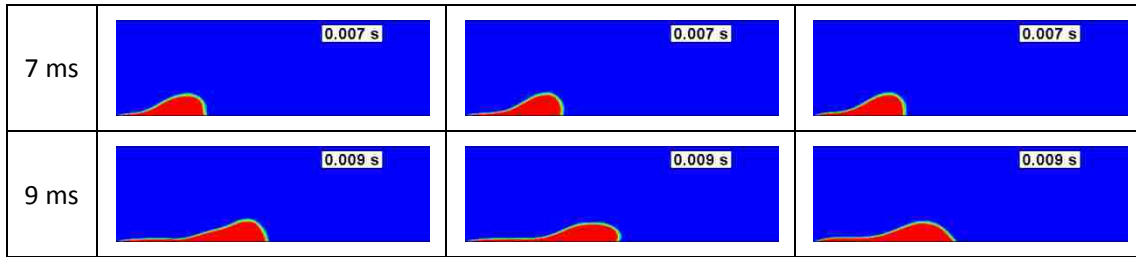
Table 4-4 Surface tension effects on the slug flow model

| Time | Case2 Original DCA model | Case5 110% surface tension | Case6 200% surface tension |
|------|---|--|---|
| 1 ms |  |  |  |
| 3 ms |  |  |  |
| 5 ms |  |  |  |
| 7 ms |  |  |  |
| 9 ms |  |  |  |

To study the effect of viscosity, Case7 has an increase of 9% and Case8 has an increase of 100%. Unlike previous groups with changing of air flowrate and surface tension, the change of viscosity does not have much influence on the transport of slug flow, with only slight altering in the shape, in other words, viscosity slightly affects the interaction of the two phases.

Table 4-5 Viscosity effects on the slug flow model

| Time | Case2 Original DCA model | Case7 109% viscosity | Case8 200% viscosity |
|------|---|--|---|
| 1 ms |  |  |  |
| 3 ms |  |  |  |
| 5 ms |  |  |  |



4.2.2. Impact of Droplet on Smooth Glass

4.2.2.1. Brief Description

Since the validation methodology is not reliable by comparing only to one experiment, another experiment was selected for the validation of the present model. Sikalo and Ganic [40] and Sikalo et al. [41] conducted a series of experiments of droplet impacting on a plate with different droplet and surface materials, and impact velocity given in Weber number. The experimental setup used by these researchers is shown in Figure 4-7.

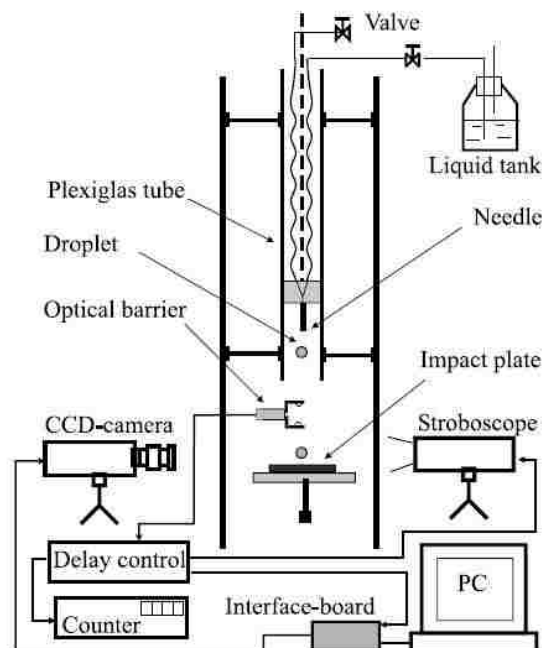


Figure 4-7 Experimental setup for droplet impact model [41]

One of the experiments was selected for validation of the present methodology in this thesis, which is an impact of glycerine droplet on a horizontal glass plate. The initial diameter of glycerine droplet is 2.45 mm, with density of 1220 kgm^{-3} , viscosity of $116 \text{ mPa}\cdot\text{s}$, and surface tension of 0.063 Nm^{-1} . The average surface roughness of glass is $0.003 \text{ }\mu\text{m}$, and the impact

Weber number is 391, which give a velocity of 3.635 ms^{-1} .

By sharing the same setting as in the experiment, a numerical model has been developed using the simplified VOF model, considering the DCA effects by compiling the UDF code on the wall boundary (which is glass in this model), for the sake of methodology validation. Another model, with only difference of fixing the contact angle on the wall (i.e., SCA), is conducted for comparison as well. The geometry of the numerical model is a cylinder with dimensions of 10 mm diameter and 4.0 mm height, with implementation of pressure-inlet boundary on the surface to simulate the surrounding atmosphere. The initial setting of contact angle on the glass (which is wall boundary) is 15° . The mesh size for this numerical model is 0.2 mm. Grid independency is determined by deducting 50% of the mesh size and the differences of results are very small.

4.2.2.2. Comparisons

Figure 4-8(a) is the experimental results from Sikalo and Ganic [40] captured by CCD camera at 0.100, 0.260, and 2.020 ms (the latest three profiles of droplet) with the starting time (0 s) at the moment of impact. The results of the numerical model with/without DCA effects are shown in Figure 4-8(b, c) with same dimension scales and time difference, in which the starting time is 0.4 ms earlier than that in experiments. Comparing the results from the three models, the results are similar between each other. Both the DCA and SCA models can simulate the experimental results well.

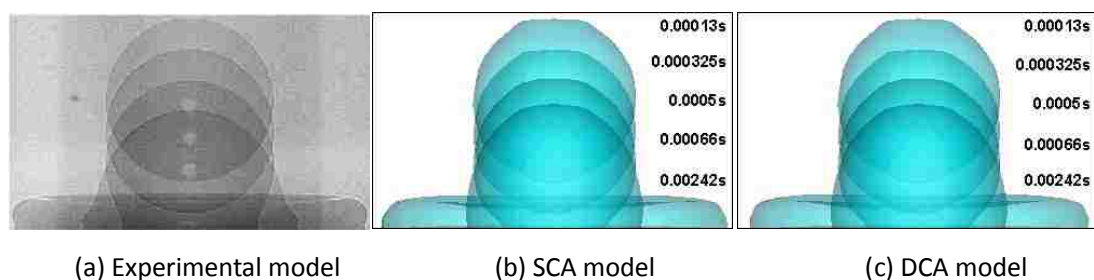


Figure 4-8(a-c) Results comparison of droplet impact model

(a) Experimental results at 0.100, 0.260, 2.020ms [40]

(b, c) Numerical results at 0.500, 0.650, and 2.420 ms (time direction with 0.4ms difference with experiments)

Although the numerical results are quiet similar between SCA and DCA model, there is still a

small difference, as shown in Figure 4-9, which illustrate an enlarged part of glycerine droplet spreading on the glass at 0.001s, 0.0015s, and 0.002s. By reference of marking rectangle in the figure, it can be observed that the joint of glycerine droplet and glass are slightly different. Compared to SCA model, the results in DCA model are closer to the experimental results as shown in Figure 4-10 which is an enlarged view of Figure 4-8(a).

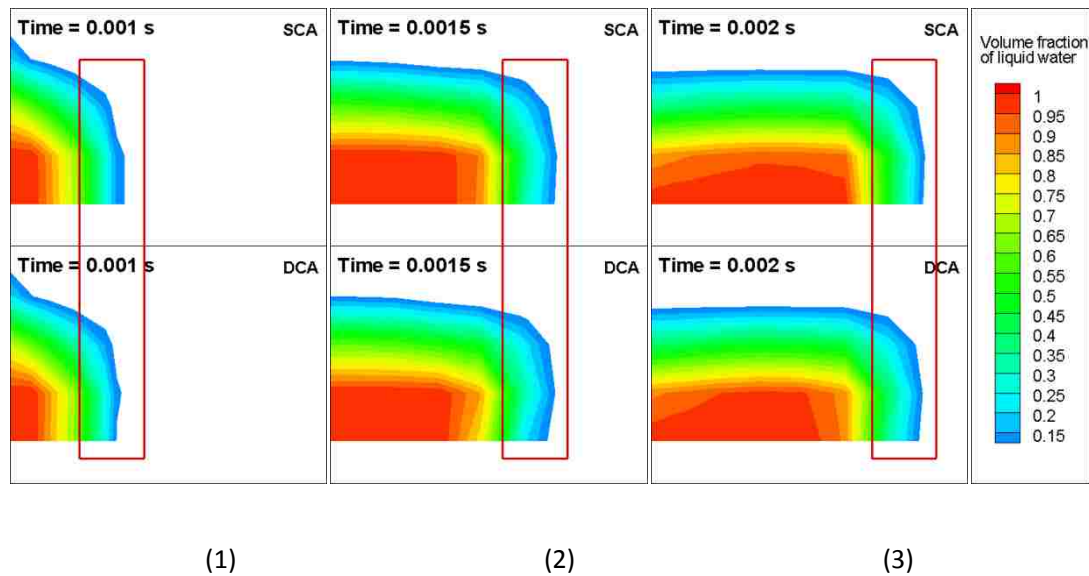


Figure 4-9 Results comparison between SCA and DCA model of glycerine impact

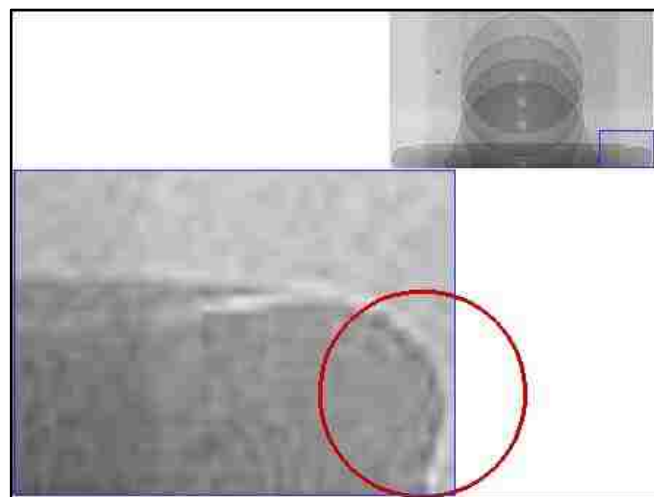


Figure 4-10 Enlarged experimental results from Sikalo and Ganic [40]

4.2.2.3. Dimple Phenomenon

When the glycerine droplet falls, the potential energy is converted to kinetic energy. When the droplet impacts the glass plate, its momentum alters greatly, both in magnitude and direction, so the droplet spreads on the glass. Because of the conservation of mass, there is no more glycerine supplied in the middle area, while the rim of the droplet is continuously spreading. Then the dimple phenomenon happens on the surface of the impacting droplet (Figure 4-11(a)). Figure 4-11(b) shows the corresponding DCAs (by cutting off the values of 15° (initial contact angle) and below) on the glass at the same time instance. In the middle area, the contact angles are smaller than other impacting areas revealing the strong hydrophilic wettability of these areas on the glass. Also the DCAs are much higher in the rim of the droplet, which demonstrates the intensive movement of glycerine there.

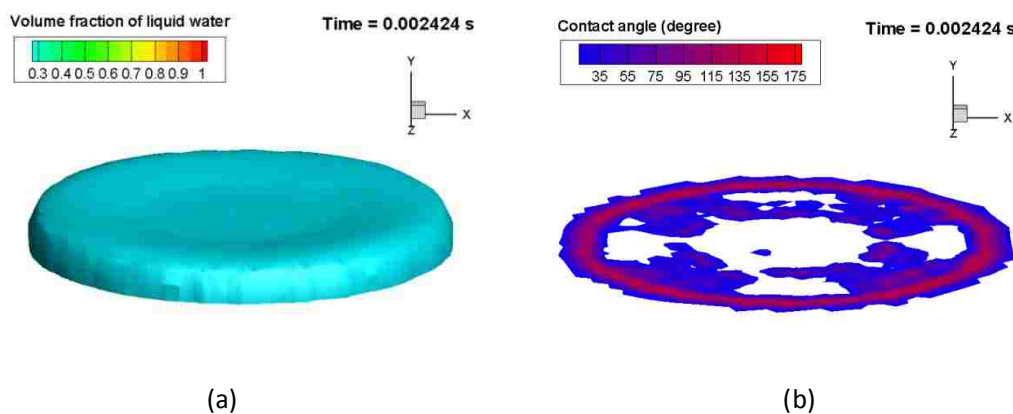


Figure 4-11(a-b) Depression phenomenon (liquid volume fraction with corresponding DCA on the glass at 0.002424 s)

4.3. Summary

The validation of the numerical methodology of VOF model with implementation of DCA is processed by conducting two series of models to compare the numerical results with experimental results. Two experiments, one is a water slug flow in a straight channel, the other is a glycerine droplet impact on glass, are selected for numerical model validation. For slug flow in a channel, numerical results partially fit experimental results; some potential factors affecting the results comparison exist. For the glycerine droplet impact on a glass plate, the numerical results fit very well with the experiments.

5. GAS-LIQUID PHENOMENA IN PROTON EXCHANGE MEMBRANE FUEL CELLS WITH PARALLEL DESIGN

5.1. Numerical Model Setup

As one of the major flow channel designs, parallel channels permit a low overall pressure drop between the gas inlet and the outlet [48]. Two numerical models, Parallel-SCA and Parallel-DCA, which share the same computational domain and operating conditions but with only difference on wall boundaries, are implemented in order to investigate the liquid water transport within this type of channel design by considering of DCA effects.

5.1.1. Geometry Domain

The numerical simulation domain for the parallel model represents a full-scale cathode side geometry of a single PEMFC. Figure 5-1 illustrates the schematic of the numerical simulation domain, which contains gas flow channels, including seven parallel channels with a 0.001 m distance between adjacent ones, and a porous layer whose porosity is 0.3. The dimensions of the entire computational domain are 0.06 m in X-direction, 0.024 m in Y-direction, and 0.002 m in Z-direction. The cross-section of the parallel channels is 0.002 m (in X-direction) \times 0.002 m (in Y-direction) \times 0.0017 m (in Z-direction). Main part of gas flow channels are attached to a 0.024 m (in X-direction) \times 0.024 m (in Y-direction) \times 0.0003 m (in Z-direction) porous layer with 0.002m frames on X-Y plane. These are the typical dimensions of a fuel cell component. A liquid water injection channel (LWIC) with dimensions of 0.0004 m (in X-direction) \times 0.0004 m (in Y-direction) \times 0.000725 m (in Z-direction) is positioned at the inlet joint (the joint of inlet channel and No.1 parallel channel) shown in Figure 5-1. This LWIC was used to simulate liquid water injection effects in previous studies [33]. In the present parallel model, the LWIC is blocked because there is no liquid water injected through it, and this geometry is kept so that the results of the current study (where the liquid water is supplied from the back surface of the porous layer as shown in Figure 5-1) can be compared to the results of previous studies (where liquid water injection is performed through the LWIC) in the future. The direction of gravity is along negative Z-axis, which is the normal direction to the porous layer.

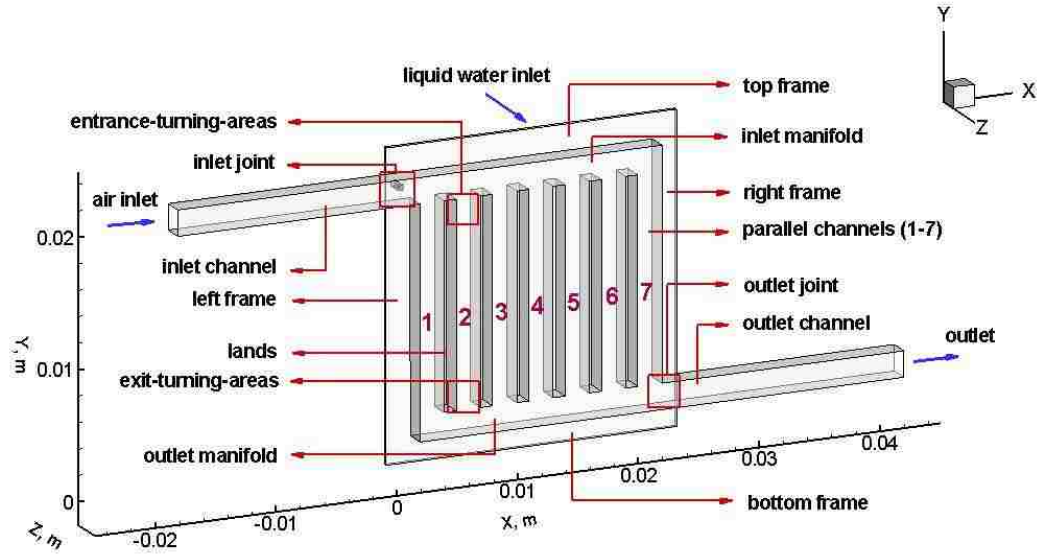


Figure 5-1 Computational domain of Parallel model

5.1.2. Boundary Conditions

The computational methodology is applied in the parallel model by means of specific boundary conditions as shown in Table 5-1. In Parallel-SCA model, initial contact angles for wall boundaries are fixed as constant; while in Parallel-DCA model, contact angles change with the change of flow field (i.e., dynamic contact angle (DCA)) during simulation through the UDF code coupling on the wall boundaries, and can be expressed as parameters associated with time and location.

Table 5-1 Boundary conditions of the parallel model

| Boundaries | | Type | Descriptions |
|--|---|-----------------|--|
| Liquid inlet (Back surface of porous layer) | | Mass flow inlet | Mass flowrate: $1.7 \times 10^4 \text{ kgs}^{-1}$ |
| Gas inlet | | Mass flow inlet | Mass flowrate: $2.0 \times 10^{-5} \text{ kgs}^{-1}$ |
| Outlet | | Pressure outlet | Pressure: 1 atm |
| Walls | Side walls of channels | Wall | No-slip, initial contact angle: 40° |
| | Upper walls of channels | Wall | No-slip, initial contact angle: 43° |
| | Walls of porous layer (walls under frames and lands) | Wall | No-slip, initial contact angle: 140° |

5.1.3. Grid Independency

The computational domain is meshed with 290,352 cells in total. The cell size is approximately 1.67×10^{-4} m in both X- and Y-directions, whereas the dimensions in Z-direction are 1.4×10^{-4} m in the gas flow channel domain and 5×10^{-5} m in the porous layer domain. Jiao et al. [26] implemented a grid check method by increasing and decreasing the number of grid cells by certain percentages. This cell size has been validated for PEMFCs by the comparison of numerical results with experimental results from the previous studies [33].

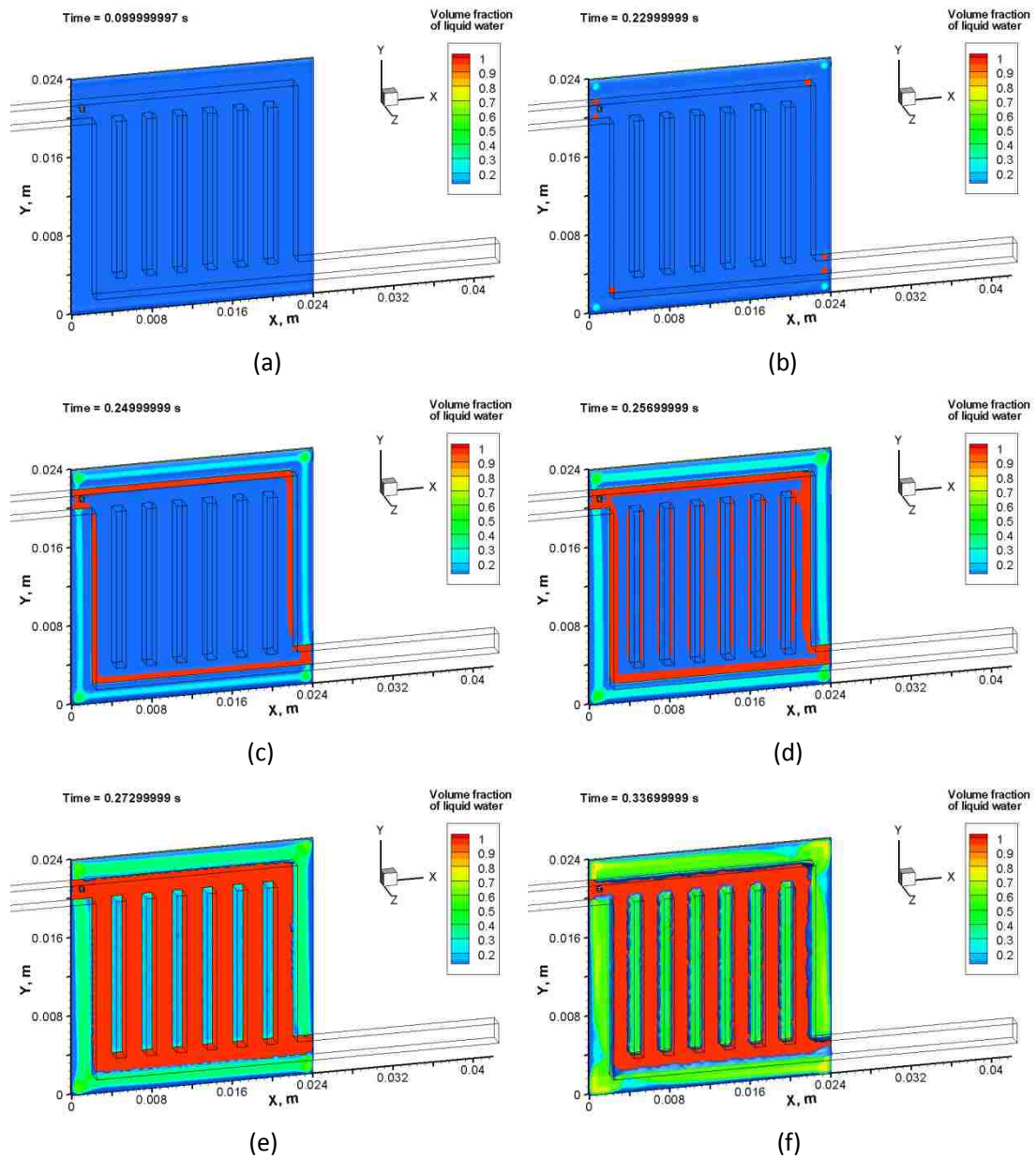
5.2. Liquid Water Transport in Parallel Model without Dynamic Contact Angle

5.2.1. General Process

Figure 5-2 shows the main process of liquid water movement over time for some selected time instants, where volume fraction of liquid water is expressed by colour-filled contours with iso-surface. The general process of liquid water transport can be divided into the following sub-processes:

- (1) Liquid water is supplied from the back surface of the porous layer by a constant mass flowrate to simulate the liquid water generation through electrochemical reaction (Figure 5-2(a)).
- (2) This supplied liquid water mounts up in the porous layer (Figure 5-2(b-d)), and reaches the top surface of the porous layer, i.e., the interface between the porous layer and channels, first at four corners of the interface under the channels domain (Figure 5-2(b)), then frame (Figure 5-2(c)), and also the edges of each parallel channel (Figure 5-2(d)).
- (3) Liquid water from the porous layer emerges into the gas flow channels from the peripheral edges of lands (defined as the solid between adjacent parallel channels on bipolar plate) and the peripheral edges of the channels domain (Figure 5-2(e-f)).
- (4) The liquid water emerging into the channels accumulates at the outlet joint (defined in Figure 5-1) (Figure 5-2(g)).
- (5) The liquid water at outlet joint starts to move into the outlet channel (Figure 5-2(h)).

(6) Liquid water drains out through the outlet channel (Figure 5-2(i)). With liquid water increasing, some parts of the gas flow channels get flooded, and the second draining process happens (Figure 5-2(j)).



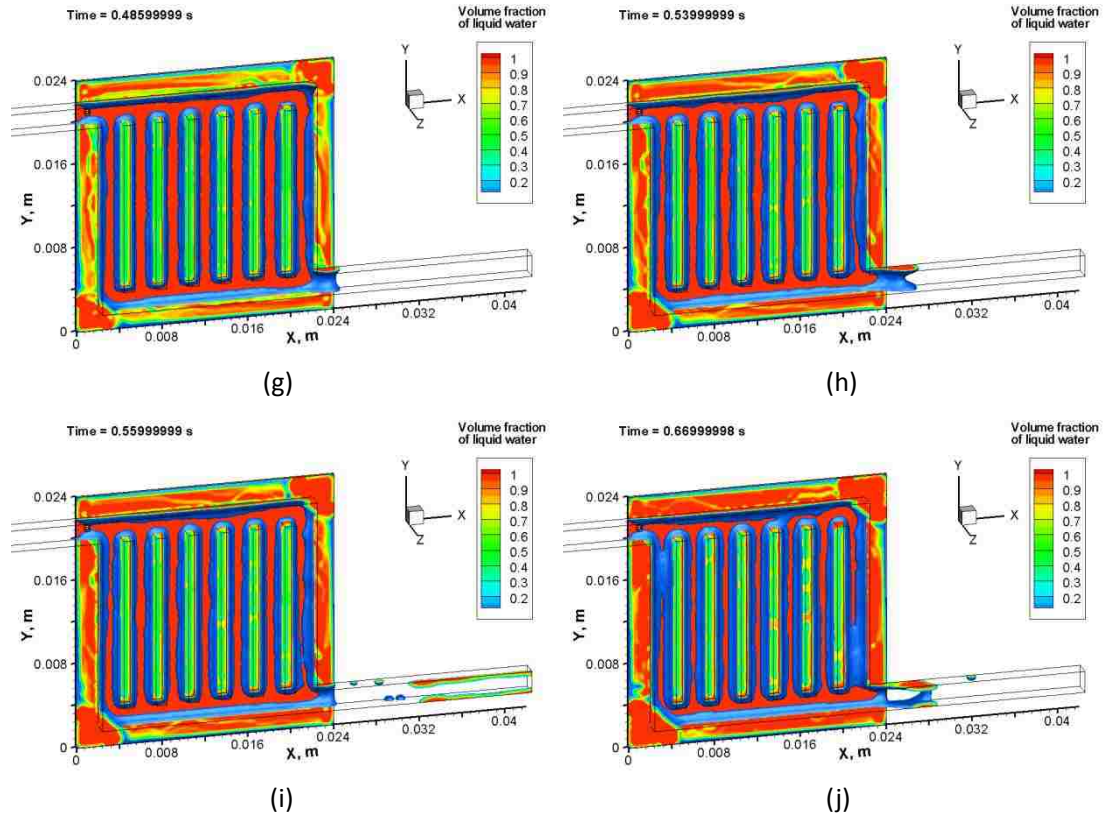


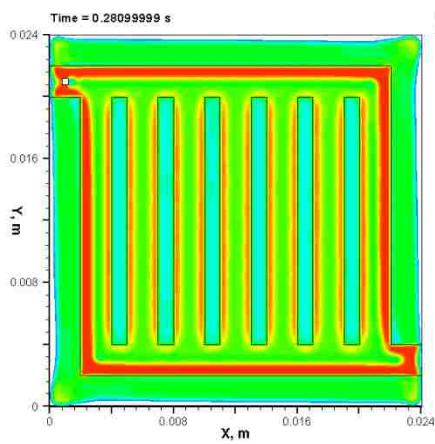
Figure 5-2(a-j) General liquid water transport in Parallel-SCA model

5.2.2. Emerging Process

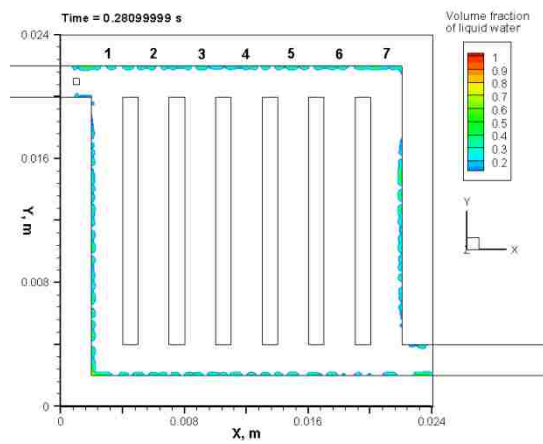
5.2.2.1. Liquid Water Emerging from Peripheral Areas of Lands and Frames

As shown in Figure 5-3, two planes are extracted near the interface ($Z = 0.00029$ m and $Z = 0.00031$ m), from the porous layer domain (left column in Figure 5-3) and channel domain (right column in Figure 5-3) respectively, to explain the pattern of liquid water emerging into the gas flow channels from the porous layer. From Figure 5-3(a-1), it can be noticed that liquid water initially reaches the interface under peripheral edges of the channel domain, and tends to accumulate under the area of edges of lands (the ribs between two adjacent parallel channels as defined in Figure 5-1). At the same time instance, liquid water already enters into the gas flow channels from the peripheral edges of the channel domain (Figure 5-3(a-2)). Soon after, liquid water emerges from the edges of lands (Figure 5-3(b-2)), meanwhile the areas underneath the lands in the porous layer domain are filled with liquid water (Figure 5-3(b-1)). As time goes by, more liquid water is generated, passes through the interface, and enters into the channels (Figure 5-3(c)).

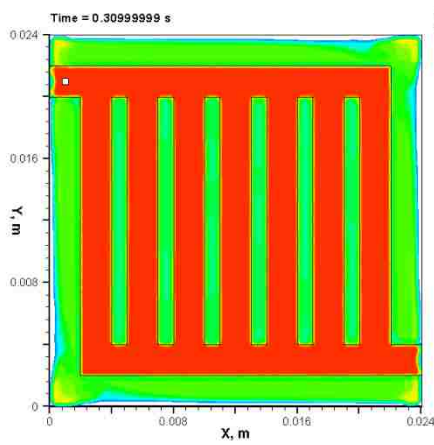
The detailed emergence and growth of liquid water from the porous layer into channels can be explained by Figure 5-5. The left column in Figure 5-5 shows the liquid water volume fraction on the plane extracted from computational domain at $Y = 0.012$ m (Figure 5-4); and the right column is the enlarged area of No. 7 parallel channel on the plane, showing velocity as well as volume fraction with different reference velocity vectors. The liquid water from the porous layer enters into the channels from the edges of the lands because the liquid water generation rate is uniform on the back surface of the porous layer, but the liquid water underneath the lands cannot directly enter into the channels in the manner that the liquid water underneath the middle of the channels enters. Actually, the liquid water underneath the lands has to detour along the interface between the lands and the porous layer then into the channels because the lands are solid and only allow the conduction of electrons.



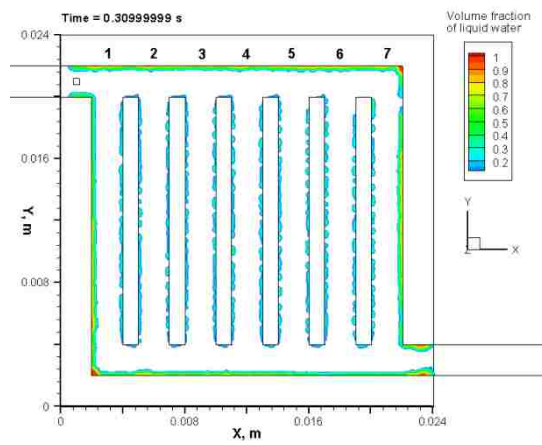
(a-1)



(a-2)



(b-1)



(b-2)

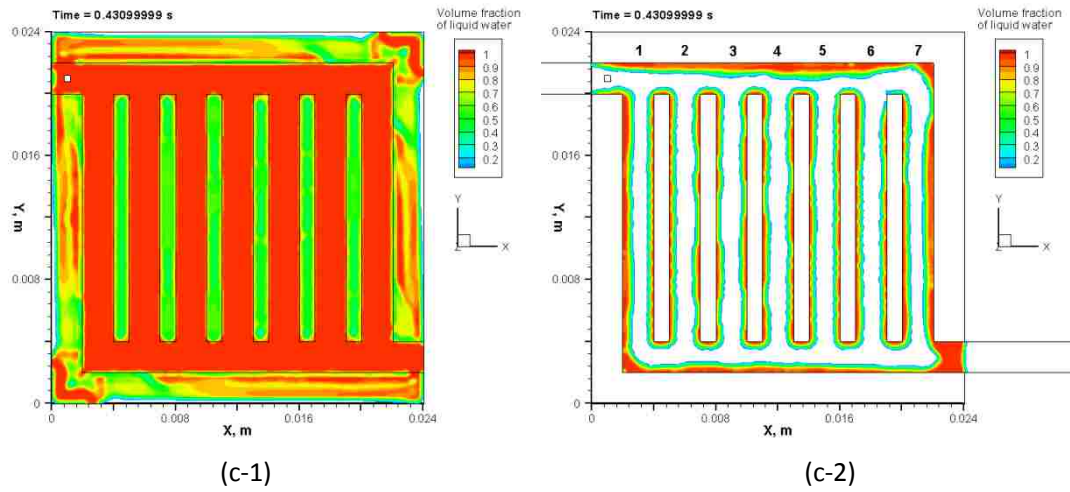


Figure 5-3(a-c) Liquid water distribution near interface in Parallel-SCA model
(Left column: plane at $Z = 0.00029$ m; right column: plane at $Z = 0.0031$ m)

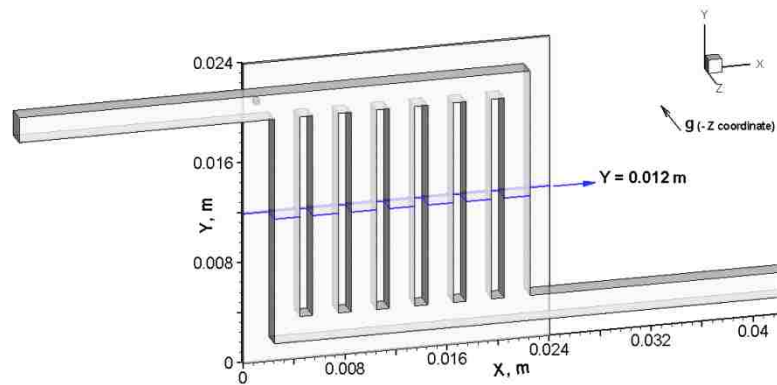
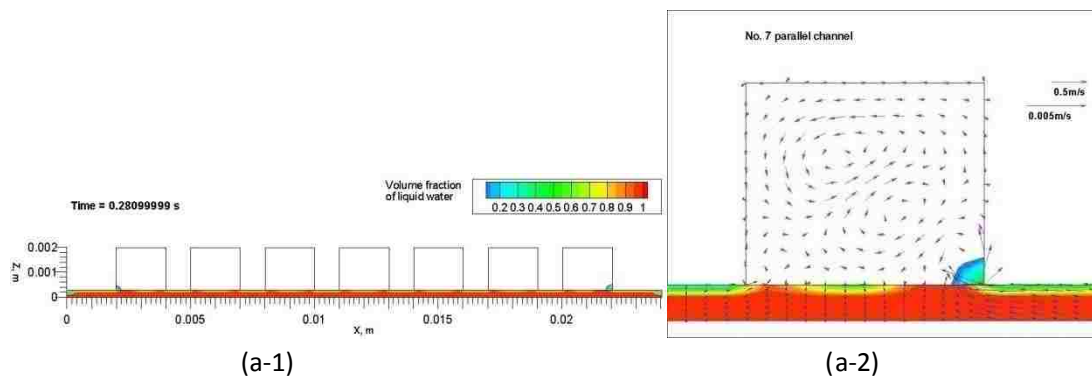


Figure 5-4 Extract a plane from Parallel computational domain at $Y=0.0012$ m



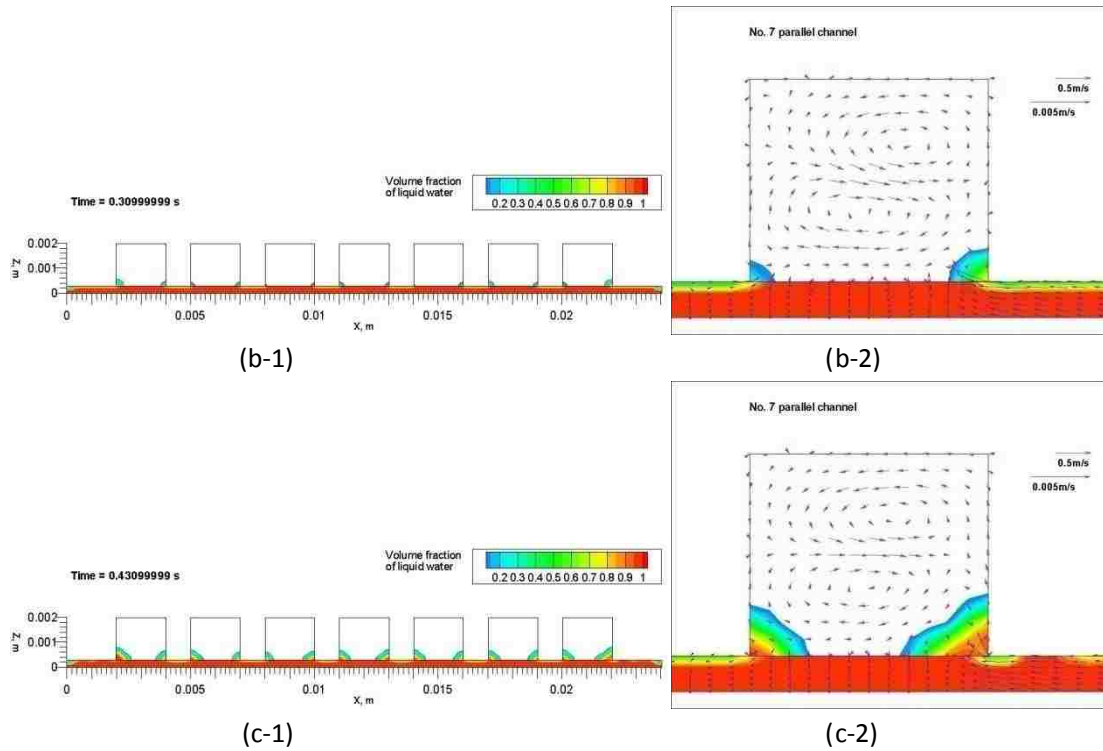


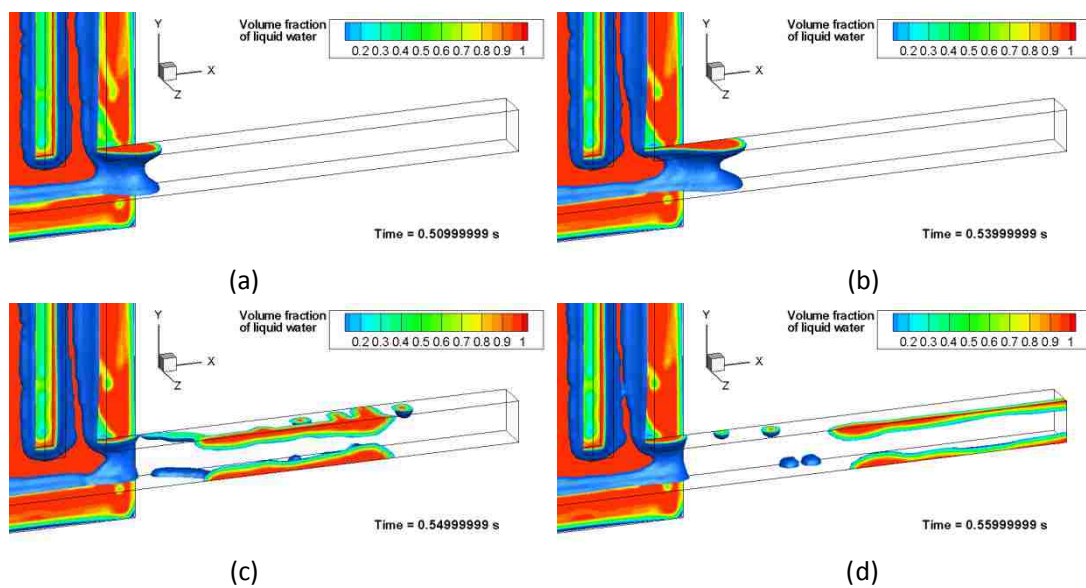
Figure 5-5(a-c) Emerging process on plane at $Y = 0.012$ m in the Parallel-SCA model (Left column: entire plane; right column: enlarged plane with velocity (the upper reference vector is in No. 7 parallel channel, and the lower reference vector is in the porous layer))

5.2.2.2. Dean Vortex Evolution

For the $X-Z$ plane at $Y = 0.012$ m (Figure 5-5), it can be noticed that there are a pair of vortices – an upper vortex and a lower one – in the cross-section of the parallel channels, referred to as Dean vortices, which occurs in curved channels or pipes [49]. This tangential flow enhances the ability of liquid water removal along the primary direction of gas flow channels. Because of the effects of Dean Vortices and gravity, the emerged liquid water occupies the lower corners of the channel cross-section, attaches to the sidewalls due to wall adhesion, and gets removed by the primary gas flow. It can also be noticed that the emergence of liquid water affects the gas flow pattern. Especially in Figure 5-5(a-2), when liquid water first enters into the channel from the right corner in the cross-section, Dean vortices are distorted with approximately 45° in anti-clockwise direction. This interesting phenomenon shows the interaction between gaseous and liquid phases.

5.2.3. Draining Process in Outlet Channel

The draining process in the Parallel-SCA model can be explained by Figure 5-6, showing the deformation of draining liquid water in the outlet channel. The liquid water coming from the porous layer near the peripheral zones of the four frames and the lands gradually develops into two liquid water streams, with the first stream accumulating at the bottom of the outlet manifold and the second stream accumulating on the side wall of No. 7 parallel channel. These two streams meet near the outlet joint and gradually form a valley shape (Figure 5-6(1)). This shape is formed due to the combined effects of wall adhesion and liquid water surface tension. At the same time, the air streams from all directions also meet and merge into one stream at the outlet joint; this combined air stream continuously strikes the windward side of the valley shape, forcing it to move along the outlet channel and be more sharp (Figure 5-6(b)). Then, this valley shaped water deforms into a top-bottom stratified flow pattern while moving along the outlet channel to drain (Figure 5-6(c-h)). Several splashed small droplets are not removed together with the top-bottom stratified flow but adhere to the sidewalls of outlet channel; that is because their inertial force is not strong enough to overcome the friction or wall adhesion. These liquid water removal processes repeat for a period of time, similar deformation occurs for each draining period.



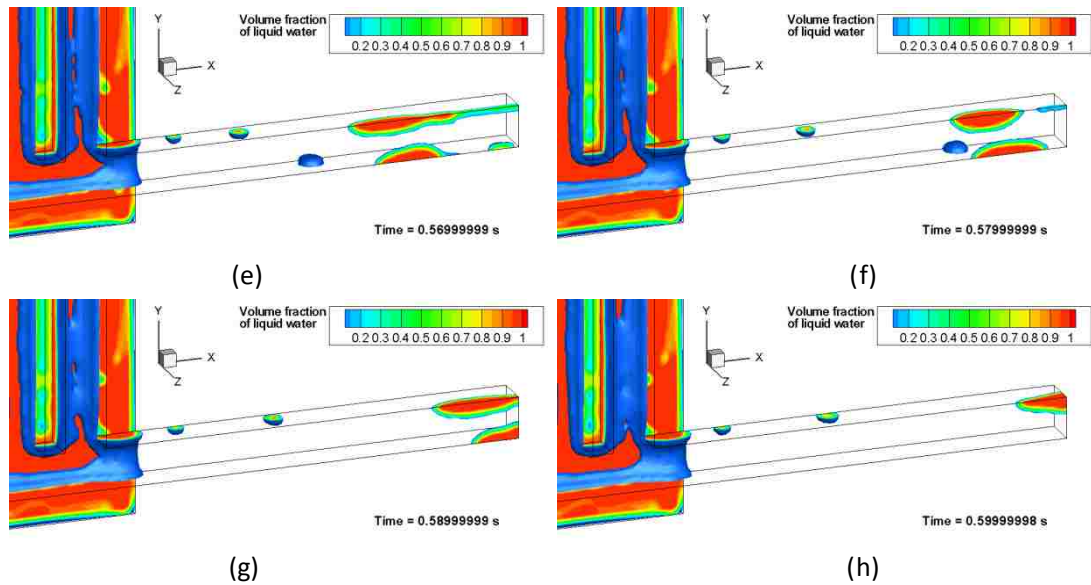


Figure 5-6(a-h) Draining process in the Parallel-SCA model

5.3. Liquid Water Transport in Parallel Model with Dynamic Contact Angle

Unlike Parallel-SCA model, the Parallel-DCA model combines dynamic contact angle (DCA) with the wall boundary conditions through the user defined function (UDF) code. Although the initial contact angles are set the same as that in the Parallel-SCA model, they are affected by the change of local volume fraction of liquid water and velocity. On the other hand, the distribution of liquid water is affected by the change of contact angle. Therefore, the simulation results in the Parallel-DCA model will differ from the results in Parallel-SCA model discussed in the former section.

5.3.1. General Process

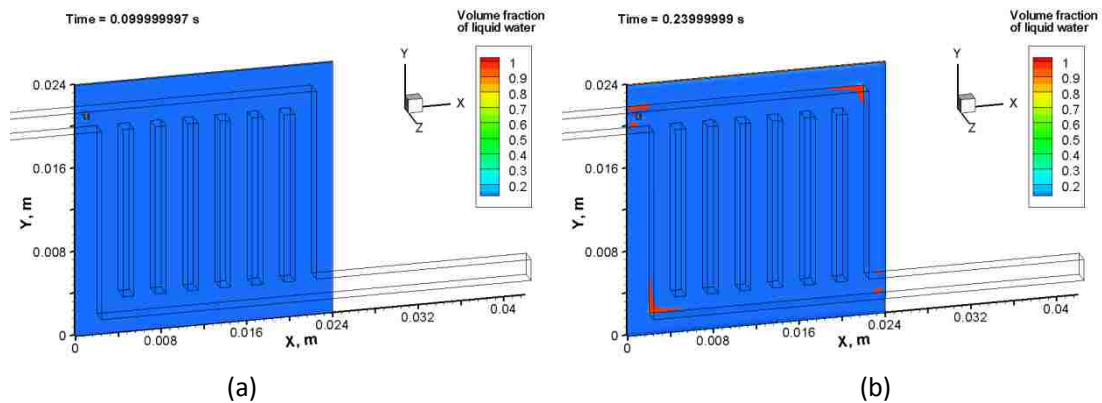
The general process of liquid water transport in the Parallel-DCA model, which is illustrated in Figure 5-7, can also be summarized into several sub-processes:

- (1) Liquid water is supplied from the back surface of the porous layer by a constant mass flowrate to simulate the liquid water generation through electrochemical reaction (Figure 5-7(a)).
- (2) This supplied liquid water mounts up in the porous layer (Figure 5-7(b-d)), and reaches the top surface of porous layer, i.e., the interface between porous layer and channels, first at

four corners of the interface under the channels domain (Figure 5-7(b)), then frame (Figure 5-7(c)), and also the edges of each parallel channels (Figure 5-7(d)).

- (3) Liquid water starts to emerge into the channels, splits into some small droplets flying from No.7 parallel channel and accumulates at the outlet joint and the side wall of the outlet channel (Figure 5-7(e)).
- (4) Liquid water from the porous layer emerges into the gas flow channels first from the interface under the frame of the channels domain, in the middle area of the channels (Figure 5-7(e-f)).
- (5) More liquid water emerges into the channels and accumulates at the outlet joint (Figure 5-7(g)).
- (6) Channels get flooded and the liquid water at the outlet joint starts to move into the outlet channel (Figure 5-7(h)).
- (7) Liquid water drains out through the outlet channel (Figure 5-7(i)). With liquid water increasing, some parts of the gas flow channels get flooded, and the second draining process happens (Figure 5-7(j)).

In summary, the general processes in the Parallel-DCA model are quite similar with that in the Parallel-SCA model, especially the first two sub-processes (Figure 5-2(a-d), 5-7(a-d)); whereas, some phenomena during emerging and draining are different, which are going to be illustrated in the following sections.



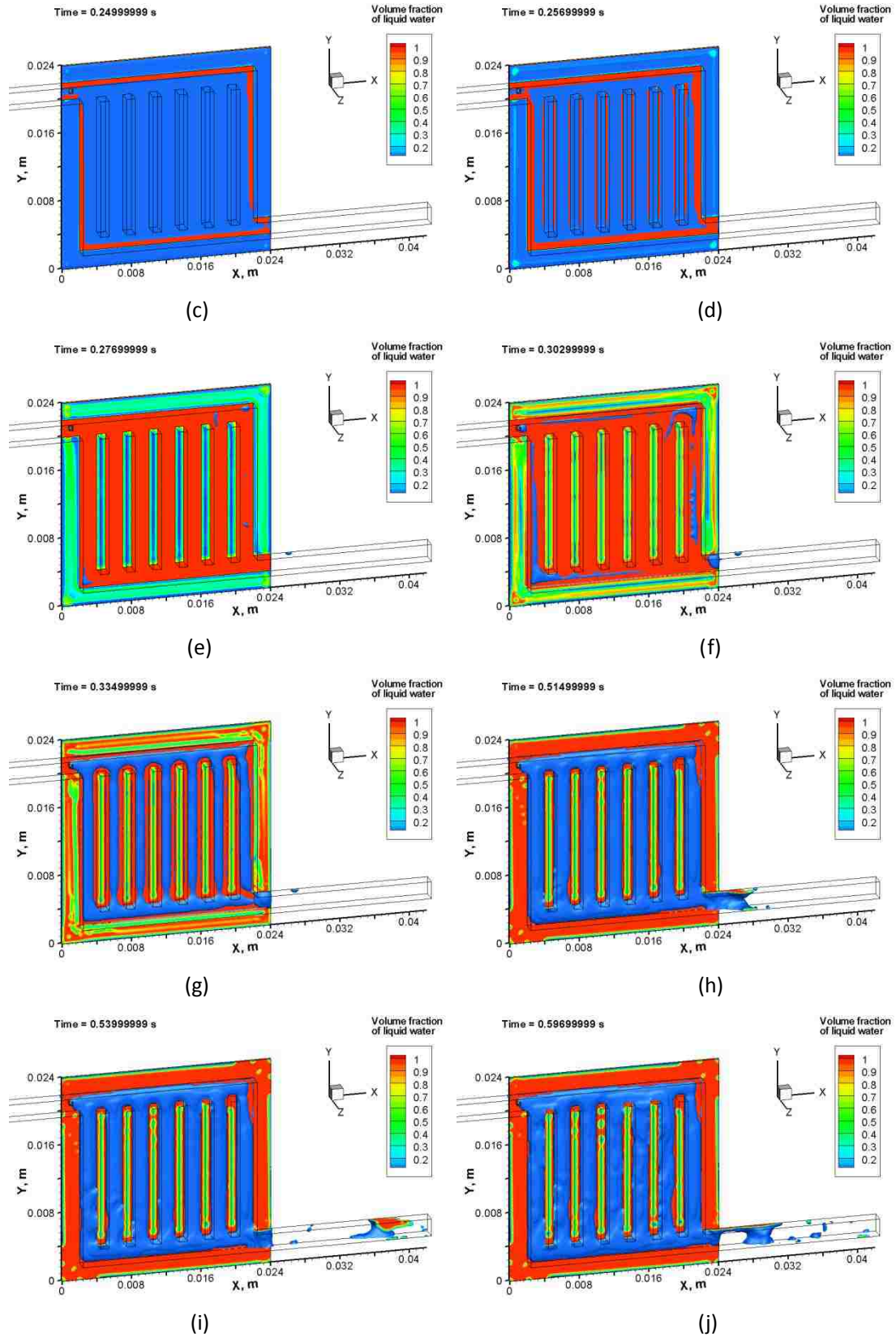


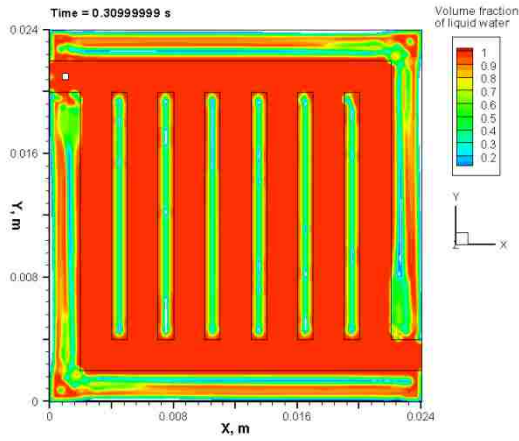
Figure 5-7(a-j) General liquid water transport in the Parallel-DCA model

5.3.2. Emerging Process

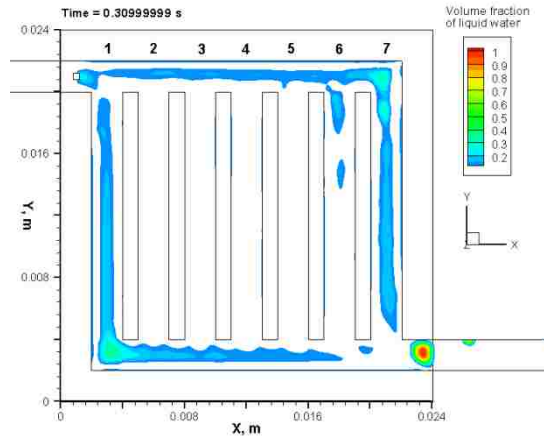
5.3.2.1. Liquid Water Emerging Mainly from Middle of the Interface under Channels

In this Parallel-DCA model, two planes are extracted near interface ($Z = 0.00029$ m and $Z = 0.00031$ m), from the porous layer domain (left column in Figure 5-8) and the channel domain (right column in Figure 5-8). Similarly, liquid water tends to fill in the area underneath the gas flow channels (Figure 5-8(a-1)), and initially emerges into the channels from the interface under peripheral edges of the channel domain (Figure 5-8(a-2)). However, unlike in Parallel-SCA model where liquid water enters into the channels from the edges of the frames and lands, in the Parallel-DCA model, water mainly passes through the interface under the middle of the channels, with only a small amount of liquid water emerging from the edges of lands and moving along sidewalls (Figure 5-8(b-2)). With liquid water continuously generated, i.e. supplied from the liquid inlet boundary, the gas flow channels get partially flooded.

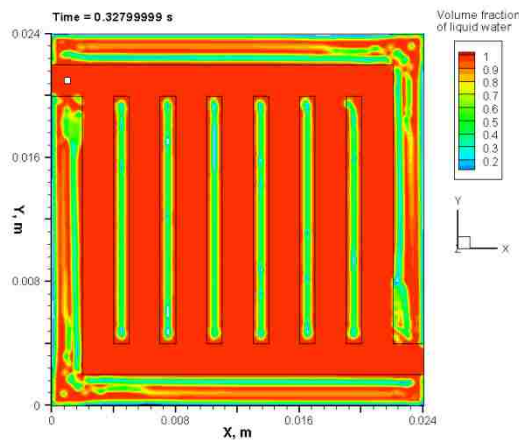
This difference is caused by DCA effects. In order to investigate how DCA affects the emergence pattern of liquid water, two figures are plotted showing the DCA contours filled of porous layer walls (Figure 5-9) and channel sidewalls (Figure 5-10) at certain time instances (0.254 s and 0.337 s) during simulation. The initial contact angle for the porous layer wall boundary is 140° (coloured deep green in DCA contour in Figure 5-9), however, from Figure 5-9, it can be noticed that at the edges of walls under the frames and lands, the DCAs get greater (coloured light green) than 140° . Larger the contact angle is, more strongly the wall repels liquid water. Figure 5-10 shows DCAs at the sidewalls of the channels (or lands). The DCAs on the sidewalls near the interface are greater (coloured light green) than the initial setting 40° (coloured deep green), which means those areas have weak ability to adhere liquid water. Consequently, one key point can be addressed from Figure 5-9 and Figure 5-10, that the areas near the edges of the lands are hard to contain water, and that is why liquid water prefers to enter into the channels from the areas underneath the middle of the gas flow channels in the model with consideration of DCA effects.



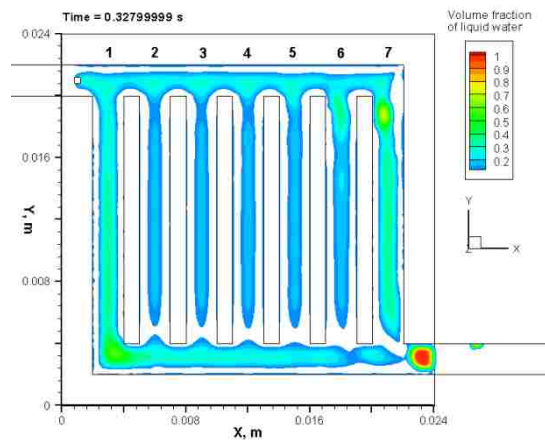
(a-1)



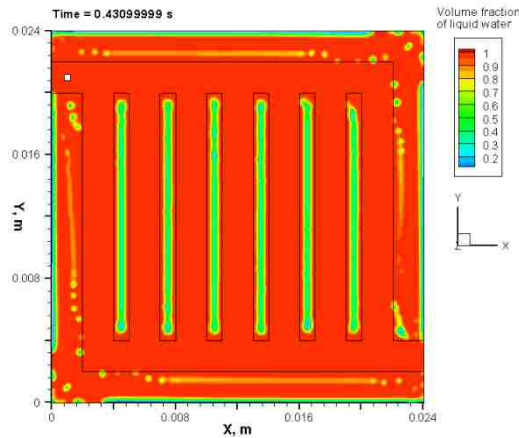
(a-2)



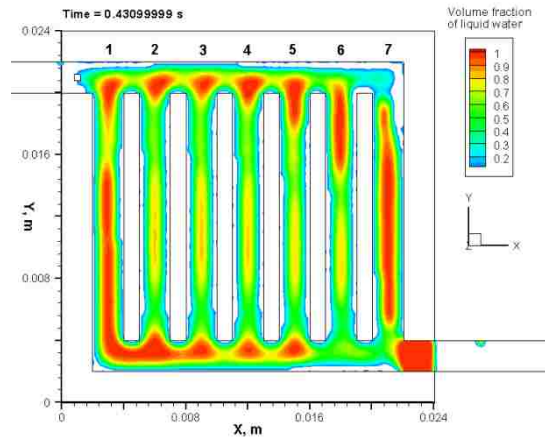
(b-1)



(b-2)



(c-1)



(c-2)

Figure 5-8(a-c) Liquid water distribution near interface in the Parallel-DCA model
(Left column: plane at $Z = 0.00029$ m; right column: plane at $Z = 0.0031$ m)

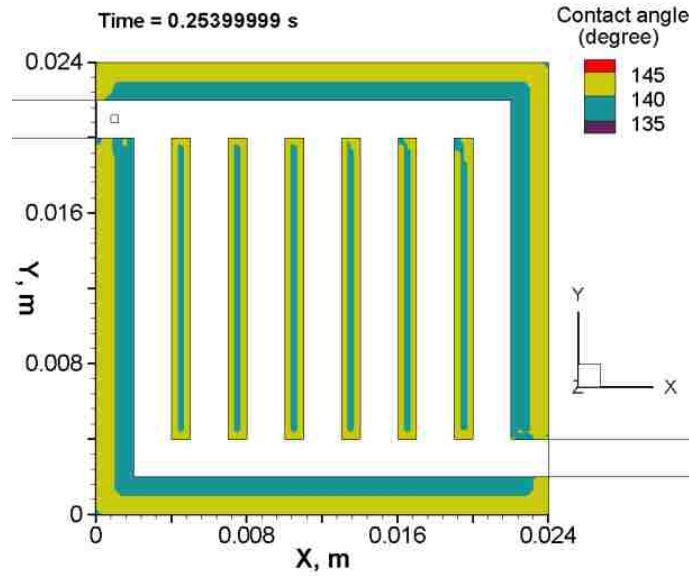


Figure 5- 9 Contact angle on porous layer walls in the Parallel-DCA model at 0.254 s

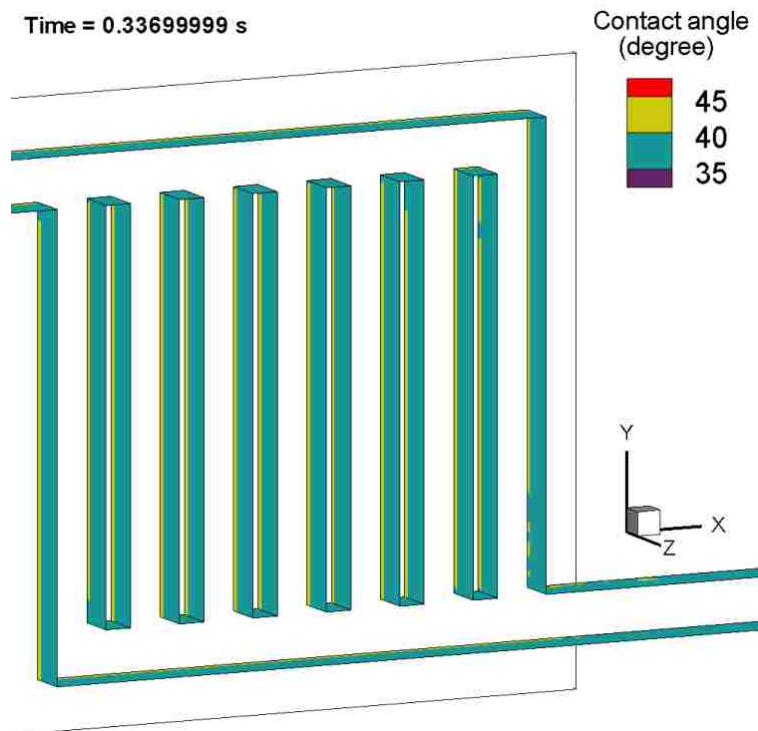


Figure 5-10 Contact angle on channel sidewalls in the Parallel-DCA model at 0.337s

5.3.2.2. Dean Vortex Evolution

There is Dean vortex phenomenon existing in the Parallel-DCA model as well; whereas, the pair of Dean vortices appears in a different pattern (Figure 5-11), with one vortex on the left side and the other on the right side of the channel cross-section, distorted around 90° in anti-clockwise

direction from that in the Parallel-SCA model. Similarly, these Dean vortices are also affected by emerging liquid water, distorting with a certain degree either in clockwise (Figure 5-11(a-2)) or anti-clockwise (Figure 5-11(c-2)) caused by the wave motion of liquid water in the middle bottom of the parallel channel.

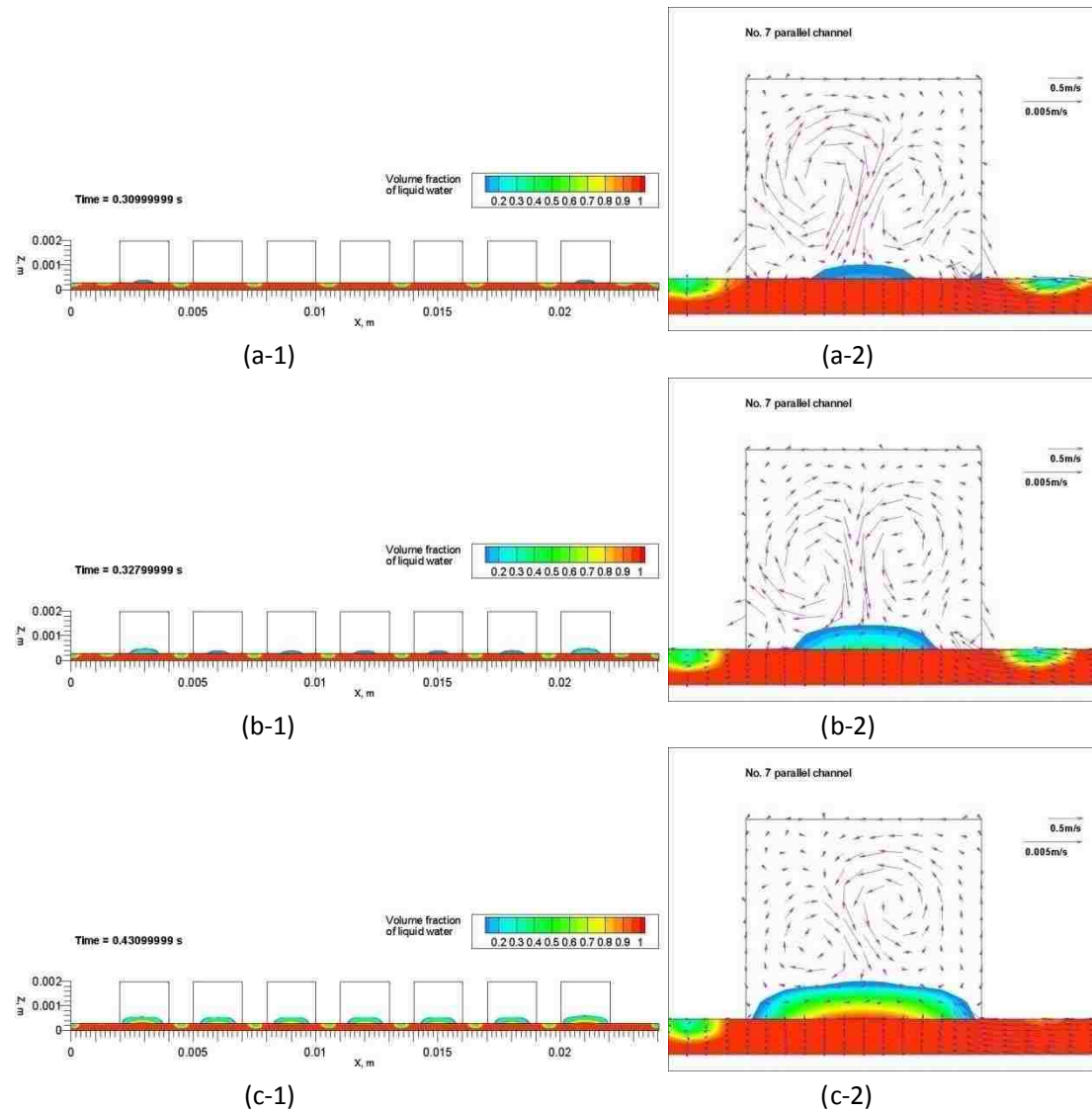
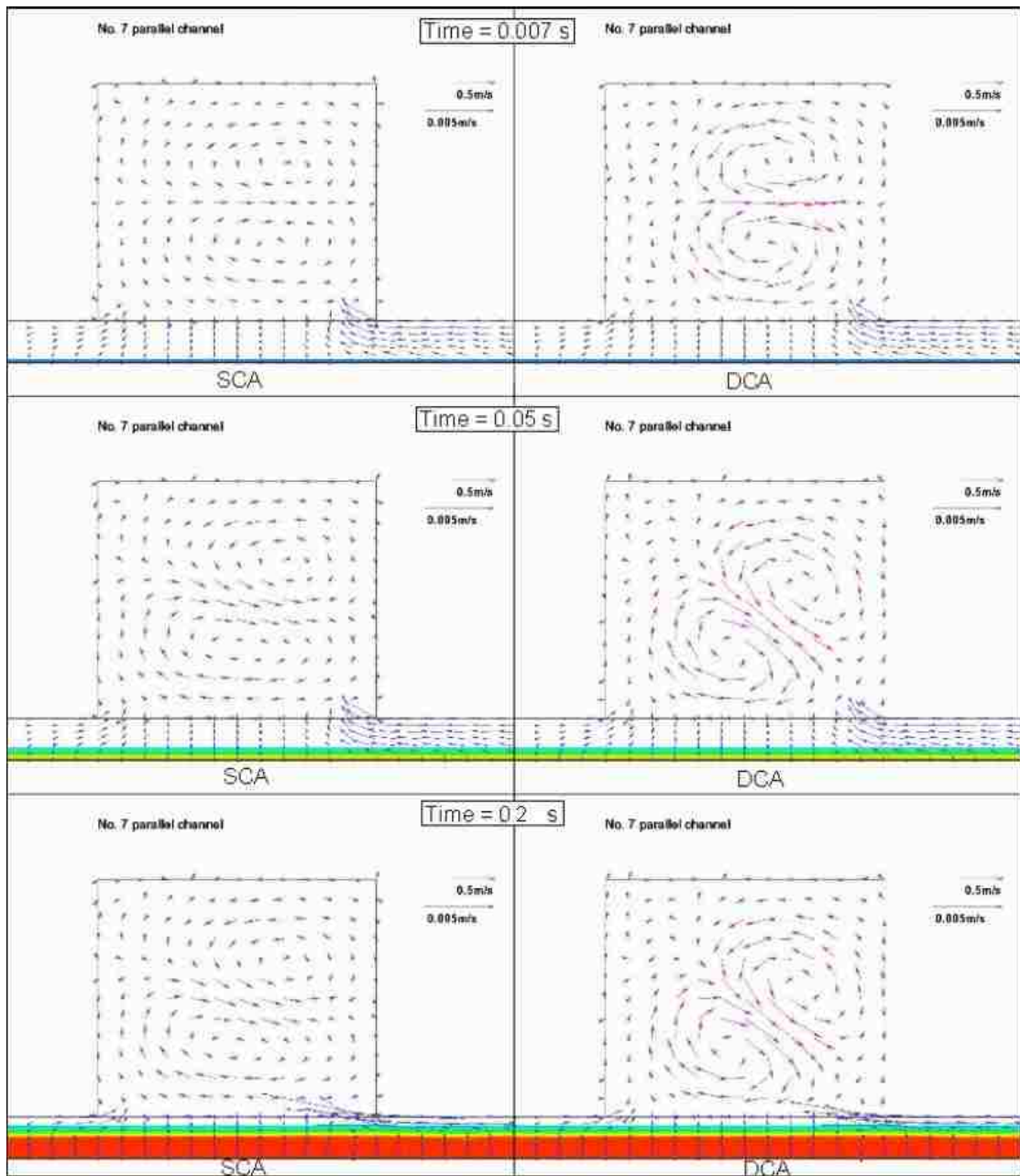


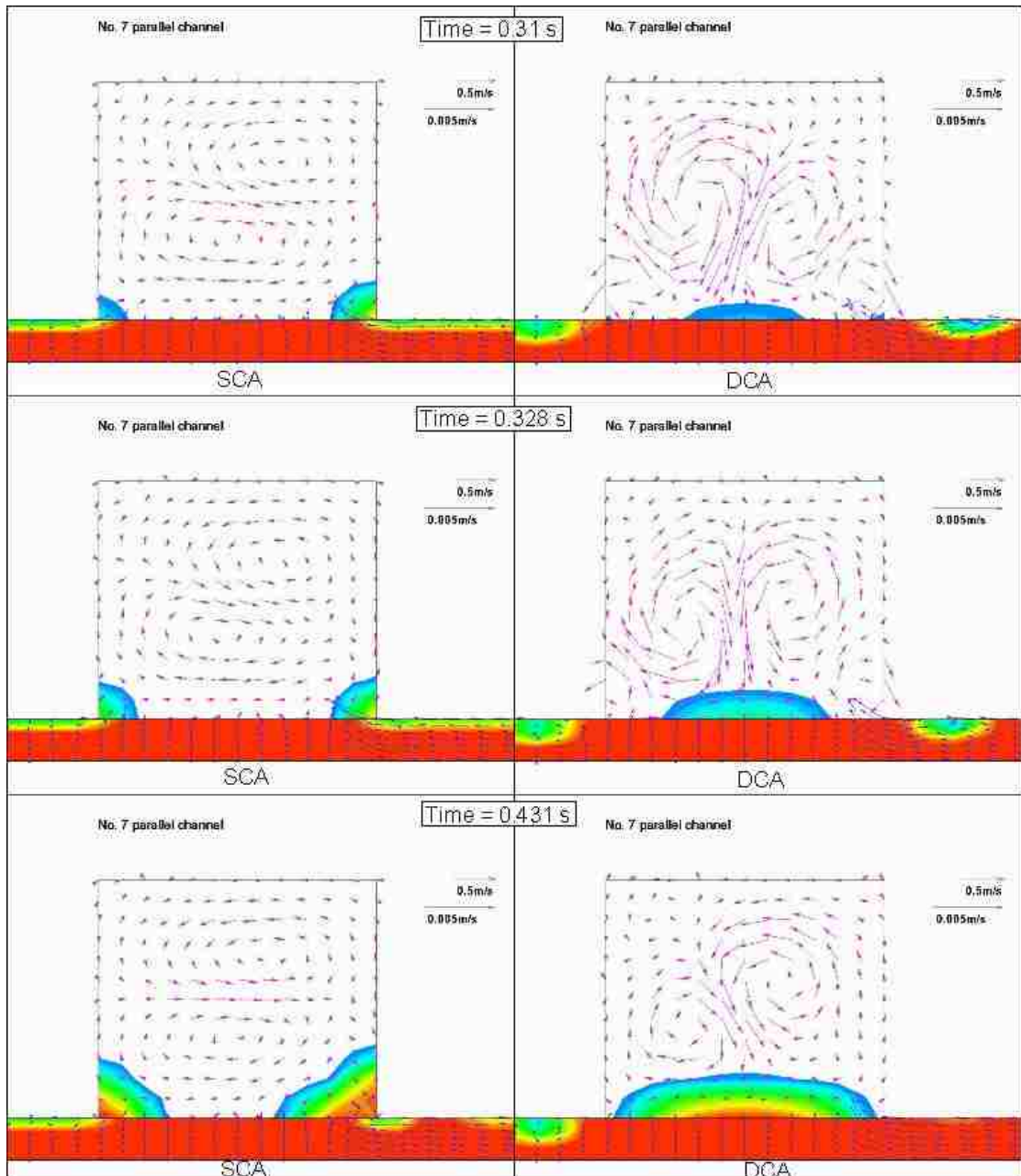
Figure 5-11(a-c) Emerging process on plane at $Y = 0.012$ m in the Parallel-DCA model (Left column: entire plane; right column: enlarged plane with velocity (the upper reference vector is in No. 7 parallel channel, and the lower reference vector is in the porous layer))

In order to compare the detailed difference of Dean vortex evolution between the Parallel-SCA model and Parallel-DCA model, a series of comparison of Dean vortices in the middle plane of No. 7 parallel channel ($Y = 0.012$ m) between the two models is plotted from the beginning of the

simulation (Figure 5-12), in which the left columns are from the Parallel-SCA model and the right columns are from the Parallel-DCA model. From Figure 5-12, it can be noticed that, around 0.007 s, Dean Vortices appear in an upper and lower pattern in both models due to less influence of DCA at the very beginning of the simulation. However, when liquid water is continuously supplied from the liquid inlet boundary and mounts up in the porous layer the velocities near wall, boundaries especially those in porous layer, fluctuate with the volume fraction of liquid water in each computation cell; hence the contact angles change and cause changes in wall adhesion that directly affects the interaction between gas and liquid, and also the distribution of liquid water. That is why the liquid water in the two models emerges from different areas, i.e. edges of the interface under the channels in Parallel-SCA model and middle of the interface under the channels in Parallel-DCA model, as discussed in the previous section. Since velocities vary with the interaction between the two phases, the pattern of Dean vortices in the channel changes along with transform of velocity field in the Parallel-DCA model. While in the Parallel-SCA model, because the contact angle on wall boundaries are fixed, the corresponding wall adhesion is stable, so the velocity field does not change much for the reason of interaction between two-phases, consequently, Dean vortices in the Parallel-SCA model do not distort much with emerging water.



(a)



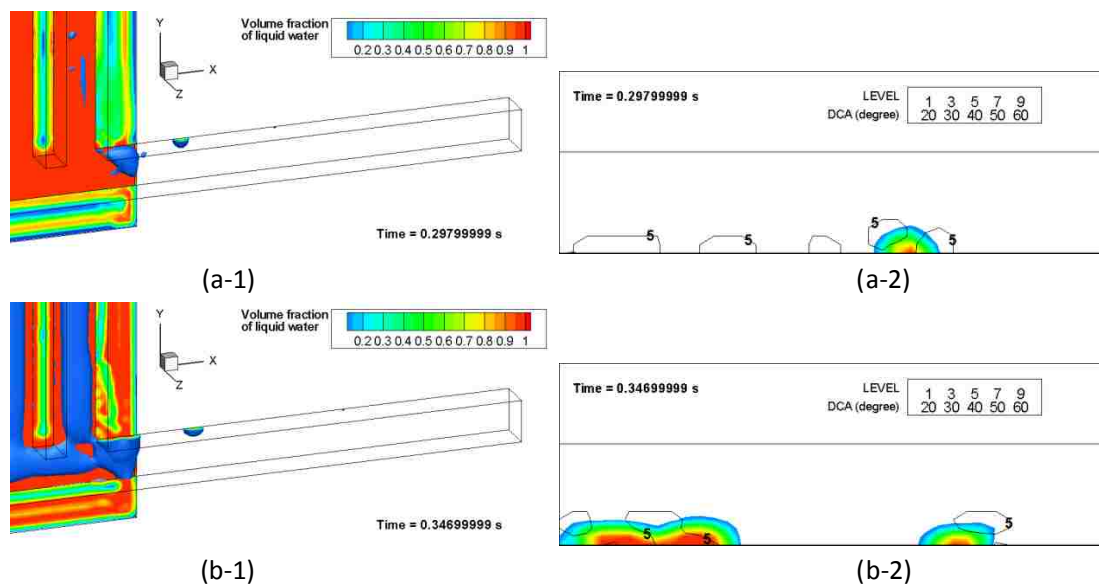
(b)

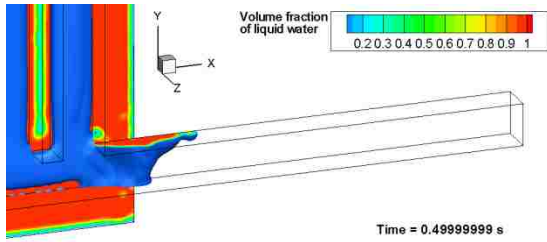
Figure 5-12(a-b) Comparison of Dean Vortex evolution in No.7 parallel channel (Left column: the Parallel-SCA model; right column: the Parallel-DCA model) (The upper reference vector is in No. 7 parallel channel, and the lower reference vector is in the porous layer)

5.3.3. Draining Process in Outlet Channel

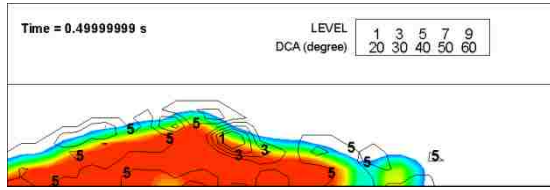
Figure 5-13 illustrates the draining process in the Parallel-DCA model. The left columns in Figure 5-13 show the deformation of draining liquid water in the outlet channel, while the right columns are the upper sidewall (partial) of the outlet channel with colour-flooded contours of volume

fraction of liquid water and line contours of contact angle. When liquid water enters into the gas flow channels, some splashed droplets floating in No. 7 parallel channel attach to the entrance of the outlet channel, and the outlet joint starts to get flooded (Figure 5-7(e), 5-13(a-1)). Soon after, middles of the parallel channels get flooded, while more and more liquid water coming from seven parallel channels and the outlet manifold accumulate at the outlet joint, and tend to move in the outlet channel (Figure 5-13(b-1)-(d-1)). Since the cross-section of the entrance of the outlet channel is partially blocked, gas flow near the windward side of accumulating water gets condensed, hence more pressure acts on the windward surface of liquid water, enhances the momentum and makes it large enough to break restriction of the adhesion between solid and liquid and the viscosity of liquid, and drain into the outlet channel. Like that in the Parallel-SCA model, valley shape forms as well when liquid water starts to drain (Figure 5-13(e-1)). On the other hand, the deformation of liquid water in the outlet channel seems discretional (Figure 5-13(f-1)-(j-1)). Some small splashed droplets adhere to the sidewalls because of large wall adhesion. The removal processes repeat for a period of time. From the right columns of Figure 5-13, it is observed that DCAs are corresponding to the deformation of liquid water, and they shift intensely along the interface between gas and liquid because the velocities change greatly there. Accordingly, the inconstant deformation of draining water is a reflection of DCA effects on liquid water movements.

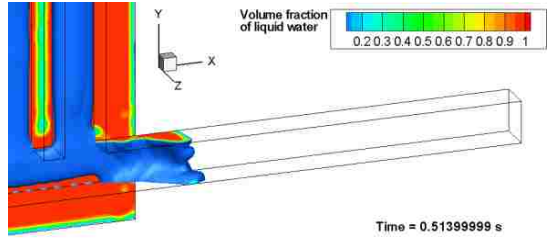




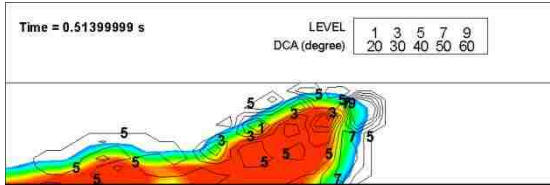
(c-1)



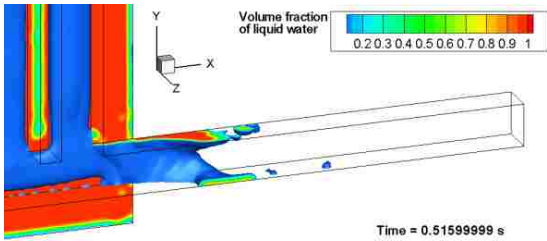
(c-2)



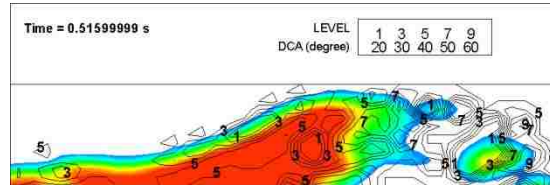
(d-1)



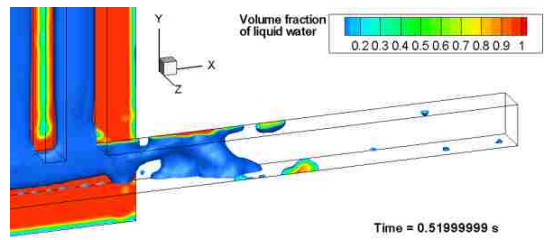
(d-2)



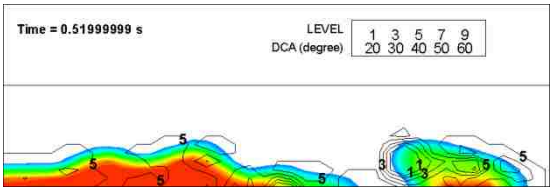
(e-1)



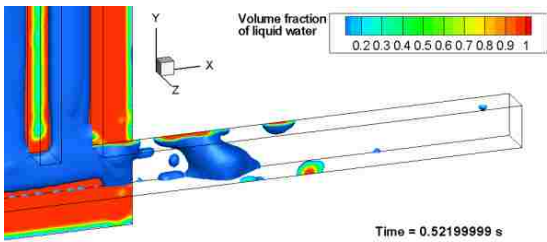
(e-2)



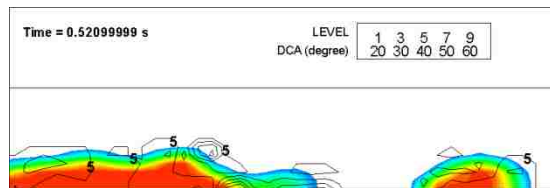
(f-1)



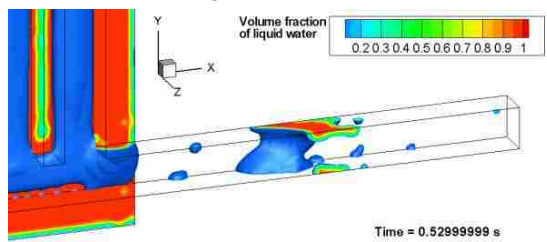
(f-2)



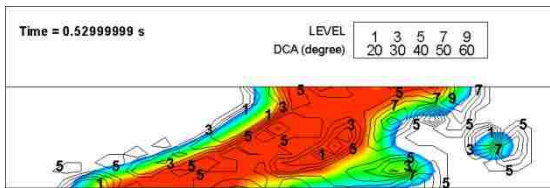
(g-1)



(g-2)



(h-1)



(h-2)

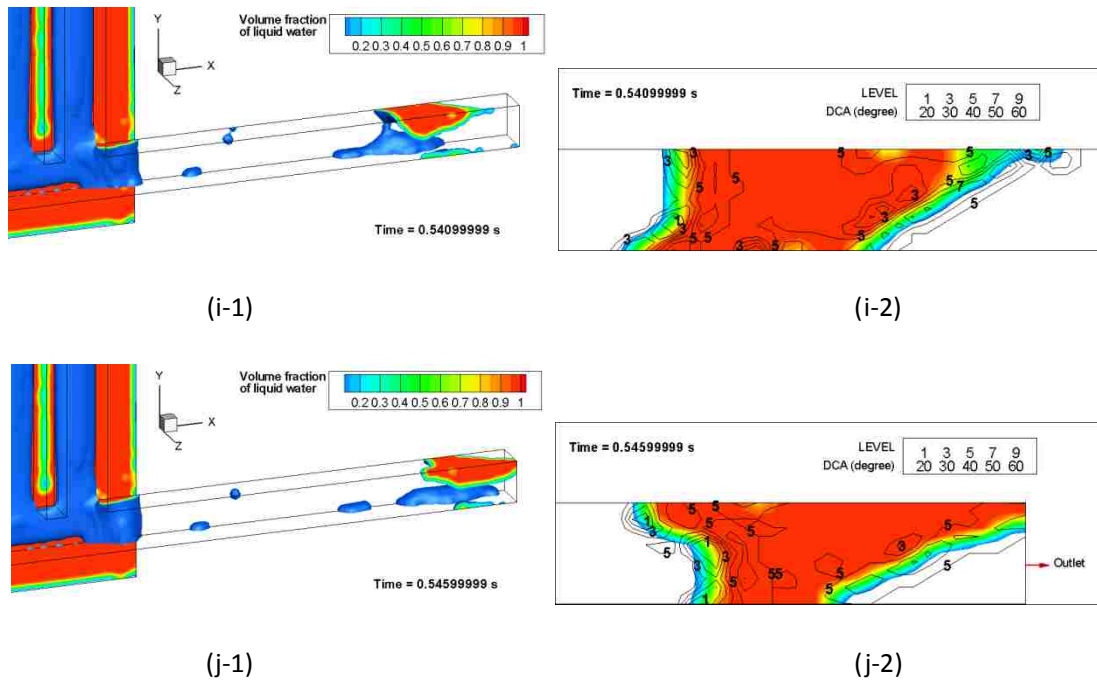


Figure 5-13(a-j) Draining water deformation in Parallel-DCA model
 (Left column: liquid water draining in outlet channel; right column: dynamic contact angles on top sidewall(partial) of outlet channel)

5.3.4. Liquid Water Amount and Pressure over Time

Figure 5-14 is a plot of liquid water amount (kg) with time in the channels and porous layer in the Parallel-DCA model; while Figure 5-15 presents the average gauge pressure (Pa) at the inlet and outlet surfaces of the gas flow channels over time.

From Figure 5-14, it can be noticed that, at the forefront, liquid water only moves in the porous layer and mounts up at the speed with a steady slope (Speed 1). When there is liquid water entering into the gas flow channels, approximately 0.27 s, the slope (Speed 2) of liquid water amount in the porous layer has a dramatically decrease, while the liquid water in the channels increases at a speed (Speed 3) higher than Speed 2 but lower than Speed 1. Around 0.55 s and 0.62 s, there are two slight fluctuations of the liquid water amount in the channels caused by the draining.

As shown in Figure 5-15 which shares the same time directions with Figure 5-14, outlet gauge pressure stays at zero since the reference pressure is held at 1 atm at the middle of the outlet

boundary. Before 0.45 s, the inlet pressure remains around 100 Pa; however, after that the inlet pressure starts to tempestuously fluctuate. That is because, in the draining process, with more and more water accumulating at the outlet joint, partially block the channel and baffle the gas flow, and make inlet pressure rise up; when the accumulated water cannot be held and drain out though the outlet channel, the inlet pressure falls down correspondingly.

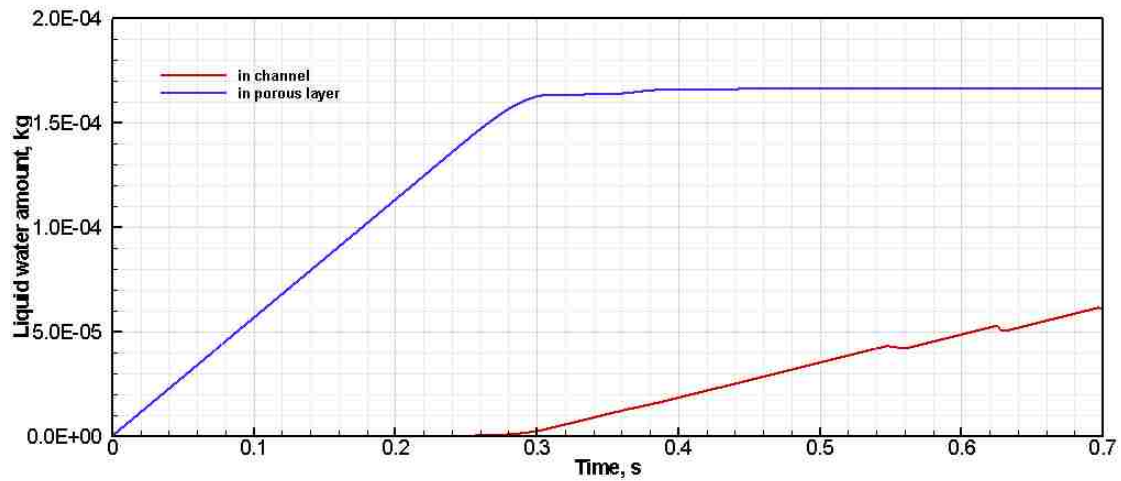


Figure 5-14 Liquid water amount in the Parallel-DCA model over time

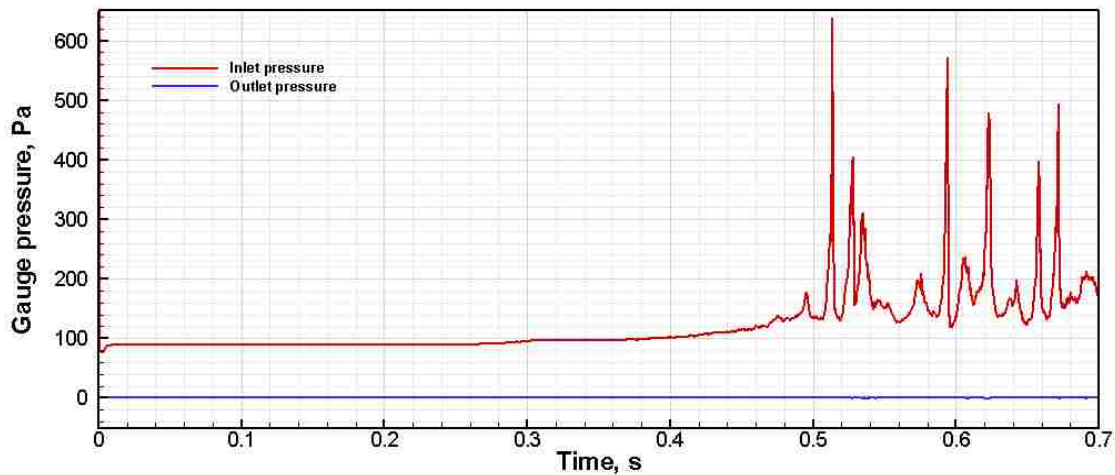


Figure 5-15 Gauge pressure in the Parallel-DCA model over time

5.4. Comparison and Summary

From Figure 5-16, which shows the liquid water and velocity distribution on three planes extracted at $Y = 0.006 \text{ m}$, 0.012 m , and 0.018 m (the left columns are from the Parallel-SCA model and the right columns are from the Parallel-DCA model), it can be observed that maldistribution

of gas flow exists in both models, which is caused by parallel flow field design itself, and does not change much over time.

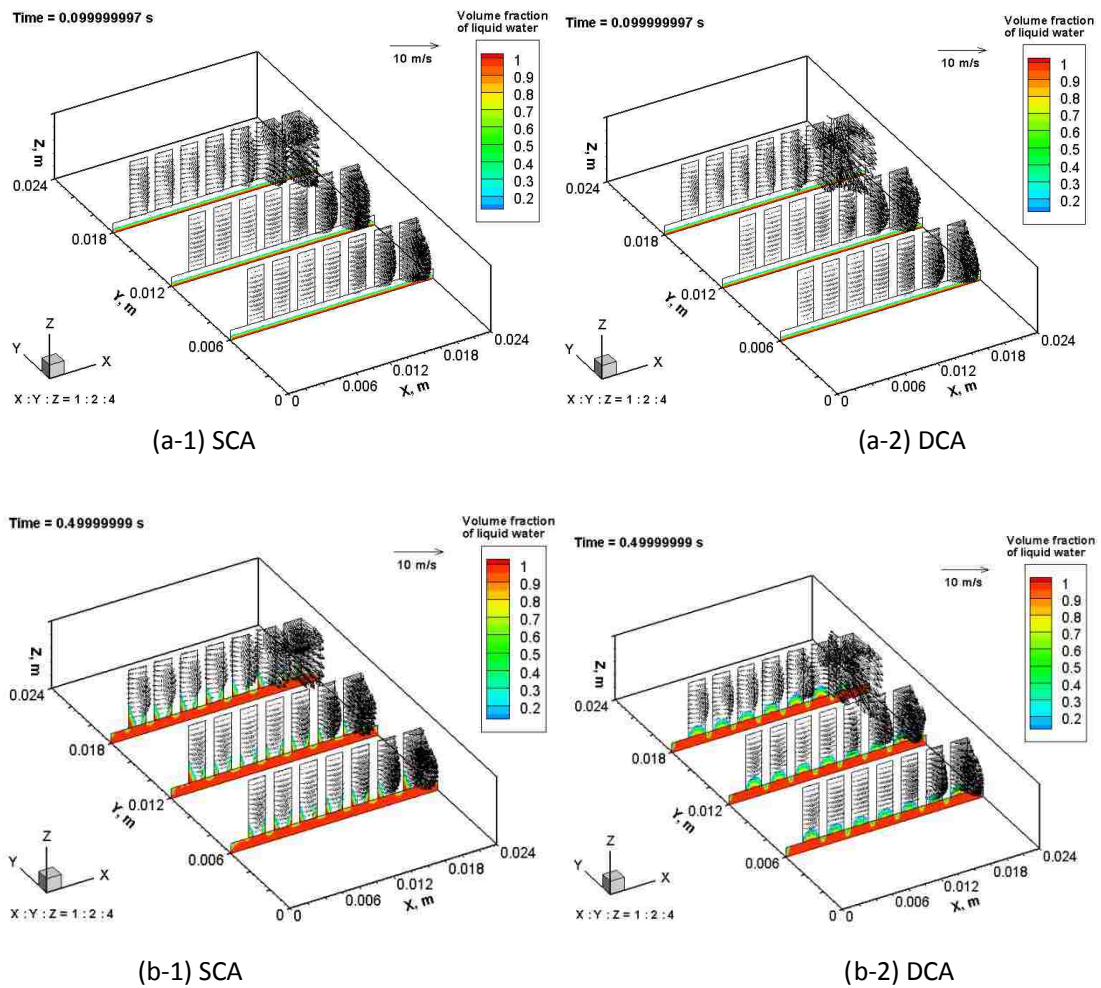


Figure 5-16(a-b) Liquid water and velocity distribution on three planes ($Y = 0.006$ m, 0.012 m, and 0.018 m) at 0.1 s, 0.5 s

Compare gas and liquid water phenomena in the two parallel models, i.e. the Parallel-SCA model and the Parallel-DCA model, although the general processes are quite similar, there are some differences in detailed phenomena which cannot be eliminated, such as emerging pattern (SCA model: liquid water firstly emerges from the edges of the interface under the channels; DCA model: liquid water firstly emerges from the middle of the interface under the channels), Dean vortices evolution (SCA model: upper-lower distribution; DCA model: from upper-lower to left-right distribution), and draining deformation (SCA mode: top-bottom stratified flow; DCA model: inconstant flow). Consequently, it is necessary to consider the DCA effects when investing water management in the model of PEMFC with parallel flow field design.

6. GAS-LIQUID PHENOMENA IN PROTON EXCHANGE MEMBRANE FUEL CELLS WITH STIRRED TANK REACTOR (STR) DESIGN

6.1. Numerical Model Setup

A novel PEMFC was developed by Benziger et al. [44] and Hogarth and Benziger [45], which has a stirred tank reactor (STR) instead of conventional gas flow channels. There is no publication so far investigating the gas-liquid phenomena within the cathode of this type of PEMFC. In order to get fundamental understanding of liquid water transport in the cathode of STR PEMFC, a numerical model of the cathode is generated including a porous layer and a STR. Similar to the parallel model, for the STR model, two cases, i.e., the STR-SCA model and the STR-DCA model, sharing the same computational domain and operating conditions other than wall boundaries, are carried out for the consideration of the DCA effects.

6.1.1. Computational Domain

The numerical simulation domain (Figure 6-1) is a STR PEMFC cathode, sharing the similar geometry dimensions in Hogarth and Benziger's model [45], constituted by a porous layer and a stirred tank reactor attached to it rather than conventional gas flow channels.

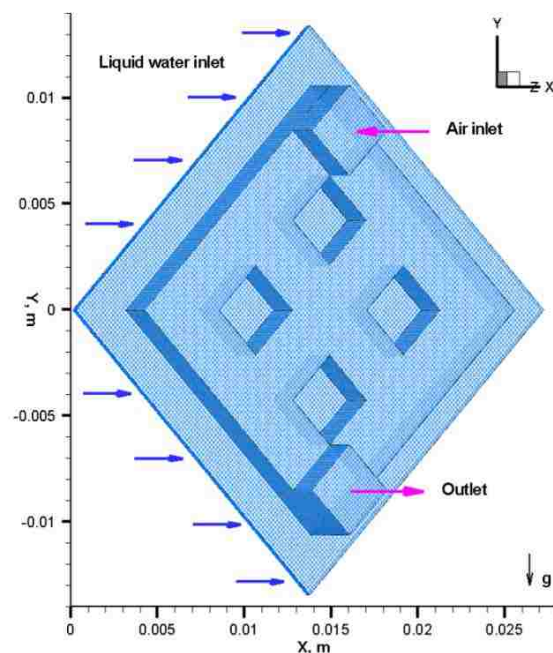


Figure 6-1 Computational domain of STR model

The porous layer is 0.019 m (in X-direction) \times 0.019 m (in Y-direction) \times 0.0003 m (in Z-direction). The attached STR is 0.015 m (in X-direction) \times 0.015 m (in Y-direction) \times 0.0017 m (in Z-direction), is an open rectangular plenum as gas flow field, subtracting four distributed pillars with intervals of 0.003 m in X-Y plan. These pillars are in a dimension of 0.003 m (in X-direction) \times 0.003 m (in Y direction) \times 0.0017 m (in Z-direction) for each. A gas inlet channel and an outlet channel with the same dimensions of pillars, are attached to the STR, distributed on the diagonal corners. The gravity is applied along the diagonal of the plenum connecting gas inlet and outlet channels, directed to the outlet. And the porosity for the porous layer is 0.3.

6.1.2. Boundary Conditions

The boundary conditions introducing the initial parameters into the STR model are defined as shown in Table 6-1, which are gained according to the given parameters in Hogarth and Benziger’s work [45] and the validation work of VOF model by Le et al. [33]. Similar to the parallel model, in the STR-SCA model, initial contact angles for wall boundaries are fixed as constant, and in the STR-DCA model, contact angles change with the change of flow field during simulation by means of the UDF code compiling on the wall boundary conditions. In the STR-DCA model, at a certain time, for each computational cell there is a corresponding contact angle value.

Table 6-1 Boundary conditions of the STR model

| Boundaries | | Type | Descriptions |
|--|--|-----------------|--|
| Liquid inlet (Back surface of porous layer) | | Mass flow inlet | Mass flowrate: $1.331 \times 10^{-4} \text{ kgs}^{-1}$ |
| Gas inlet | | Mass flow inlet | Mass flowrate: $6.615 \times 10^{-5} \text{ kgs}^{-1}$ |
| Outlet | | Pressure outlet | Pressure: 1 atm |
| Walls | Side walls of plenum including inlet and outlet channels | Wall | No-slip, initial contact angle: 53° |
| | Upper walls of plenum | Wall | No-slip, initial contact angle: 43° |
| | Walls of porous layer (walls under frames and pillars) | Wall | No-slip, initial contact angle: 130° |

6.1.3. Grid Independency

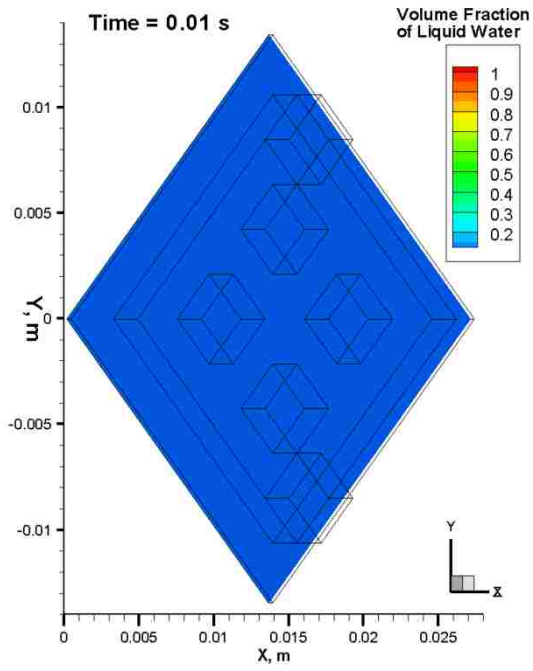
The computational domain of STR model is meshed into 167,400 cells with a total volume of $4.602 \times 10^{-7} \text{ m}^3$, and a maximum volume of $3.935185 \times 10^{-12} \text{ m}^3$ and a minimum volume of $1.388889 \times 10^{-12} \text{ m}^3$ for each cell. The cell size measures approximately $1.67 \times 10^{-4} \text{ m}$ by $1.67 \times 10^{-4} \text{ m}$ in X- and Y- directions, whereas the dimensions in Z-direction are $1.4 \times 10^{-4} \text{ m}$ in the plenum domain and $5 \times 10^{-5} \text{ m}$ in the porous layer domain. Grid independency for this STR model is determined by the same method in the parallel model, which was implied by increasing and decreasing certain percentages of grid cells [33].

6.2. Liquid Water Transport in STR Model without Dynamic Contact Angle

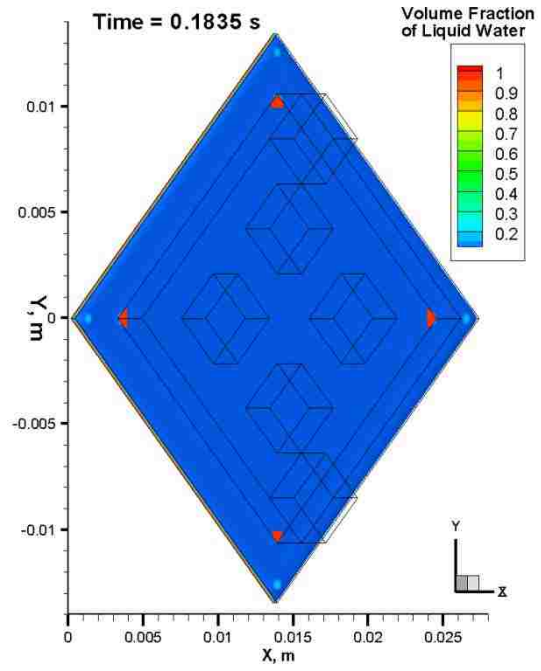
6.2.1. General Process

Figure 6-2 shows the general process of liquid water transport over time at several selected time instants, which can be divided into the following sub-processes:

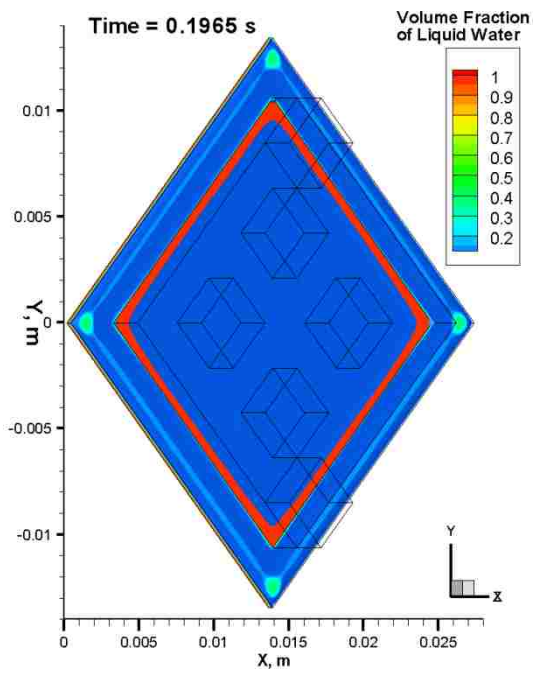
- (1) The liquid water generated from the electrochemical reaction is supplied continuously from the liquid inlet boundary, i.e. the back surface of the porous layer (Figure 6-2(a)).
- (2) Liquid water rising up in the porous layer, reaches the interface between the porous layer and the plenum, firstly at four corners (Figure 6-2(b)), and peripheral edges of the plenum domain (Figure 6-2(c)), then the edges of four pillars (Figure 6-2(d)).
- (3) Liquid water goes through interface and emerges along sidewalls of the plenum domain (Figure 6-2(e)), and also sidewalls of each pillar (Figure 6-2(f)). Some liquid water merges from circumjacent areas near pillars as well (Figure 6-2(g)).
- (4) Liquid water emerging from peripheral edges of the plenum domain, and those from the edges of the pillars, merge together with the liquid water from the circumjacent areas near pillars, forming “tooth shape” (Figure 6-2(h)).
- (5) With more and more water enters into the plenum, the areas under pillars get flooded. By the cooperation of gravity and gas flow, liquid water drains out of the computational domain through the outlet channel (Figure 6-2(i, j)).



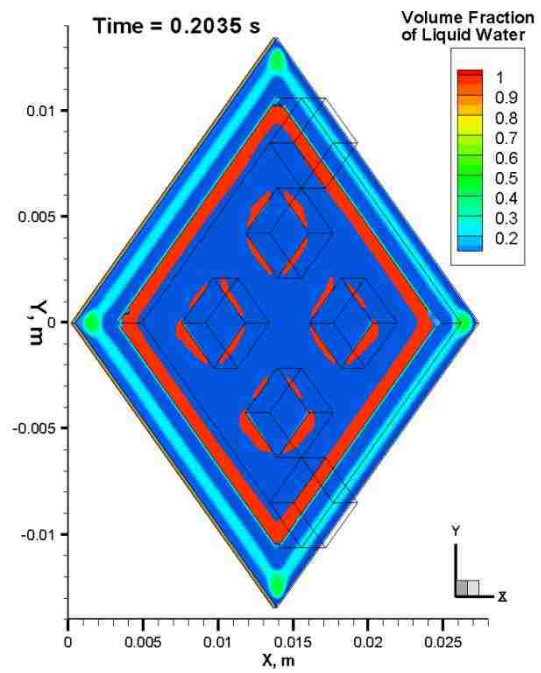
(a)



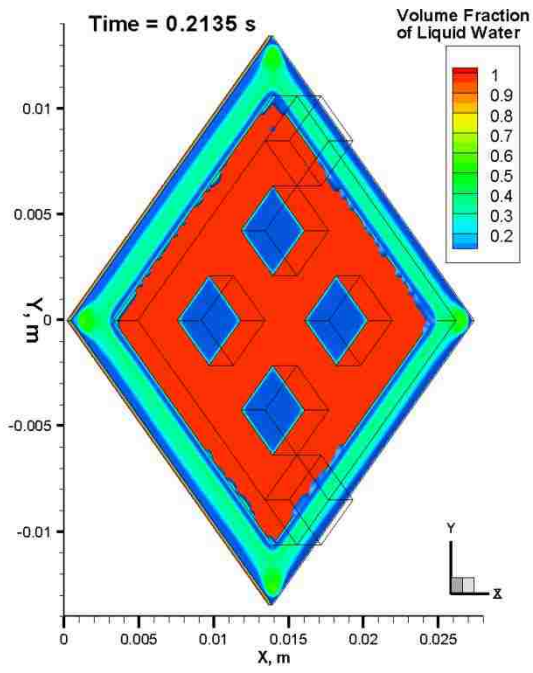
(b)



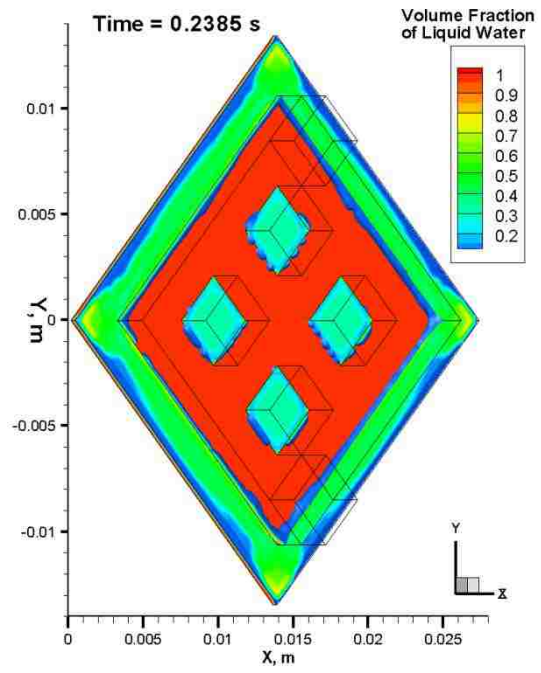
(c)



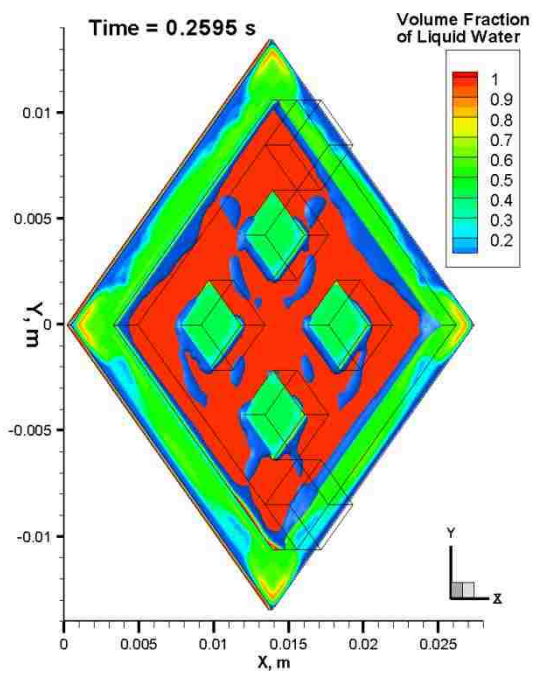
(d)



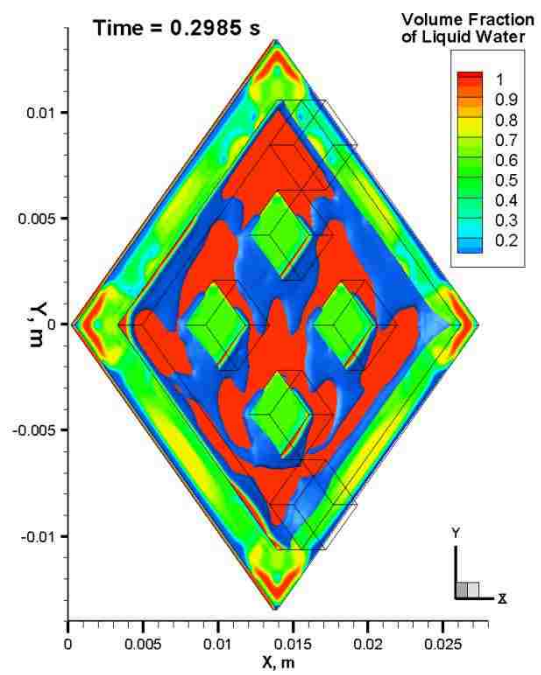
(e)



(f)



(g)



(h)

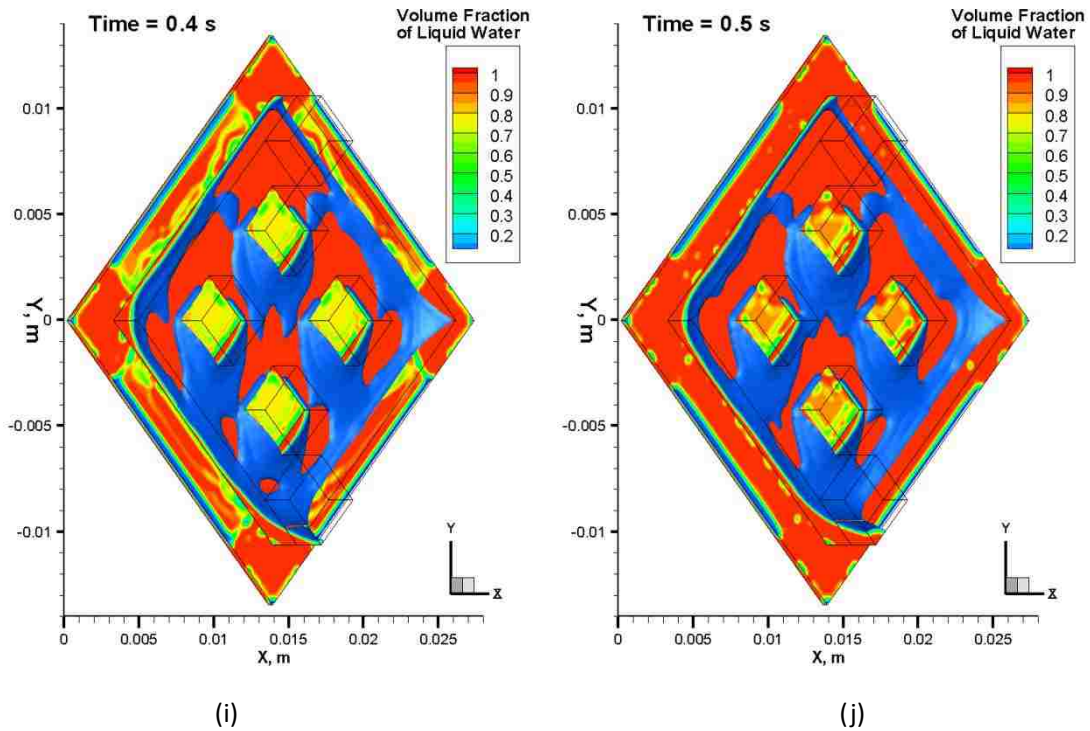


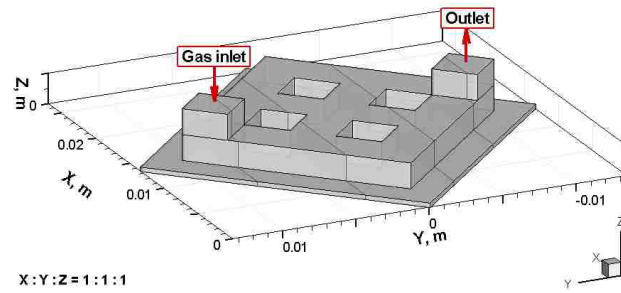
Figure 6-2(a-j) General liquid water transport in the STR-SCA model

6.2.2. Emerging Process

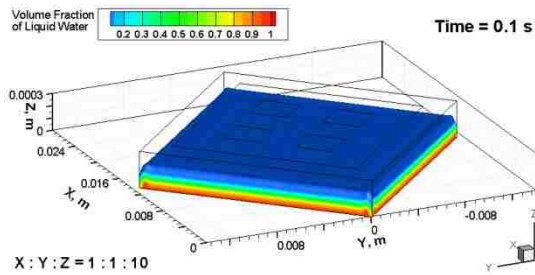
6.2.2.1. Liquid Water Emerging Tranquilly in Porous Layer

For the sake of investigating liquid water transport in the porous layer, a series of three-dimensional plots are presented in the left columns in Figure 6-3 with coloured liquid water volume fraction contours only in the porous layer (positioned as shown in Figure 6-3(a)) and a tenfold enlarged scale in Z-direction. The right columns in Figure 6-3 show the liquid water distribution on four planes extracted from the porous layer domain at $Y = -0.008$ m, -0.003 m, 0.003 m, and 0.008 m, with the same scheme and time instance as those in the left columns.

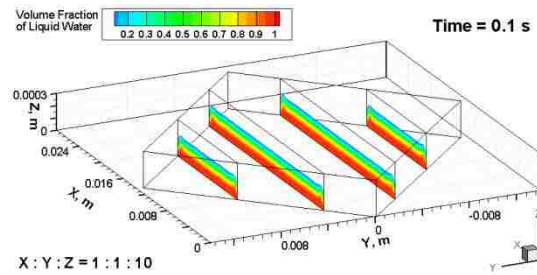
As denoted by Figure 6-3(b-f), liquid water in the porous layer rises up in a relative equably state. And the water near the sidewall of porous layer is repulsed because of the hydrophobic wettability on the walls of the porous layer which have a static contact angle of 130° . That is also why the volume fractions of water under the frame and pillars are lower than that under the plenum (Figure 6-3(e-1, e-2)). With more and more liquid water generated, most part in the porous layer domain fills with water, and almost the entire interface between the porous layer and the plenum gets wet, as shown in Figure 6-3(f-1, f-2).



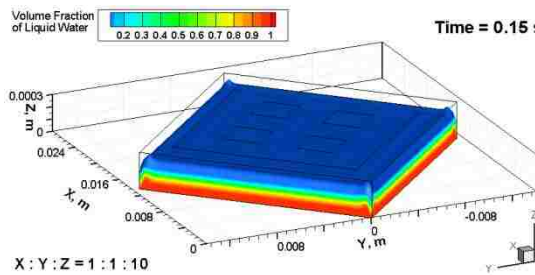
(a)



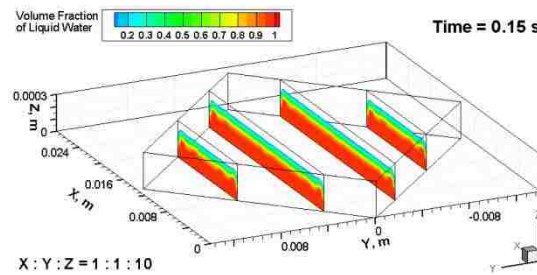
(b-1)



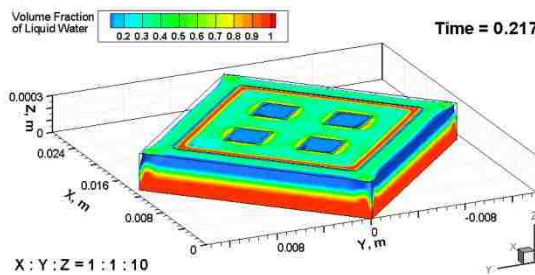
(b-2)



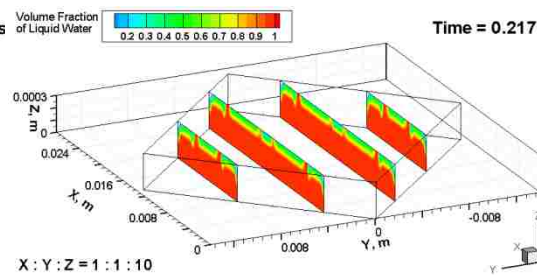
(c-1)



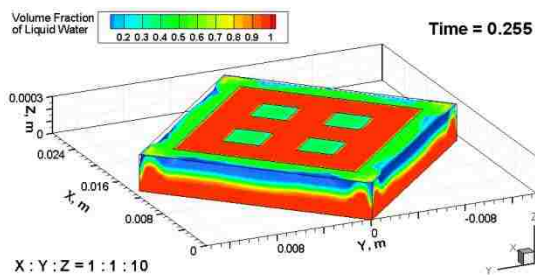
(c-2)



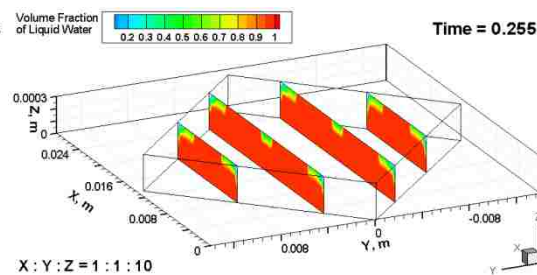
(d-1)



(d-2)



(e-1)



(e-2)

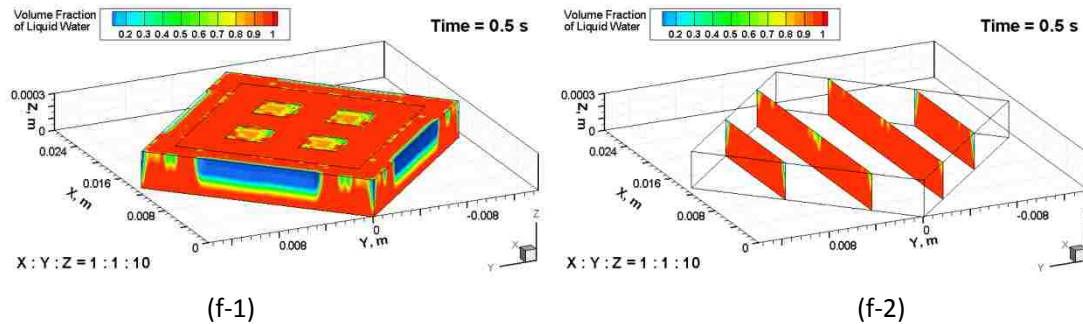


Figure 6-3(a-f) Liquid water transport in porous layer in the STR-SCA model
 (a) Numerical domain; (b-f) left column: porous layer domain; right column: four planes extracted at $Y = -0.008 \text{ m}, -0.003 \text{ m}, 0.003 \text{ m},$ and 0.008 m

6.2.2.2. Liquid Water Distribution in Plenum

Figure 6-4 shows the liquid water distribution on the X-Y plane (with the edges of porous layer showed up) extracted from the plenum domain at $Z = 0.00031 \text{ m}$, where is very close to the interface. In the first instance, liquid water emerges from the peripheral edges of the plenum domain (Figure 6-4(a)), and the edges of pillars (Figure 6-4(b)), especially the bottom edges. Then water come out from the circumjacent areas near bottom of four pillars and also the upper side of the top pillar (Figure 6-4(c)), and gradually merge with the water from edges of plenum (Figure 6-4(d)), forming tooth like shapes (Figure 6-4(e)). Finally, nether areas near pillars get flooded, as well as the areas near peripheral edges of plenum (Figure 6-4(f)). The phenomenon that liquid water distributes mainly in the nether part of plenum as shown in Figure 6-4, is affected by gravity direction and location of the inlet channel and the outlet channel.

Comparing with two sub-figures in Figure 6-5, which show the pressure contours with velocity vectors on the plane at selected time instances as the same in Figure 6-4(a, b), it can be noticed that gas flow velocities at 0.245 s (Figure 6-5(a)) are larger than that at 0.255 s (Figure 6-5(b)), because the water emerging from the porous layer into the plenum embarrasses the gas flow and decreases the velocity. The velocities at lower peripheral edges of plenum are pointed from the plenum of the sidewalls, therefore the liquid water there adhere to the sidewalls of the plenum and flow along the edges (Figure 6-5(b)). Similar situations happen near the edges of the pillars. Relating the liquid distribution in Figure 6-4(c, d) with the pressure distribution in Figure 6-5(a, b), it is addressed that where liquid water accumulates have lower pressure than surrounding areas, because the velocities of gas flow are pointed from higher pressure areas to the lower ones, and

liquid water moves along with the gas flow and accumulated. In the STR-SCA model, the pressure at the lee side of pillars is lower where easily get flooded.

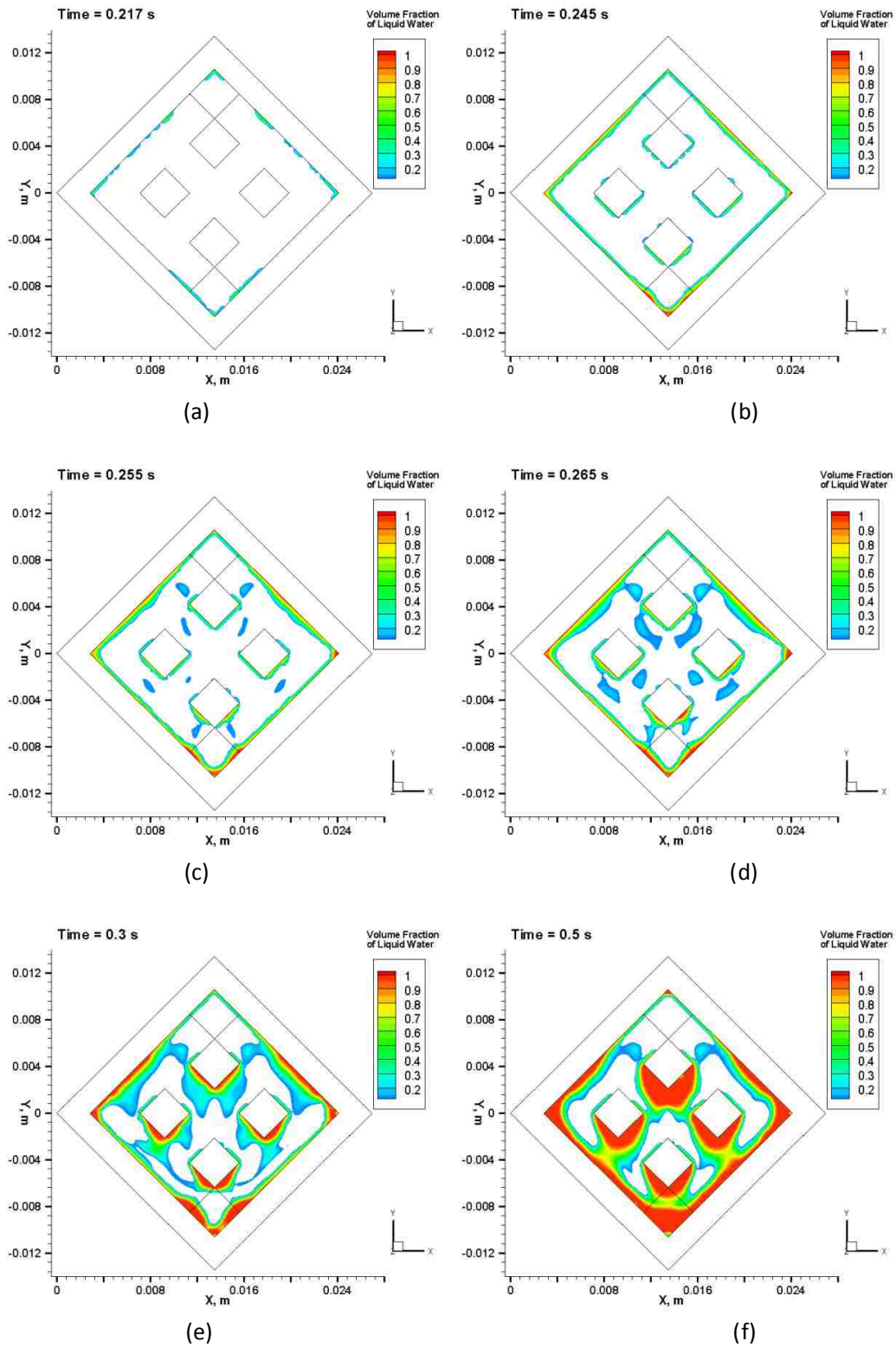
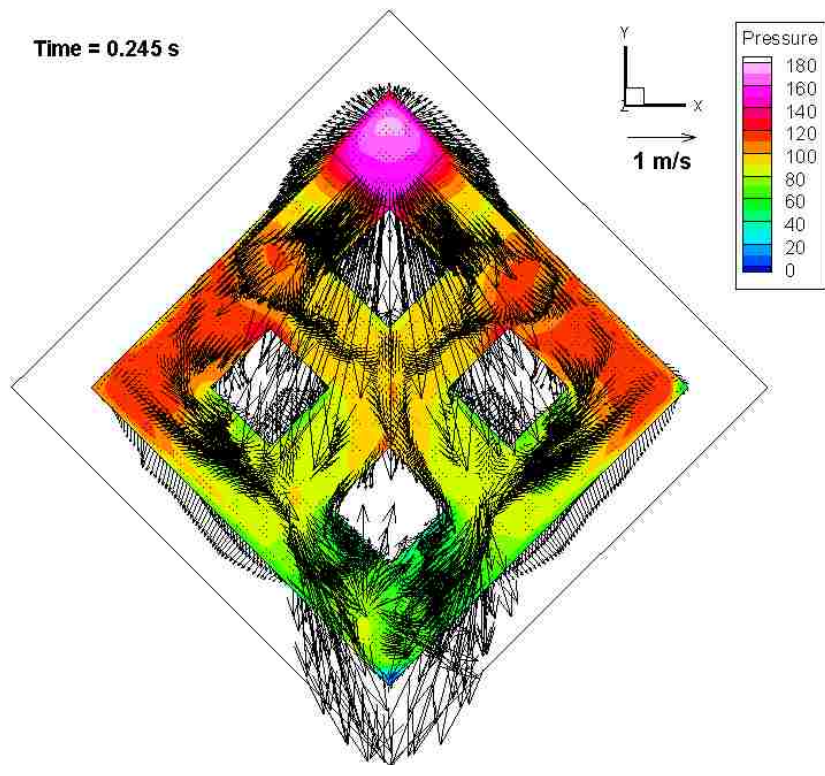
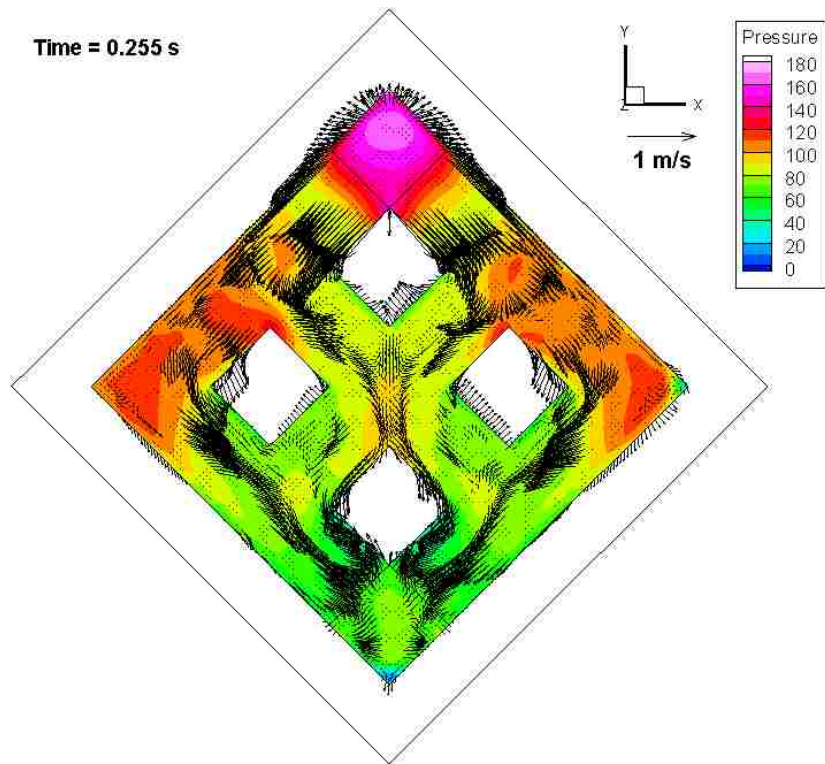


Figure 6-4(a-f) Liquid water distribution on plenum plane near interface ($Z = 0.00031$ m) in the STR-SCA model



(a)



(b)

Figure 6-5(a-b) Pressure distribution with velocity on plenum plane near interface ($Z = 0.00031$ m) in the STR-SCA model (unit: Pa)

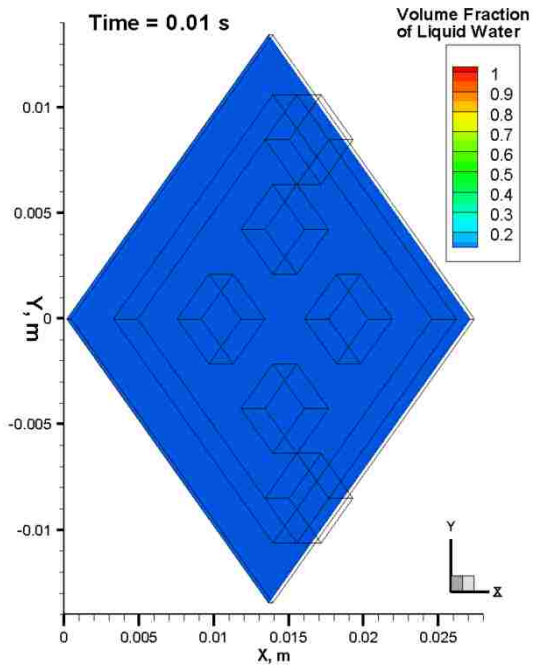
6.3. Liquid Water Transport in STR Model with Dynamic Contact Angle

6.3.1. General Process

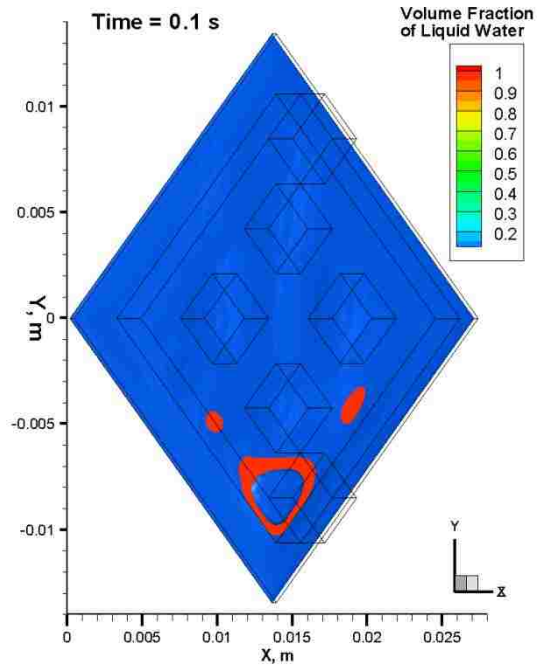
The general process of liquid water transport in the STR-DCA model is illustrated in Figure 6-5, by presenting three-dimension view of the computational domain with coloured liquid water volume fraction contours expressed by iso-surface. Like STR-SCA model, the main process in the STR-DCA model can also be summarized into several sub-processes as below.

- (1) The liquid water is supplied continuously from the liquid inlet boundary to simulate the generation of liquid water from electrochemical reactions (Figure 6-5(a)).
- (2) The surface of emerging water in the porous layer becomes bumpy, shrinking at the areas under the inlet channel and four pillars, and expanding mainly at the areas under plenum. Some liquid water reaches the interface and enters into the plenum domain under the outlet channel (Figure 6-5(b)).
- (3) More liquid water reaches the interface under nether part of the plenum appearing in a “V” shape and enters in to it (Figure 6-5(c, d)). Then the interface near the top pillar, under the bottom pillar, and under bottom frames get wet (Figure 6-5(e)).
- (4) Liquid water in the plenum accumulated at the area under the outlet channel drains out (Figure 6-5(f)).
- (5) With water draining, the liquid water in the porous layer and the plenum distributes in a relative steady pattern (Figure 6-5(g-j)).

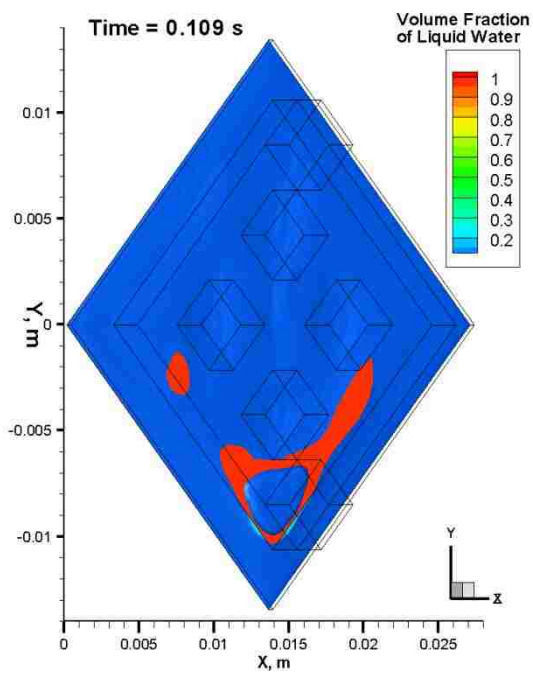
Generally, main process of liquid water transport in the STR-DCA model is different from that in the STR-SCA model with only the first sub-process staying exactly the same. Apparently, DCA effects weight much on the gas-liquid phenomena in the PEMFC model with STR flow field design. Detailed difference phenomena are going to be discussed in the following sections.



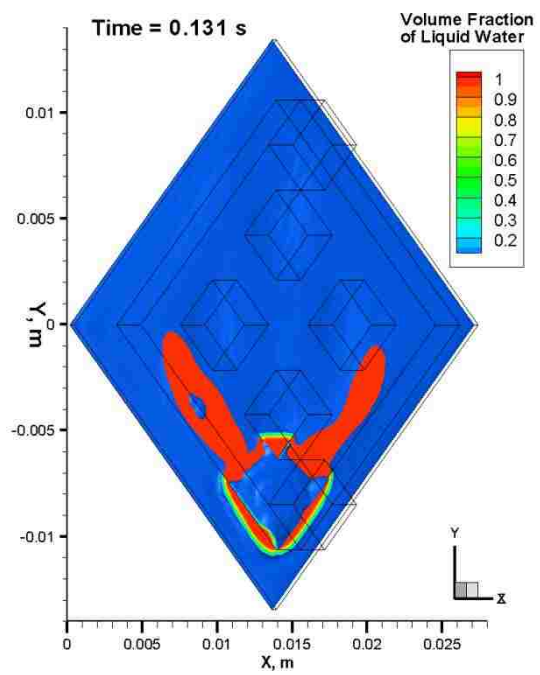
(a)



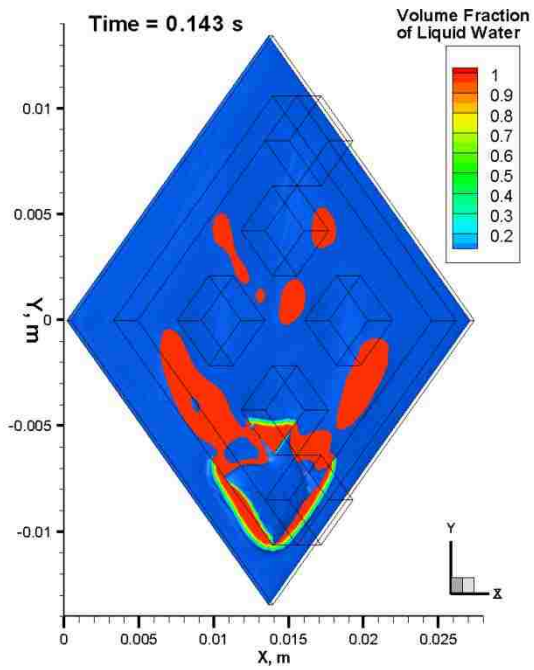
(b)



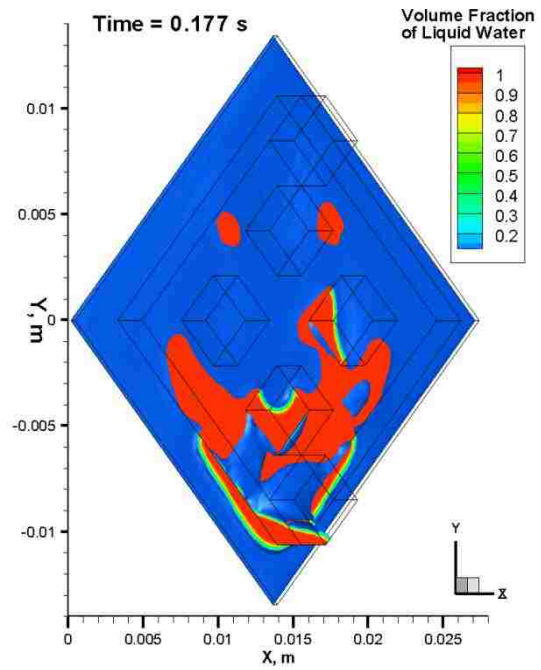
(c)



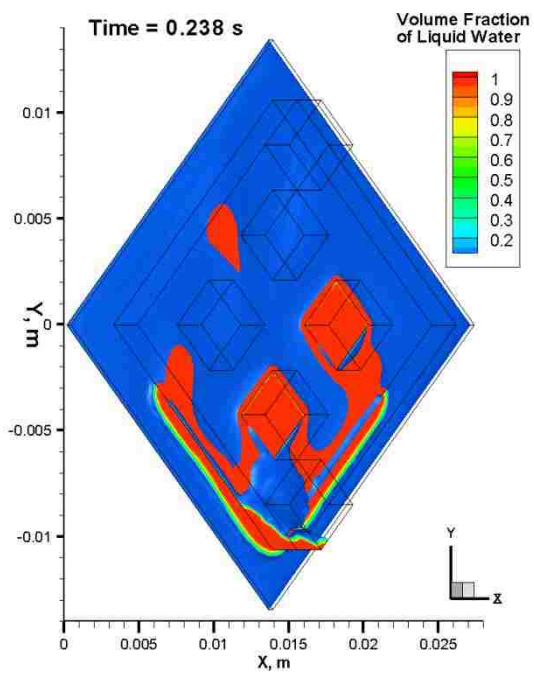
(d)



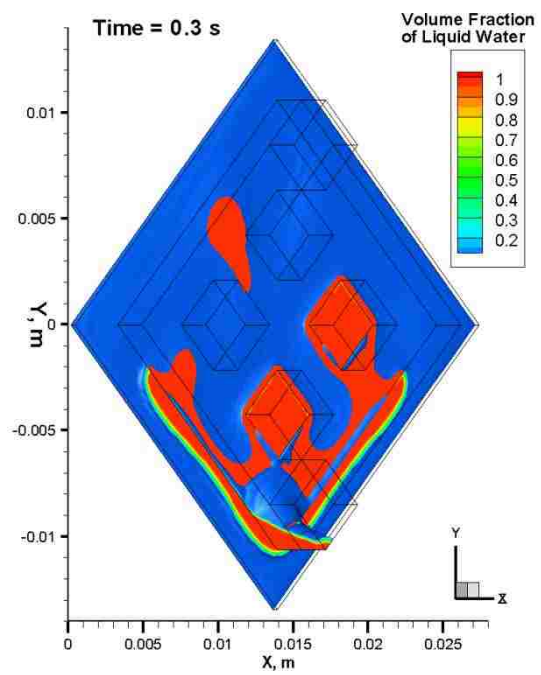
(e)



(f)



(g)



(h)

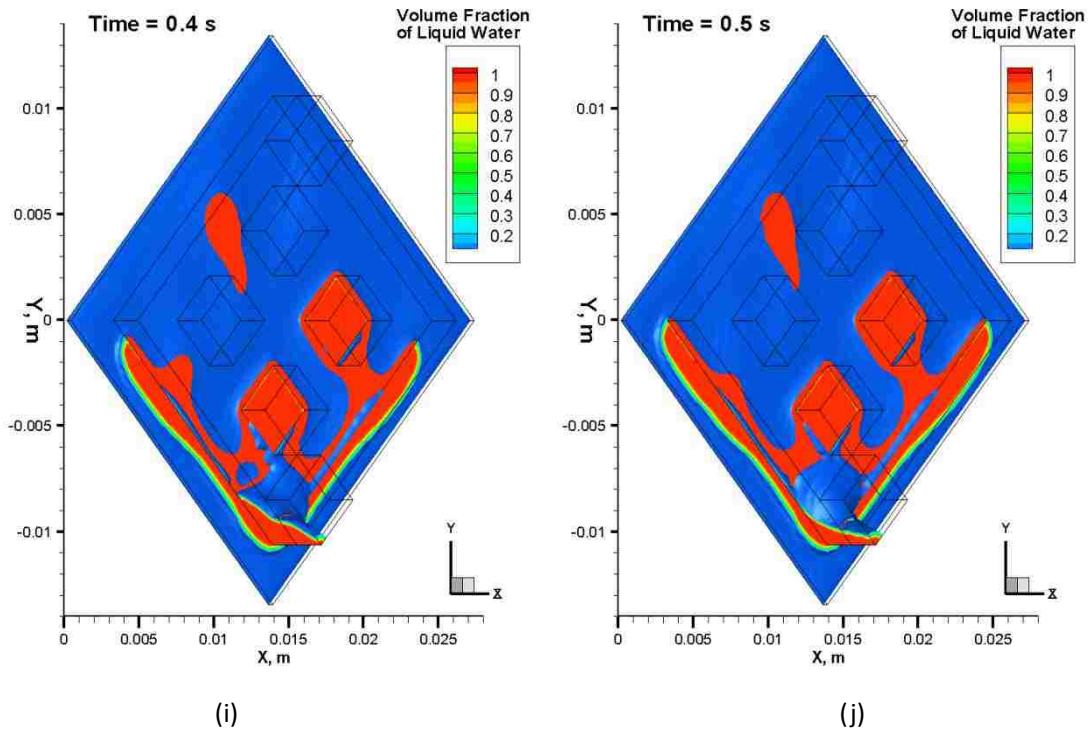
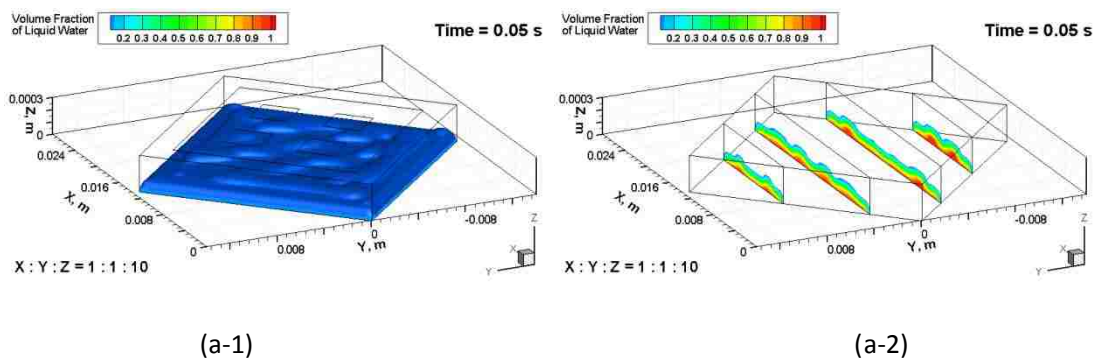


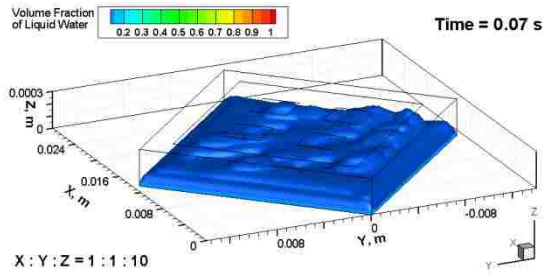
Figure 6-6(a-j) General liquid water transport in the STR-DCA model

6.3.2. Emerging Process

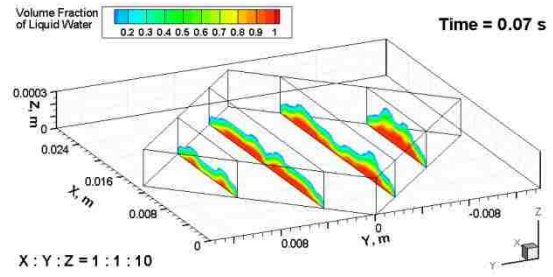
6.3.2.1. Liquid Water Surging in Porous Layer

Unlike that in the STR-SCA model, liquid water surges in the porous layer, and distributes like apex-valley, as presented in Figure 6-7. And the wave motions of liquid water surface exist during the emerging process. Take Figure 6-7(d, e) for example. In Figure 6-7(d), there is a protuberance touching the interface of the porous layer and the plenum near the inlet channel (leftmost side in the figure); whereas, it descends and doesn't touch the interface in Figure 6-7(e). The similar phenomena distinctly happens on the plane where $Y = 0.003$ m (right column in Figure 6-7(d, e)).

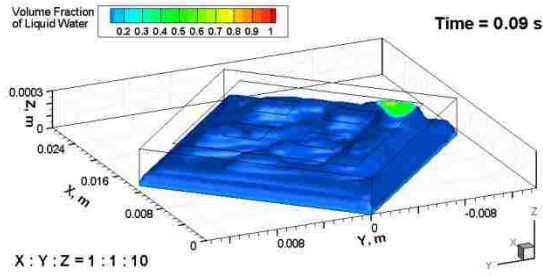




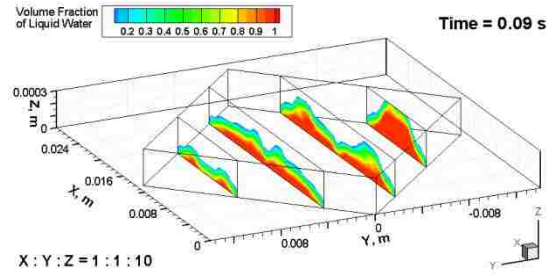
(b-1)



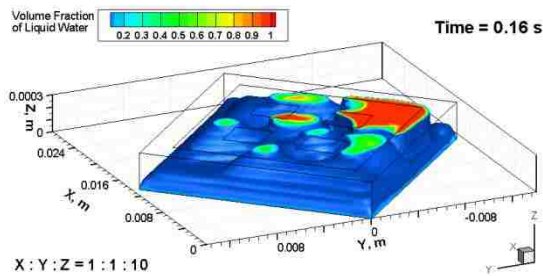
(b-2)



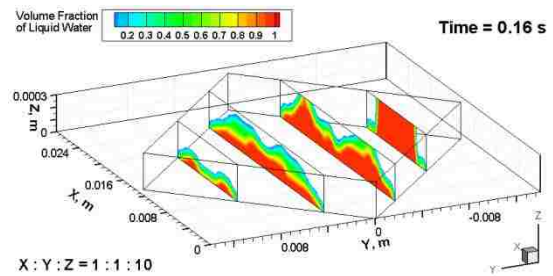
(c-1)



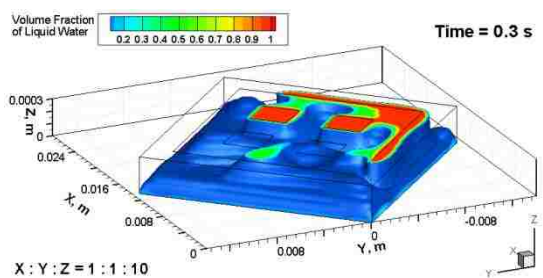
(c-2)



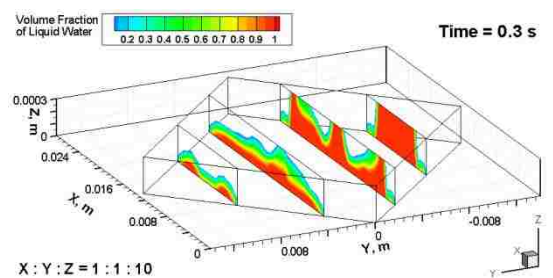
(d-1)



(d-2)



(e-1)



(e-2)

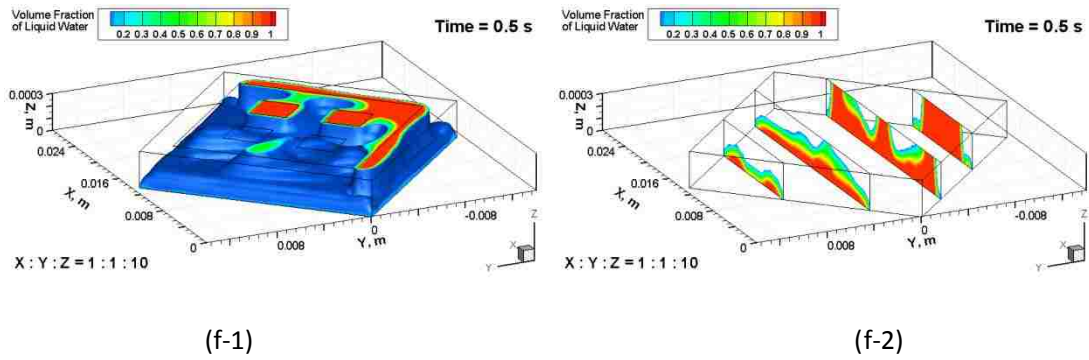
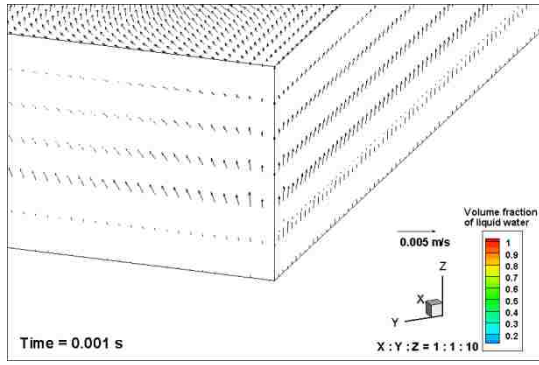
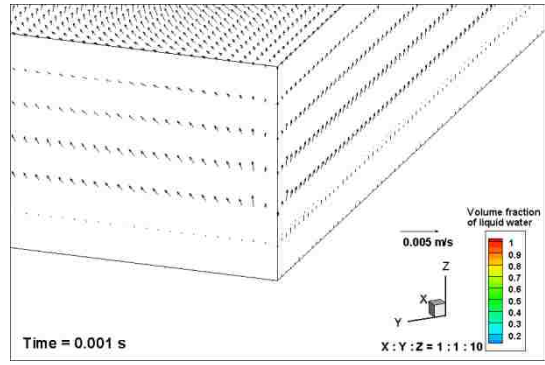


Figure 6-7(a-f) Liquid water transport in porous layer in the STR-SCA model
 (Left column: porous layer domain; right column: four planes extracted at $Y = -0.008$ m, -0.003 m, 0.003 m, and 0.008 m)

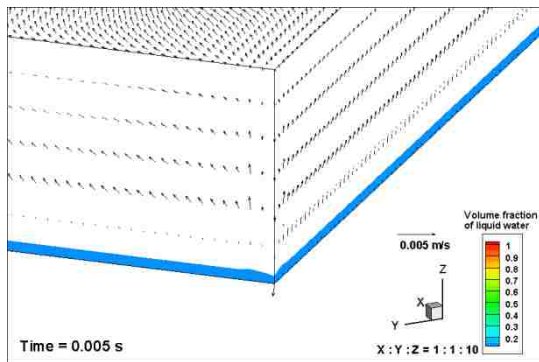
In order to study the reason why the liquid water distribution in the porous layer in the STR-DCA model is like apex-valley which differs from that happening in the STR-SCA model, a corner of porous layer (the bottom corner in Figure 6-7) is enlarged to plot water volume fraction with velocity vectors. The left columns in Figure 6-8 are from the STR-SCA model, and the right columns are from the STR-DCA model. It can be noticed that at the very beginning of the simulation, the velocity fields are quite similar between two models (Figure 6-8(a)). However, when liquid water starts to emerge into the porous layer and rises up, the velocity vectors alter in both magnitude and directions (Figure 6-8(b, c)), which shows the effects of DCA on the interaction between gas and liquid. Figure 6-9 shows the flooded DCA contours on the walls of the enlarged corner, where deep green stands for 130° (initial setting of contact angle on the wall boundaries). At the very beginning (same time instance as in Figure 6-8(a)), the contact angles on sidewalls of the porous layer close to the liquid inlet boundary (light green) are greater than 130° (deep green) (Figure 6-9(a)), this is caused by the impulsion of the initial liquid mass flow. This increase in DCA value gives an influence on the wall adhesion which makes the wall get more hydrophobic and repulse water, so liquid water dislikes accumulating near sidewalls of the porous layer. Because of less water accumulating near the wall, the influence of DCA becomes lower, and gradually into a steady status (Figure 6-9(b-d)). Although the difference of DCA values is not much and just at the beginning, it affects the liquid water distribution and emerging pattern significantly afterwards, and that is the reason why in the STR-DCA model the liquid water in the porous layer appears as apex-valley and surges up, other than emerging tranquilly in the STR-SCA model.



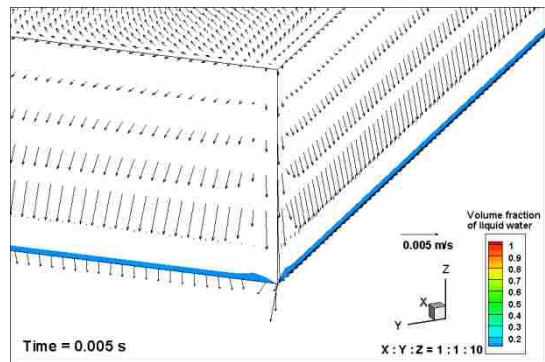
(a-1) SCA



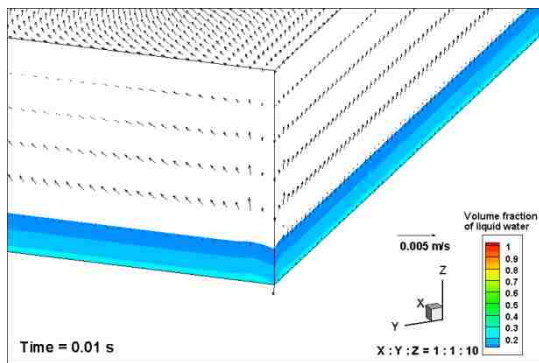
(a-2) DCA



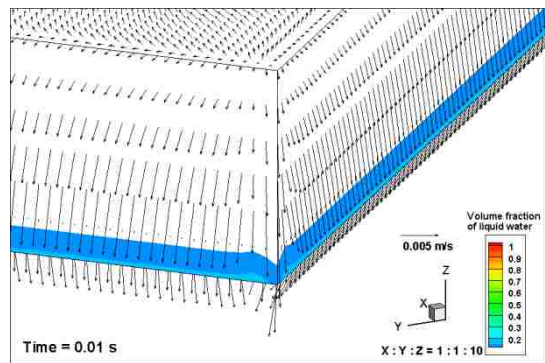
(b-1) SCA



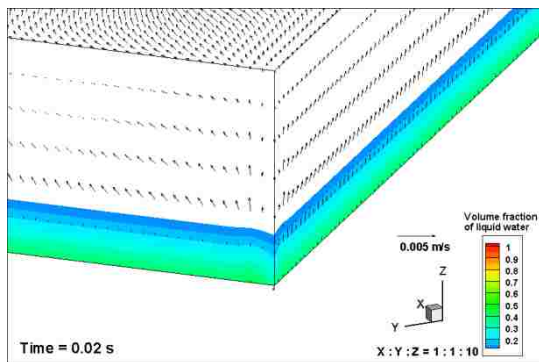
(b-2) DCA



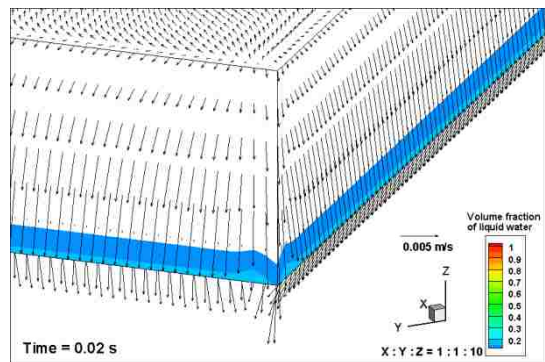
(c-1) SCA



(c-2) DCA



(d-1) SCA



(d-2) DCA

Figure 6-8(a-d) Liquid water and velocity field near walls (partial) of porous layer at the beginning of emerging process

(Left column: the STR-SCA model; right column: the STR-DCA model)

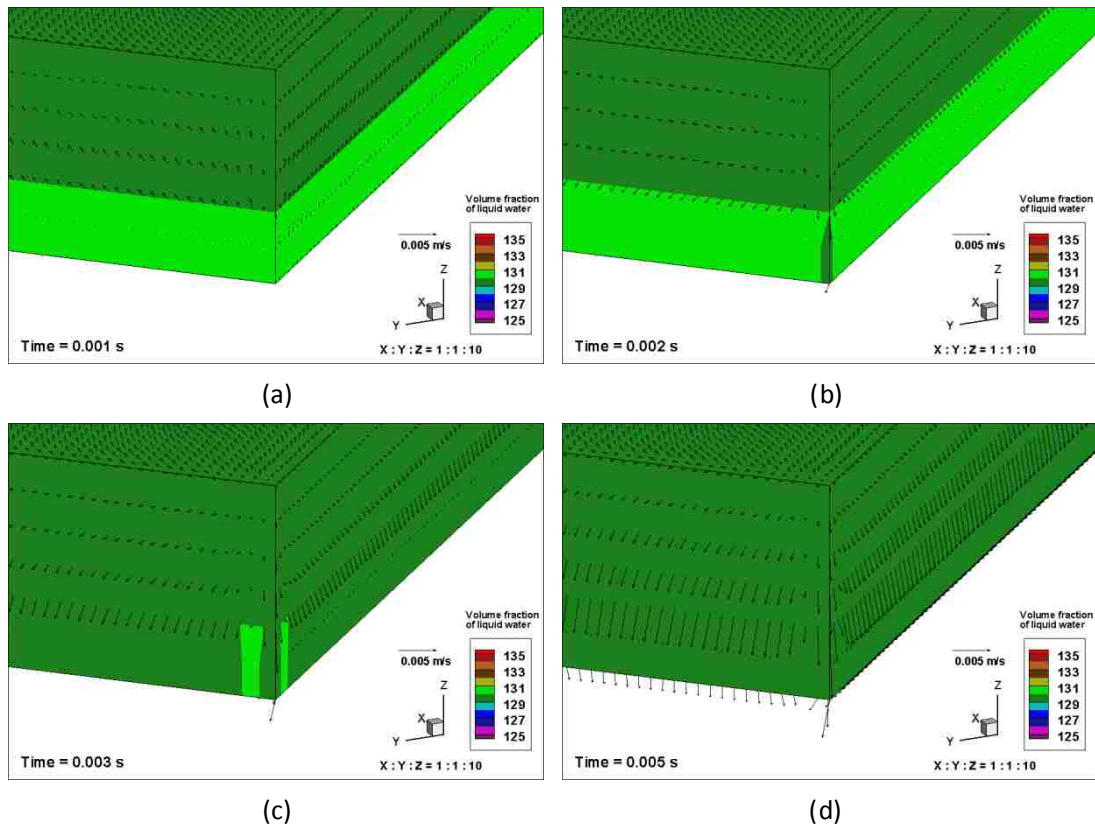


Figure 6-9(a-d) Dynamic contact angle effects on velocity change at the beginning of emerging process in the STR-DCA model

6.3.2.2. Liquid Water Distribution in Plenum

Figure 6-10 presents the liquid water distribution on a plenum plane extracted near the interface ($Z = 0.00031$ m), with edges of the porous layer, the inlet channel, and the outlet channel shown. Liquid water emerging from the porous layer mainly concentrates at the lower part of the plenum due to the influence of gravity and the DCA effects on the water distribution in the porous layer discussed in the previous section. It is been observed that in Figure 6-10(c) there is water entering into plenum at the left circumference of the lower pillar but shrinking back into the porous layer in the later time instances (Figure 6-10(d-f)), because of the wave motion of liquid water also discussed in the previous section.

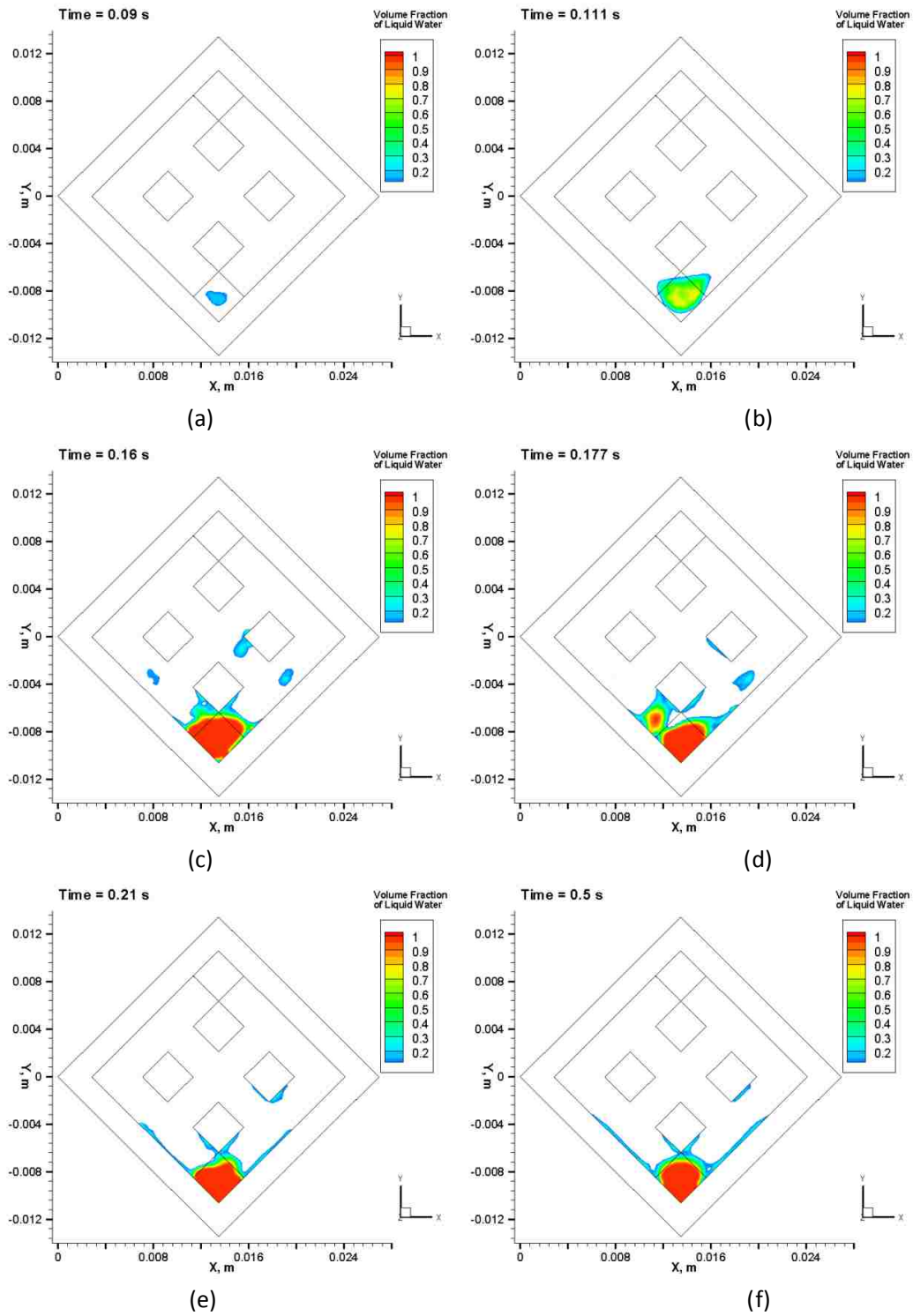
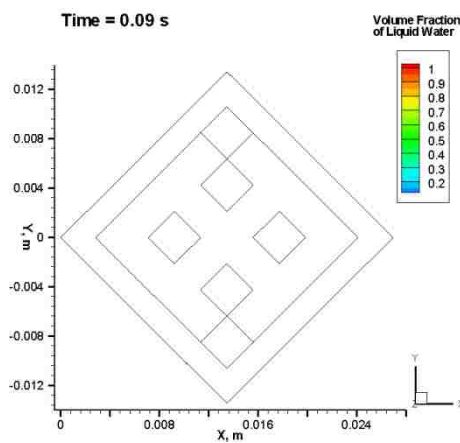


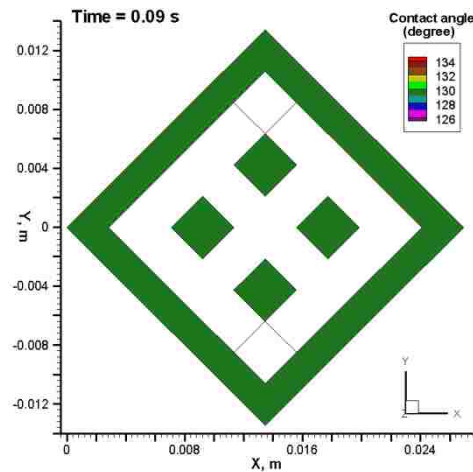
Figure 6-10(a-f) Liquid water distribution on plenum plane near interface ($Z = 0.00031$ m) in STR-SCA model

In order to study the influence of DCA on liquid water distribution in plenum as presented in Figure 6-10, a series of figures (Figure 6-11) with liquid water volume fraction and DCAs on top walls of the porous layer (namely on the same plane with interface ($Z = 0.00031$ m)) are plotted,

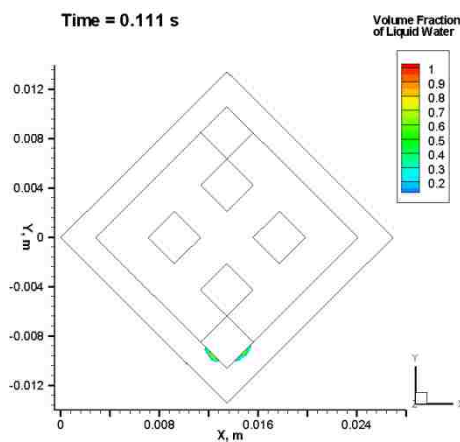
at the same time instances as those in Figure 6-10. At first (0.09s), there is no liquid water on the wall (Figure 6-11(a-1)), so the contact angle remains at initial setting (130° , Figure 6-11(a-2), deep green). When liquid water reaches the top walls of the porous layer (Figure 6-11(b-1)), the contact angles at these areas are affected by the change of volume fraction and velocity in the computational cells and become higher (Figure 6-11(b-2), light green), so the wettability there turns more hydrophobic that more water are squeezed away and enters into the plenum from the nearest interface, i.e. the edges of the pillars and the frame. Since the initial contact angle on sidewalls of the plenum is 53° that the wall wettability is hydrophilic, emerging liquid water moves along the sidewalls because of the large wall adhesion.



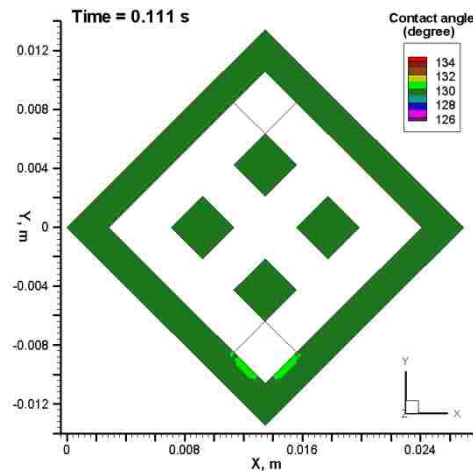
(a-1)



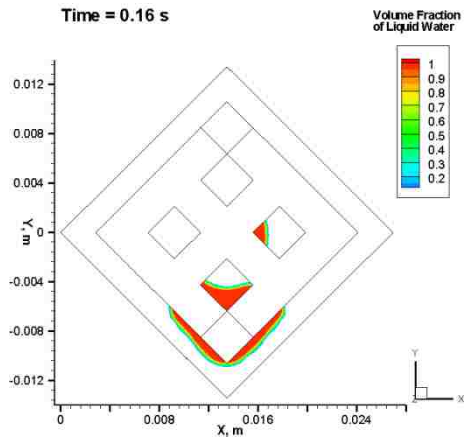
(a-2)



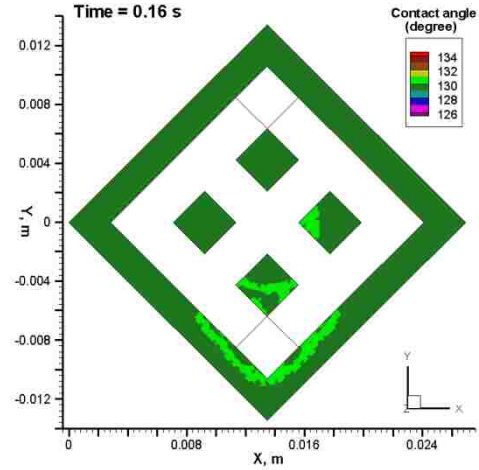
(b-1)



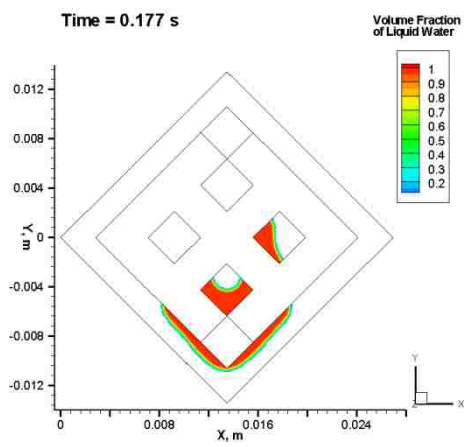
(b-2)



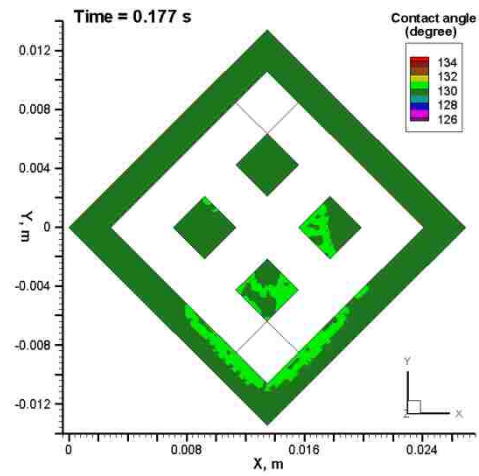
(c-1)



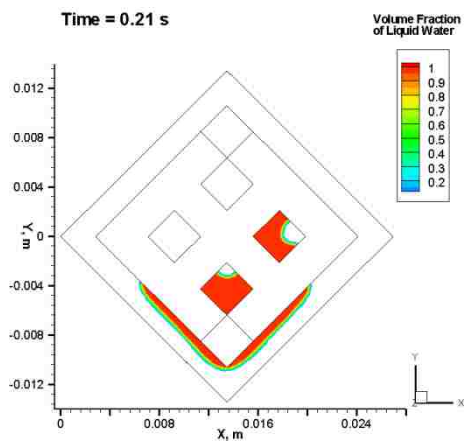
(c-2)



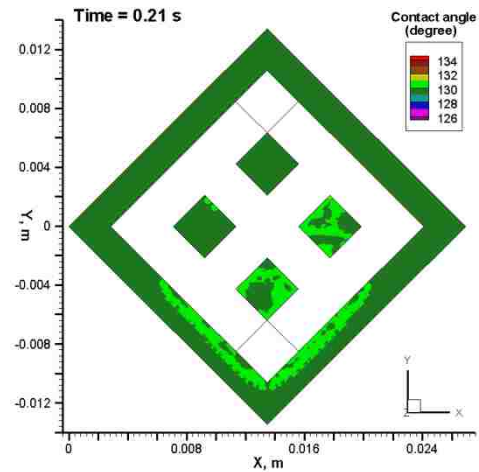
(d-1)



(d-2)



(e-1)



(e-2)

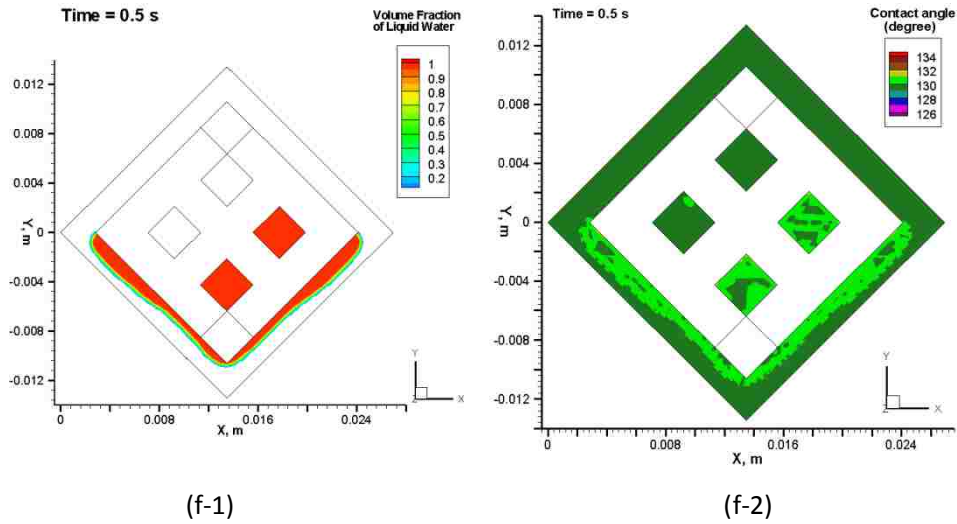
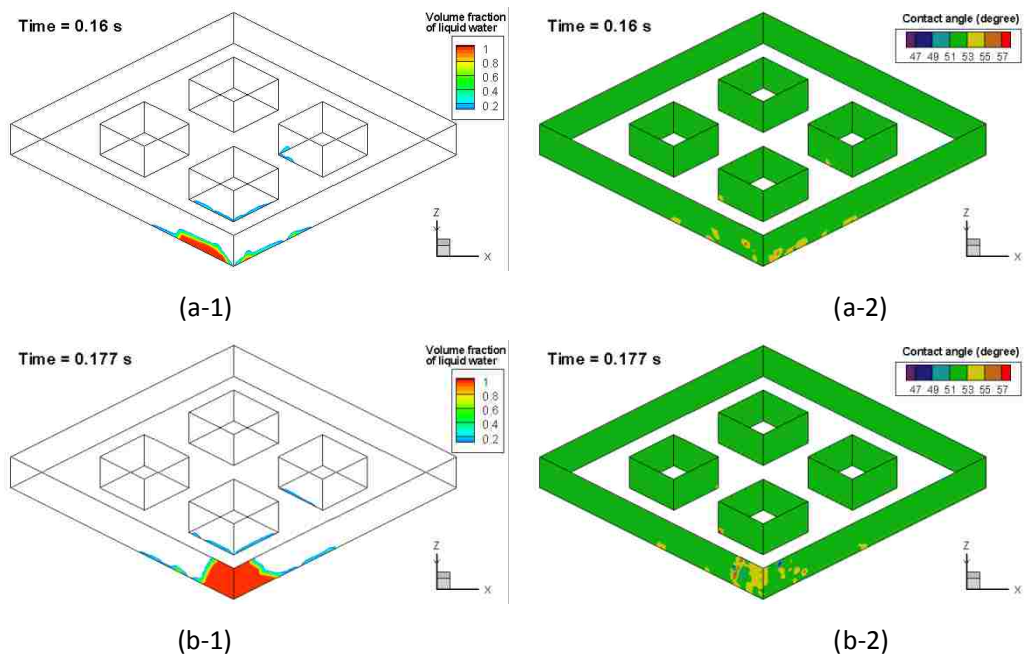


Figure 6-11(a-f) Liquid water distribution and contact angles on PL walls in the STR-DCA model (Left column: liquid water distribution; right column: dynamic contact angles)

Figure 6-12 shows the liquid water movements (expressed by volume fraction) and DCAs on sidewalls of the plenum. Similar to what happens on the top walls of the porous layer (Figure 6-11), contact angles are affected by the water distribution, but change greatly at where liquid water move tempestuously, usually at the interface of two-phases.



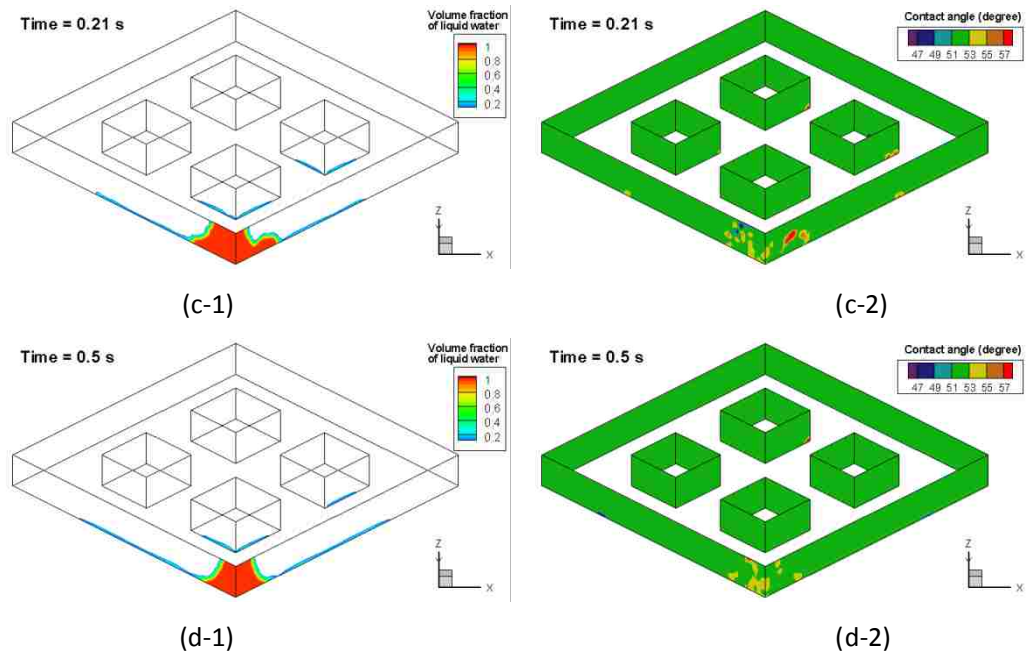


Figure 6-12(a-d) Liquid water distribution and contact angles on sidewalls in the STR-DCA model (Left column: liquid water distribution; right column: dynamic contact angles)

6.4. Comparison of Liquid Water Amount and Gauge Pressure

Figure 6-13 and Figure 6-14 plot liquid water amount (kg) with time in plenum, porous layer, inlet channel, and outlet channel in the STR-SCA model and the STR-DCA model respectively. In the STR-SCA model, at first liquid water only moves in the porous layer at a speed with a constant slope (Speed 1), and then enters into the plenum around 0.225 s with a lower slope (Speed 2), meanwhile the water amount in the porous layer rests in a small range. Liquid water starts to drain out at approximate 0.37 s while the water amount in the plenum becomes steady. Similarly happen in the STR-DCA model, and Speed 1 and Speed 2 are quite same between two models. However, there are several points in the STR-DCA model differing from the STR-SCA model. Firstly, the speed change of water amount in porous layer is more gently than in the STR-SCA model. Secondly, the times when liquid water enters into the plenum and drains out are early than that in the STR-SCA model. Thirdly, the amount of liquid water in steady status (when water draining out) containing in the porous layer and the plenum are lower, almost half of that in the STR-SCA model. In a word, the effects of DCA improve the ability of drainage in the STR model.

Figure 6-15 and Figure 6-16 present the average gauge pressure (Pa) at the gas inlet and outlet

surfaces over time in the STR-SCA model and the STR-DCA model respectively. Inlet pressure differences during entire simulation in both models are within 100 Pa, though the fluctuation of inlet pressure in the STR-SCA model has a higher frequency.

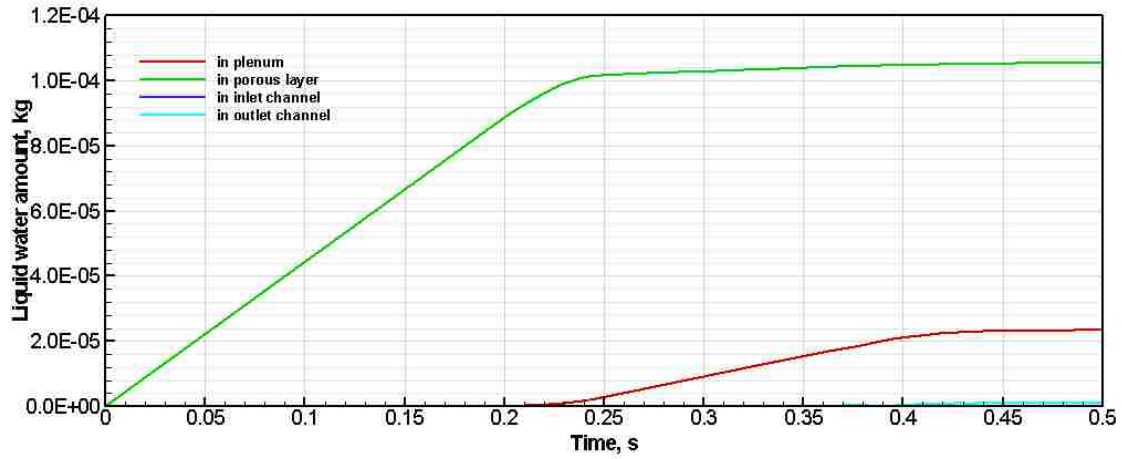


Figure 6-13 Liquid water amount in the STR-SCA model over time

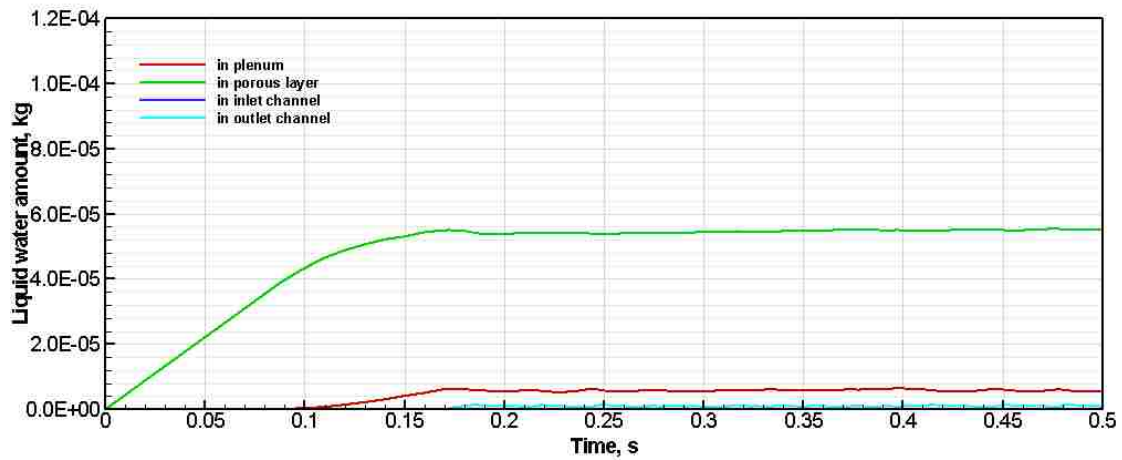


Figure 6-14 Liquid water amount in the STR-DCA model over time

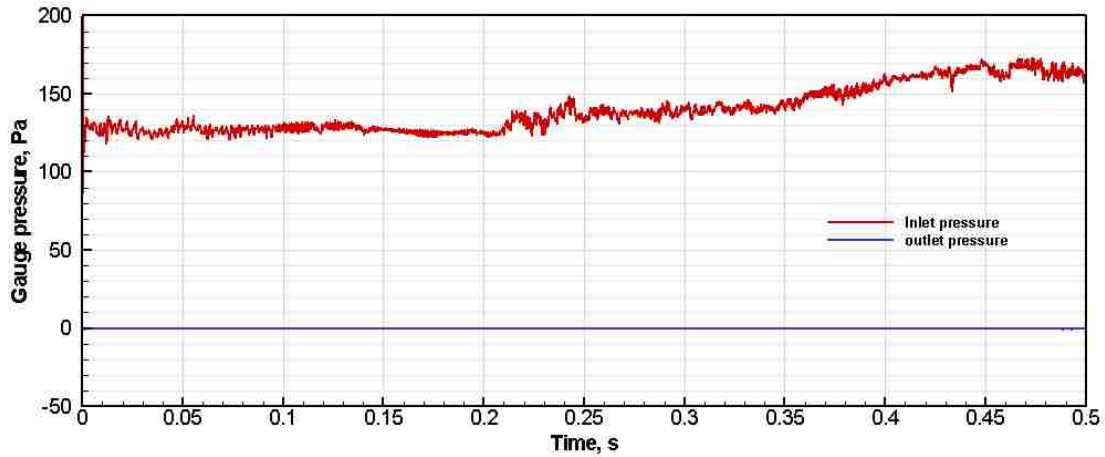


Figure 6-15 Gauge pressure in the STR-SCA model over time

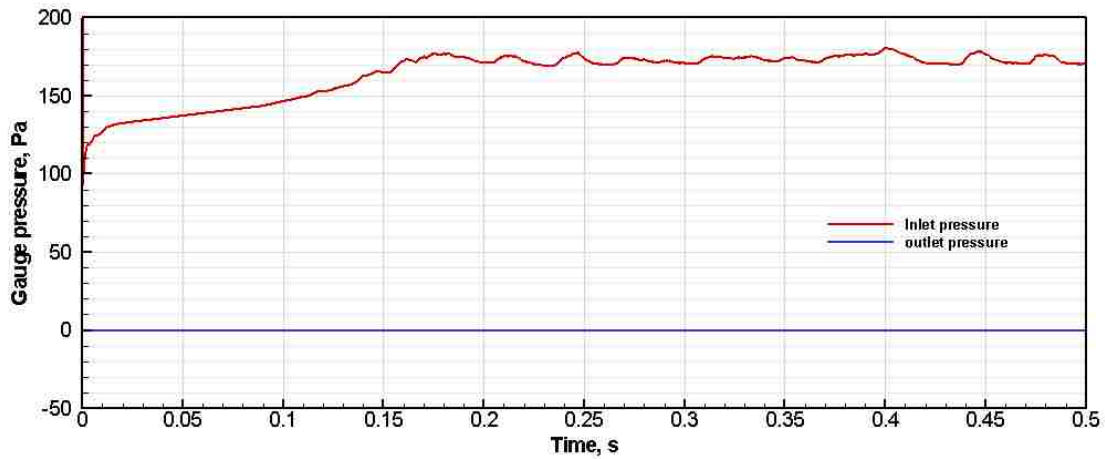


Figure 6-16 Gauge pressure in the STR-DCA model over time

6.5. Summary

The cathode model of PEMFC with STR design has better capability of water drainage than other models with traditional designs, such as parallel design, so that the fluid flow field in the STR model hardly gets blocked or fully flooded which weakens the power density of whole cell.

With consideration of DCA effects in the STR model, the aspect mostly differing from the STR-SCA model is the liquid water distribution and emerging pattern in the porous layer (SCA: tranquilly; DCA: surging), causing a difference in distribution in the plenum. And the time instances when water entering into the plenum and draining out are different between two models as well, that in the STR-DCA model the time instances are earlier than that in the STR-SCA model.

7. CONCLUSIONS

In this thesis, a three-dimensional, two-phase numerical model is developed and applied to investigate gas-liquid phenomena inside the cathode of proton exchange membrane fuel cells (PEMFC) with different gas flow field designs. The present numerical model uses volume of fluid (VOF) method which has been validated by Le et al. [33] to track gas-liquid interface. Dynamic contact angle (DCA) is compiled to wall boundary conditions through user defined function (UDF) code. The improved Hoffman function, which is used to calculate DCA, is modified by inserting a correction term to the original Hoffman function. This methodology is validated by conducting two numerical models with the same computational domains and operating conditions from the experiments carried out by other researchers. One is a water slug flow in a rectangular micro-channel; the other is a glycerine droplet impact on a glass plate.

By using this presented methodology, the gas-liquid phenomena inside the PEMFC cathode with the gas flow field design of parallel channel and a stirred tank reactor (STR). Two numerical models, with/without the implementation of DCA, i.e., the DCA model and the SCA model, are conducted for each design. For the parallel design, although general processes are similar, the emerging pattern, Dean vortices' distribution, and draining deformation are quite different between the Parallel-SCA and the Parallel-DCA models. While for the STR design, the differences between the STR-SCA and the STR-DCA models exist in emerging pattern and liquid water distribution as well as the time instances when liquid water enters into the plenum and drains out.

From the results discussed, it can be summarized and concluded into several points as below:

- (1) Liquid water firstly emerges from the edges of the interface under the channels in the Parallel-SCA model while liquid water emerges from the middle of the interface under the channels in the Parallel-DCA model.
- (2) Dean vortices in parallel channels distribute in an upper-lower pattern in the Parallel-SCA model and in a left-right pattern in the Parallel-DCA model.
- (3) Draining water in the Parallel-SCA model is in a top-bottom stratified flow while in the

Parallel-DCA model is in an inconstant flow.

- (4) Liquid water emerges tranquilly in the porous layer in the STR-SCA model; whereas it surges up like apex-valley in the STR-DCA model.
- (5) The time instances when water entering into the plenum and draining out are different between the two models; in the STR-DCA model the time instances are earlier than that in the STR-SCA model.
- (6) With compiling DCA to wall boundaries, numerical models showed better capability in drainage.

Since this presented methodology is applied to simulate liquid transport only in the cathode of PEMFC, rather than the whole cell, in the future, the model could be improved to simulate entire PEMFCs with different designs. And comparison experiments could be conducted for further validations.

REFERENCES

- [1] R. O'Hayre, S.-W. Cha, W. Colella, F. B. Prinz, Fuel Cell Fundamentals, 2nd Edition, (2008).
- [2] T. S. Chow, Wetting of rough surfaces, Journal of Physics: Condensed Matter 10 (27): (1998) L445.
- [3] K. Jiao, X. Li, Water transport in polymer electrolyte membrane fuel cells, Progress in Energy and Combustion Science, 37 (2011) 221-291.
- [4] D. Singh, D.M. Lu, N. Djilali, A two-dimensional analysis of mass transport in proton exchange membrane fuel cells, International Journal of Engineering Science 37 (1999) 431–445.
- [5] N. Djilali, D. Lu, Influence of heat transfer on gas and water transport in fuel cells, International Journal of Thermal Sciences 41 (2002) 29–40.
- [6] S. Dutta, S. Shimpalee, J.W. Van Zee, Three-dimensional numerical simulation of straight channel PEM fuel cells, Journal of Applied Electrochemistry 30 (2000) 135–146.
- [7] S.-W. Cha, R. O'Hayre, Y. Saito, F.B. Prinz, The scaling behaviour of flow patterns: a model investigation, Journal of Power Sources 134 (2004) 57–71.
- [8] A.A. Kulikovskiy, Numerical simulation of a new operational regime for a polymer electrolyte fuel cell, Electrochemistry Communications 3 (2001) 460–466.
- [9] J.S. Yi, J.D. Yang, C. King, Water management along the flow channels of PEM fuel cells, Journal of AIChE 50 (2004) 2594–2603.
- [10] L. You, H. Liu, A two-phase flow and transport model for the cathode of PEM fuel cells, International Journal of Heat Mass Transfer 45 (2002) 2277–2287.
- [11] Z.H. Wang, C.Y. Wang, K.S. Chen, Two-phase flow and transport in the air cathode of proton exchange membrane fuel cells, Journal of Power Sources 94 (2001) 40–50.
- [12] M.M. Mench, Q.L. Dong, C.Y. Wang, In situ water distribution measurements in a polymer electrolyte fuel cell, Journal of Power Sources 124 (2003) 90–98.
- [13] J.E. Dawes, N.S. Hanspal, O.A. Family, A. Turan, Three-dimensional CFD modelling of PEM fuel cells: an investigation into the effects of water flooding, Journal of Chemical Engineering Science 64 (2009) 2781–2794.

- [14] G. Luo, Y. Ji, C.-Y. Wang, P.K. Sinha, Modeling liquid water transport in gas diffusion layers by topologically equivalent pore network, *Electrochimica Acta* 55 (2010) 5332–5341.
- [15] C.Y. Wang, Fundamental models for fuel cell engineering, *Chemical Reviews*, 104 (2004) 4727-4766.
- [16] A. Z. Weber, J. Newman, Modeling transport in polymer-electrolyte fuel cells, *Chemical Reviews*, 104 (2004) 4679-4726.
- [17] H. Li, Y. Tang, Z. Wang, Z. Shi, S. Wu, D. Song, J. Zhang, K. Fatih, J. Zhang, H. Wang, Z. Liu, R. Abouatallah, A. Mazza, A review of water flooding issues in the proton exchange membrane fuel cell, *Journal of Power Sources*, 178 (2008) 103-117.
- [18] Q. Ye, T. V. Nguyen, Three-dimensional simulation of liquid water distribution in a PEMFC with experimentally measured capillary functions, *Journal of Electrochemical Society*, 154 (2007) B1242-B1251.
- [19] P.C. Sui, S. Kumar, N. Djilali, Advanced computational tools for PEM fuel cell design. Part 1: development and base case simulations, *Journal of Power Sources*, 180 (2008) 410-422.
- [20] H. Wu, P. Berg, X. Li, Steady and unsteady 3D non-isothermal modeling of PEM fuel cells with the effect of non-equilibrium phase transfer, *Applied Energy*, 87 (2010) 2778-2784.
- [21] H. Meng, C.Y. Wang, New model of two-phase flow and flooding dynamics in polymer electrolyte fuel cells, *Journal of Electrochemical Society*, 152 (2005) A1733–A1741.
- [22] S. Basu, J. Li, C.Y. Wang, Two-phase flow and maldistribution in gas channels of a polymer electrolyte fuel cell, *Journal of Power Sources* 187 (2009) 431-443.
- [23] P. P. Mukherjee, Q. Kang, C.Y. Wang, Pore-scale modeling of two-phase transport in polymer electrolyte fuel cells—progress and perspective, *Energy Environ. Sci.*, 4 (2011) 346-369.
- [24] P. Quan, B. Zhou, A. Sobiesiak, Z. Liu, Water behaviour in serpentine micro-channel for proton exchange membrane fuel cell cathode, *Journal of Power Sources*, 152 (2005) 131-145.
- [25] K. Jiao, B. Zhou, P. Quan, Liquid water transport in parallel serpentine channels with manifolds on cathode side of a PEM fuel cell stack, *Journal of Power Sources*, 154 (2006) 124-137.
- [26] K. Jiao, B. Zhou, P. Quan, Liquid water transport in straight micro-parallel-channels with manifolds for PEM fuel cell cathode, *Journal of Power Sources*, 157 (2006) 226-243.

- [27] K. Jiao, B. Zhou, Innovative gas diffusion layers and their water removal characteristics in PEM fuel cell cathode, *Journal of Power Sources*, 169 (2007) 296-314.
- [28] K. Jiao, B. Zhou, Effects of electrode wettabilities on liquid water behaviours in PEM fuel cell cathode, *Journal of Power Sources*, 175 (2008) 106-119.
- [29] K. Jiao, B. Zhou, Accelerated numerical test of liquid behaviour across gas diffusion layer in proton exchange membrane fuel cell cathode, *Journal of Fuel Cell Science and Technology*, 5 (2008) 041011.
- [30] A. D. Le, B. Zhou, A general model of proton exchange membrane fuel cell, *Journal of Power Sources*, 182 (2008) 197-222.
- [31] A. D. Le, B. Zhou, Fundamental understanding of liquid water effects on the performance of a PEMFC with serpentine-parallel channels, *Electrochimica Acta*, 54 (2009) 2137-2154.
- [32] A. D. Le, B. Zhou, A numerical investigation on multi-phase transport phenomena in a proton exchange membrane fuel cell stack, *Journal of Power Sources*, 195 (2010) 5278-5291.
- [33] A. D. Le, B. Zhou, H.R. Shiu, C.I. Lee, W. C. Chang, Numerical simulation and experimental validation of liquid water behaviours in a proton exchange membrane fuel cell cathode with serpentine channels, *Journal of Power Sources*, 195 (2010) 7302-7315.
- [34] X. Wang, B. Zhou, Liquid water flooding process in proton exchange membrane fuel cell cathode with straight parallel channels and porous layer, *Journal of Power Sources*, 196 (2011) 1776-1794.
- [35] S Kang, B Zhou, C Cheng, H Shiu, C Lee, Liquid water flooding in a proton exchange membrane fuel cell cathode with an interdigitated design, *Int. J. Energy Res.* (2011), DOI: 10.1002/er.1858.
- [36] X. Zhu, P. C. Sui, N. Djilali, Numerical simulation of emergence of a water droplet from a pore into a microchannel gas stream, *Microfluid Nanofluid* 4 (2008) 543-555.
- [37] X. Zhu, P. C. Sui, N. Djilali, Three-dimensional numerical simulations of water droplet dynamics in a PEMFC gas channel, *Journal of Power Sources*, 181 (2008) 101-115.
- [38] G. Minor, N. Djilali, D. Sinton and P. Oshkai, Flow within a water droplet subjected to an air stream in a hydrophobic microchannel, *Fluid Dyn. Res.*, 41 (2009) 045506.
- [39] S. Sikalo, H. D. Wilhelm, I.V. Roisman, S. Jakirlic, and C. Tropea, Dynamic contact angle of spreading droplets: Experiments and simulations, *Physics of Fluids* 17-062103 (2005) p. 1-13.

- [40] S. Sikalo, E.N. Ganic, Phenomena of droplet–surface interactions, *Experimental Thermal and Fluid Science* 31 (2006) 97–110.
- [41] S. Sikalo, M. Marengo, C. Tropea, E. Ganic, Analysis of impact of droplets on horizontal surfaces, *Experimental Thermal and Fluid Science* 25 (2002) 503-510
- [42] S. F. Kistler, Hydrodynamics of wetting, in *Wettability*, edited by J. C. Berg (Marcel Dekker, New York, 1993) p. 311.
- [43] Chris Miller, Liquid water dynamics in a model polymer electrolyte fuel cell flow channel, A MASC Thesis in University of Victoria (2009).
- [44] J. Benziger, E. Chia, E. Karnas, J. Moxley, C. Teuscher, I.G. Kevrekidis, The stirred tank reactor polymer electrolyte membrane fuel cell, *AIChE J.*, 50 (2004) 1889-1900.
- [45] W. Hogarth, J. Benziger, Operation of polymer electrolyte membrane fuel cells with dry feeds: Design and operating strategies, *Journal of Power Sources* 159 (2006) 968-978.
- [46] R. L. Hoffman, A study of the advancing interface. I. Interface shape in liquid-gas systems, *J. Colloid Interface Sci.* 50 (1975) 228-241.
- [47] C. Fang, C. Hidrovo, F. Wang, J. Eaton, K. Goodson, 3-D numerical simulation of contact angle hysteresis for microscale two-phase flow, *International Journal of Multiphase Flow* 34 (2008) 690–705.
- [48] J. E. Steinbrenner, E. S. Lee, C. H. Hidrovo, J. K. Eaton, K. E. Goodson, Impact of channel geometry on two-phase flow in fuel cell microchannels, *Journal of Power Sources* 196 (2011) 5012–5020.
- [49] W. R. Dean, Note on the motion of fluid in a curved pipe, *Philosophical Magazine* 20 (1927) 208-223.

VITA AUCTORIS

Xichen Wang was born in 1987 in Jiangsu Province, China. She graduated from Hohai University, China in 2009 with a Bachelor of Science degree in Thermal Energy and Power Engineering. Since September in 2009, she is pursuing a M. A. Sc. degree in Mechanical Engineering at University of Windsor, Canada and hopes to graduate in September, 2011.